



**POLITECNICO**  
MILANO 1863

SCUOLA DI INGEGNERIA INDUSTRIALE  
E DELL'INFORMAZIONE

# Baroreflex control implementation and performance evaluation of a cardiovascular hybrid mock circulation loop

TESI DI LAUREA MAGISTRALE IN  
BIOMEDICAL ENGINEERING - INGEGNERIA BIOMEDICA

Authors: Federica Mechelli (941950)  
Guido Evangelisti (943839)

Advisor: Prof. Maria Laura Costantino  
Co-advisors: Francesco De Gaetano, PhD  
Academic Year: 2021-22



# Abstract

Cardiovascular devices need an extensive process of testing and validation before placing them in the market. In vitro evaluation of cardiovascular devices is usually made using conventional hydraulic mock loops which have limited versatility.

In collaboration with the Department of Chemistry, Materials and Chemical Engineering “Giulio Natta” (Laboratory of Biological Structure Mechanics, LaBS) and the Istituto Cardiocentro Ticino, we aim at developing a hybrid mock loop providing realistic hemodynamic waveforms in different scenarios including rest, exercise, infarction, with and without cardiovascular device support. The whole set-up is very user-friendly: users can easily choose, through the graphic user interface (GUI), the cannulation type (right heart or left heart), the configuration of the mock loop and values of the heart rate (HR) and contraction fraction (CF) parameters. There are two main configurations: *Baroreflex* mode which exploits the baroreflex control mechanism for the unstressed venous volume (UVV), systemic vascular resistances (SVR) and heart rate (HR) and *Device testing* mode, which allows the tuning of heart rate and contraction fraction in real-time. The first configuration can be used to understand if the heart is recovering thanks to its auto-regulation mechanisms once the cardiovascular device has been implanted, the second is aimed at evaluating the interactions between the device and the numerical model of the circulation. The mock loop validation is done in three main phases: (1) Numerical model assessment. (2) Evaluation of the mock loop’s performance in reproducing the numerical tracings. (3) VAD integration in the mock loop. The numerical model is capable of following parameter changes real-time. When the baroreflex control is activated, the model is capable of re-establish a quasi-complete physiological pressure tracing consistently to the literature. When dealing with the comparison between experimental and theoretical tracings results are really promising, especially at low frequencies. The mock loop is capable of assessing the integration between the numerical patient model and the ventricular assist device, especially because the stroke work changes by the same amount between the numerical and the experimental curves.

**Keywords:** Hybrid mock circulation loop, cardiovascular lumped parameter model, VAD, baroreflex





# Sommario

I dispositivi di assistenza cardiovascolare necessitano di un lungo ed attento processo di validazione prima di essere messi in commercio e quindi impiantati nel paziente. La valutazione delle performance in vitro attualmente viene eseguita utilizzando simulatori idraulici convenzionali, solitamente poco versatili.

Grazie alla collaborazione tra il Dipartimento di Chimica, Materiali ed Ingegneria Chimica "Giulio Natta" (Laboratorio di Meccanica delle Strutture Biologiche, LaBS) e l'Istituto Cardiocentro Ticino, lo scopo della nostra tesi è lo sviluppo di un simulatore ibrido che possa riprodurre forme d'onda realistiche in scenari diversi tra cui il riposo, l'esercizio, l'infarto, con e senza supporto cardiaco. L'utente è facilitato nell'utilizzo da un'interfaccia grafica (GUI) da cui può scegliere sia il tipo di cannulazione (cuore destro o sinistro), la modalità di utilizzo e impostare i valori di contrattilità e frequenza cardiaca.

Le configurazioni tra cui scegliere sono: *Baroreflex control* che indaga a fondo il controllo barocettivo agendo non solo sulle resistenze periferiche e il volume iniziale venoso ma anche sulla frequenza cardiaca e *Device testing* che permette di variare in tempo reale frequenza cardiaca e contrattilità. Lo scopo della prima configurazione è quello di comprendere se le funzioni cardiache stiano migliorando dopo l'impianto del VAD, la seconda configurazione serve invece a valutare l'influenza reciproca tra dispositivo e modello numerico cardiovascolare del paziente. La validazione del simulatore è stata fatta in tre fasi principali: (1) Validazione del modello numerico. (2) Valutazione della capacità del simulatore di riprodurre sperimentalmente i tracciati numerici. (3) Integrazione del VAD. In conclusione, l'interfaccia grafica permette intuitivamente all'utilizzatore di cambiare facilmente frequenza e contrattilità. Il modello numerico segue i cambiamenti dei parametri in tempo reale. Quando il controllo barocettivo è attivo il modello ristabilisce le pressioni quasi fisiologiche che ci aspettiamo dalla letteratura. Il confronto tra tracciati sperimentali e numerici sono promettenti, soprattutto a basse frequenze. Il simulatore permette la valutazione dell'interazione tra il modello cardiovascolare del paziente e il VAD, soprattutto perché il  $\Delta SW$  varia concordemente nei tracciati numerici e sperimentali.

**Parole chiave:** Simulatore ibrido, modello a parametri concentrati, baroriflesso, VAD



# Contents

<b>Abstract</b>	<b>i</b>
<b>Sommario</b>	<b>iii</b>
<b>Contents</b>	<b>v</b>
<b>1 Introduction</b>	<b>1</b>
1.1 Thesis Overview . . . . .	2
1.2 The Cardiovascular System . . . . .	3
1.2.1 Heart Anatomy . . . . .	4
1.2.2 Arterial Pressure Regulation . . . . .	7
<b>2 State of the Art</b>	<b>11</b>
2.1 Hybrid MCLs . . . . .	12
2.2 Computational Models of the CVS . . . . .	14
2.3 Feedback Control Mechanisms . . . . .	18
<b>3 Materials and Methods</b>	<b>23</b>
3.1 Numerical Model . . . . .	25
3.1.1 Circulation Model . . . . .	28
3.1.2 Baroreflex . . . . .	32
3.2 Graphic User Interface . . . . .	35
3.2.1 Main GUI . . . . .	36
3.2.2 Device Testing Mode . . . . .	37
3.2.3 Baroreflex Control Mode . . . . .	38
3.3 Hydraulic Circuit . . . . .	39
3.3.1 Chambers . . . . .	39
3.3.2 Backflow Pump . . . . .	40
3.4 Pneumatic Circuit . . . . .	42

3.5	Electric Circuit . . . . .	44
3.5.1	Data Acquisition Board . . . . .	47
3.5.2	Power Supply . . . . .	48
3.5.3	Pressure Sensors and Control . . . . .	49
3.5.4	Level Sensors and Control . . . . .	53
3.6	Test Protocol . . . . .	59
<b>4</b>	<b>Results</b>	<b>65</b>
4.1	Numerical Model Assessment . . . . .	66
4.1.1	HR Real-Time Variation . . . . .	66
4.1.2	CF Real-Time Variation . . . . .	69
4.1.3	PV Loops: Contraction Fraction and Heart Rate Variability . . . . .	71
4.1.4	Baroreflex Configuration Evaluation . . . . .	73
4.1.5	Aortic Valve Resistance Variation . . . . .	76
4.2	Experimental Pressure Waveforms and PV Loops . . . . .	77
4.2.1	Left Ventricle Simulation . . . . .	77
4.2.2	Right Ventricle Simulation . . . . .	84
4.3	VAD Assessment . . . . .	93
<b>5</b>	<b>Discussions and Conclusions</b>	<b>105</b>
5.1	Numerical Model . . . . .	106
5.2	Experimental Tracings . . . . .	108
5.3	VAD Integration in Mock Loop . . . . .	112
<b>6</b>	<b>Future Developments</b>	<b>115</b>
	<b>Bibliography</b>	<b>119</b>
	<b>List of Figures</b>	<b>125</b>
	<b>List of Tables</b>	<b>129</b>
	<b>Acknowledgments</b>	<b>131</b>

# 1 | Introduction

*In this chapter, a general introduction to our project is provided. The first paragraph deals with the importance of using hybrid mock loops when assessing cardiovascular devices in vitro and it anticipates our goals and perspective. The second part is about the anatomy and physiology of the heart and of the cardiovascular system. The last paragraph of the chapter is an overview of the most important control strategies of aortic pressure: the Frank-Starling and the Baroreflex mechanism.*

## 1.1. Thesis Overview

Active and passive cardiovascular implants need to be tested in accordance with regulatory agencies' standards before their place in the market and the actual implantation on patients. De facto, when dealing with medical products both manufacturers and regulatory authorities need to follow the standards to guarantee safety because it is of vital importance to assess devices reliability previous to the surgical procedure.

The regulatory process can be briefly divided into three phases: pre-clinical studies, clinical studies, and post-market monitoring. Pre-clinical trials include in vitro, in silico and in vivo testing. In silico trials, i.e. modeling and simulations, in recent years, thanks to the improvements in methods and approaches in modeling, have started to provide important evidence for their potential use in the reduction of both animal and human experimentation [1]. That is the reason why currently regulatory agencies such as the US Food and Drug Administration (FDA) and European Medicines Agency (EMA) accept validated computational modeling and simulation as scientific evidence. In this framework, in vitro tests play an important role in the validation and verification process of computational simulations. In addition, in vitro bench testing is required not only to assess the device performance in a well-controlled environment, but also for reducing the use of pre-clinical animal tests that are time-consuming, expensive, and troublesome from an ethical standpoint.

One of the most relevant organizations providing international standards for in vitro testing, working in 167 countries, is the International Organization for Standardization (ISO). In accordance with that, the heart valves assessment guidance is provided by the document ISO 5840-1:2021, while for ventricular assist devices by the standard ISO 14708-5:2020.

In vitro evaluation of cardiovascular devices is usually made using conventional hydraulic mock loops that consist of tubes, reservoirs, valves, connectors and cardiac simulators to simulate hemodynamic conditions. In this framework, an increase in the complexity of the set-up leads to more realistic waveforms of pressure and flow. Of course, usually a trade-off between complexity and accuracy is needed. Furthermore, the versatility is limited because whenever different patient conditions need to be tested, hardware changes are required. The need for a versatile model that can change parameters according to clinical conditions is therefore relevant.

Due to the demands for these requirements to be achieved, our thesis work has been developed. In cooperation with the Department of Chemistry, Materials and Chemical

Engineering “Giulio Natta” (Laboratory of Biological Structure Mechanics, LaBS) and the "Istituto Cardiocentro Ticino", we aim at developing a hybrid mock loop providing realistic hemodynamic waveforms in different scenarios including rest, exercise, infarction, with and without cardiovascular device support. It will be capable of performing in two main configurations so to emphasize its efficiency and versatility:

- Patient recovery assessment including baroreflex control mechanism acting on heart rate, peripheral resistances and unstressed venous volume.
- Cardiovascular device assessment.

Matter of fact, the hybrid mock circulation loop we will present is able to reproduce physiological pressure waveforms. It can be used both to characterize the interaction between the medical device we choose to test (LVAD or heart valve) and the simulated patient and to assess the patient hemodynamic by the analysis of how the natural mechanism of baroreflex acts. In summary, the first configuration can be used to perform the in vitro assessment of the device-patient interactions before proceeding to clinical trials, the latter configuration, instead, to understand if the heart is recovering thanks to its autoregulation mechanisms once the cardiovascular device has been implanted.

In order to evaluate the mock loop performance, it is of great relevance the analysis of pressure-volume loops. In particular, our model provides both a theoretical PV loop, that is the curve that is expected based on the cardiovascular parameters we set at the beginning of the simulation, and a tracing of the experimental PV loop, which should be emulating the theoretical one. However, due to inertias, time delays from signal processing to effectors' actuation, computational restraints within the controller, needed to achieve a tradeoff between precision and stability, the perfect superimposition of simulated and experimental tracings is not easy to achieve, especially when dealing with high frequencies. The evaluation of the stroke work parameter and the average error parameter shows how far those tracings are from one another, i.e. they indicate how performing the mock loop is.

## 1.2. The Cardiovascular System

The cardiovascular system is a complex network that can be described at a glance by mentioning its main components: heart, blood vessels and blood. It has the basic role to transport, through arteries, oxygen and nutrients to tissues and organs but also to carry carbon dioxide and other waste away for disposal through veins.

The cardiovascular system, as shown in Figure 1.1, can be split into systemic and pul-

monary circulation. The former carries oxygenated blood to and returns deoxygenated blood from the tissues of the body, the latter is a closed circuit between the heart and lungs[2]. Concerning the systemic circulation, the oxygenated blood is pumped from the left ventricle into the aorta. The aorta branches into many other major arteries that supply blood to the cells in the parts of both the upper and lower body. These major arteries continue to branch into smaller arteries called arterioles and eventually terminate into capillaries [3]. During its path blood is oxygen-depleted and it carries a variety of cellular waste products. Poorly oxygenated blood flows into the right ventricle through the superior vena cava and the inferior vena cava. It is pumped into the right ventricle and to the lungs through the pulmonary arteries for oxygenation, it then returns to the left heart by the pulmonary veins for distribution to the systemic circulation. In addition to gas exchange, which mainly takes place in the alveoli, pulmonary vasculature also serves for blood filtering and metabolic regulation [4].

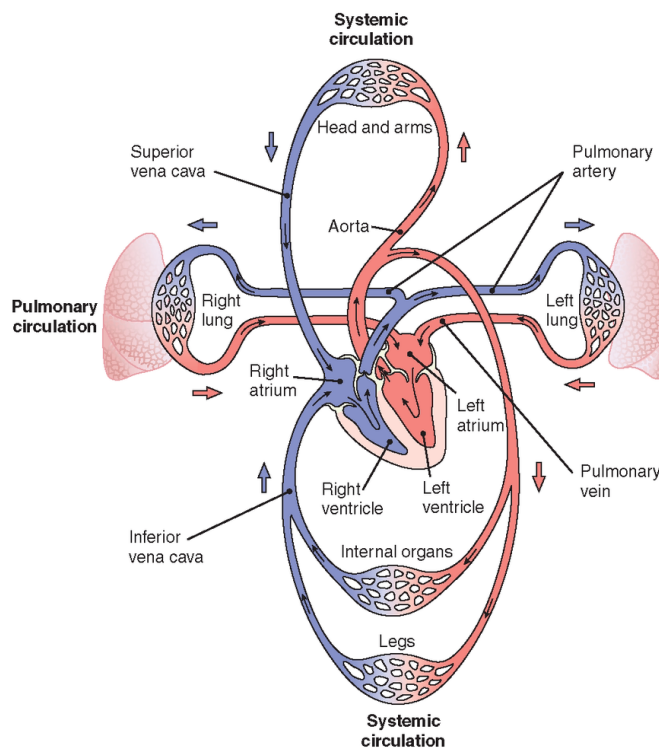


Figure 1.1: Cardiovascular system: systemic and pulmonary circulation.

### 1.2.1. Heart Anatomy

The heart is a muscular organ that acts like a pulsatile pump to continuously send blood throughout the body, thus being the center of the circulatory system. Figure 1.2 shows the heart section: the right and the left side have both an atrium and a ventricle, divided by



the interatrial and interventricular septums. Each atrium is connected with its respective ventricle through an atrioventricular valve: the tricuspid on the right side and the mitral on the left one. Two semilunar valves, called in particular pulmonary and aortic valve, are located between the ventricles and the outflow vessels. During diastole atrioventricular valves offer no resistance to blood flow, during systole they close to prevent backflow into the ventricles. Concerning semilunar valves instead, they both close at the beginning of the ventricular relaxation while they allow blood flux during systole.

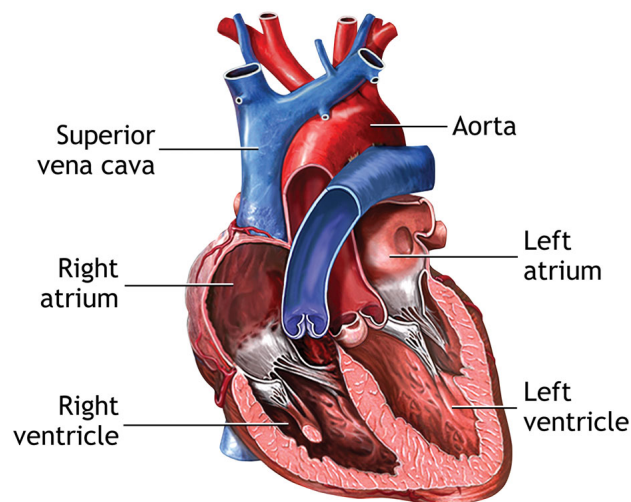


Figure 1.2: Heart anatomic section.

Regarding their anatomy, semilunar valves are malleable cup-shaped structures that are made up of dense connective tissue covered on both surfaces by an endothelium. Each valve inserts into an annulus fibrosus [5]. Both aortic valve and pulmonary valve have three leaflets and, unlike the atrioventricular valves, they do not have chordae tendineae to maintain competency, they open and close only due to blood pressure difference between the atria and the ventricles. On the other hand, the atrioventricular valves consist of lamina spongiosa on the atrial side and lamina fibrosa on the ventricular one. Both these layers are surrounded by endothelial cells [6]. The left atrioventricular valve, also called mitral valve, has only two cusps, while the right atrioventricular is called tricuspid because of the three cusps that characterize it. In both valves, backward prolapse is prevented by the chordae tendineae that connect the papillary muscles of the ventricular wall to the atrioventricular valves.

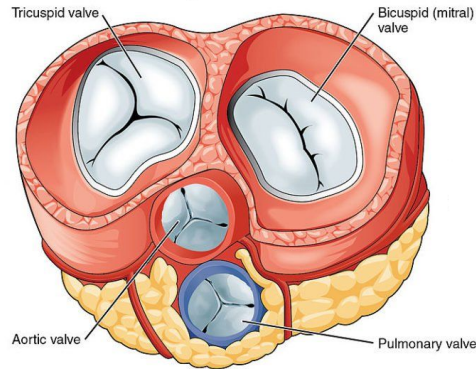


Figure 1.3: Cardiac valve plane.

In Figure 1.4 the cardiac conduction system is shown: the heart itself generates and propagates the electrical impulse that is required to start coordinated atria and ventricles contraction to efficiently pump blood throughout the body. Myocytes in the sinoatrial node activate and the impulse rapidly reaches the atrioventricular node, where it is slowed down.

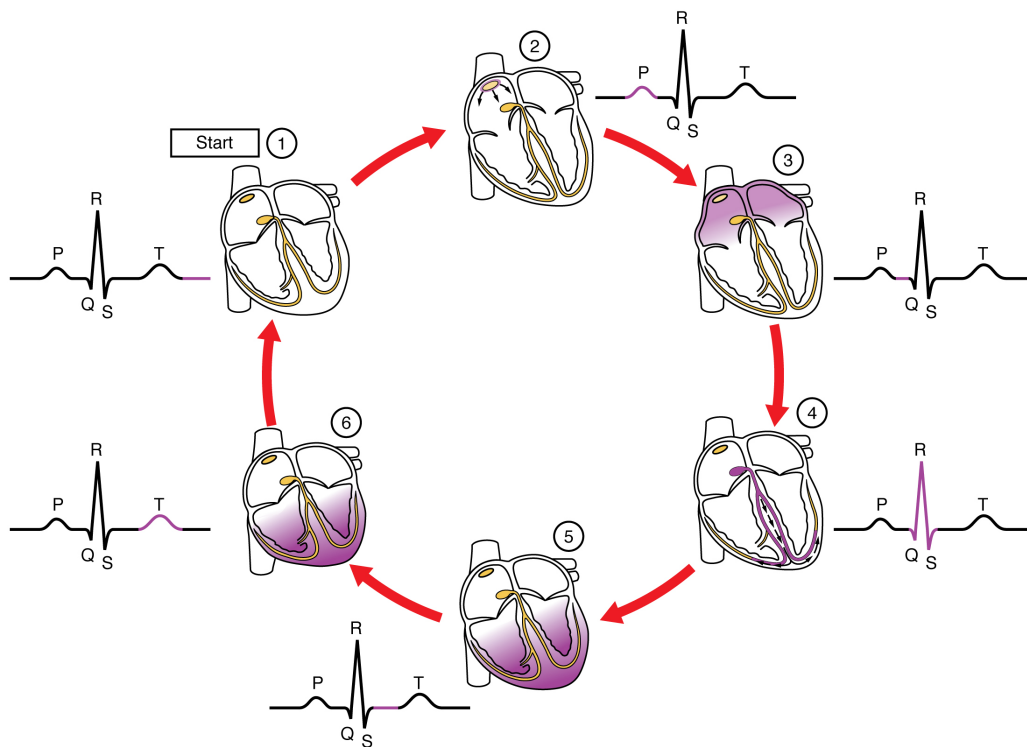


Figure 1.4: Cardiac conduction system: electrical impulse propagation from atria to ventricles and correspondent ECG waves.

The delay is around 100 ms and it allows the ventricles to fill before their activation and contraction. The atrial and ventricular myocardial tissues are electrically isolated from one another except for the His bundle that allows the impulse propagation from atria to ventricles through the Purkinje fiber network[7]. The electric conduction of heart fibers can be recorded from the surface of the skin. A registration of this electrical activity is the electrocardiogram (ECG), widely used in medicine as a diagnostic tool[8]. In the physiological ECG registration, a recurrent wave pattern is present: after the P wave, due to the depolarization of the atria, the QRS complex is present, representing the ventricle depolarization. The last deflection is T-wave corresponds to the ventricular repolarization of the heart[9].

### 1.2.2. Arterial Pressure Regulation

The two main heart feedback control mechanisms are the Starling law of the heart and the Baroreflex.

The Frank-Starling mechanism is the ability of the heart to change its force of contraction and therefore stroke volume (SV) in response to changes in venous return (VR)[10] as shown in Figure 1.5. Owing to this mechanism, when the blood flow increases, the walls of the cardiac muscle stretch, thus leading to an increase in the contraction force[11]. The Frank-Starling mechanism (FSM) has an important role during systolic heart failure. Heart failure causes a decrease of the stroke volume leading to incomplete left ventricular emptying, for that reason we see a downward shift of the left ventricular performance curve. Consequently, the volume of blood that accumulates in the left ventricle during diastole is increased. The amplified residual volume increases the stretch of the myocardial fibers and induces a greater stroke volume with the next contraction via the Frank-Starling mechanism. This allows for better emptying of the enlarged left ventricle and preserves cardiac output[12]. The Baroreflex mechanism (BR), on the other hand, represents the main neural mechanism involved in short-term cardiovascular regulation. The baroreceptors are positioned in the walls of the carotid arteries and of the aortic arch and they are activated by beat-to-beat fluctuations in systemic blood pressure [13]. When a pressure change is detected, baroreceptors stretch, hence enabling their activation. At that moment, they fire the information toward the central nervous system. Thereupon, the autonomous nervous system addresses its signal to the circulatory system to stabilize the arterial pressure to its physiological value.

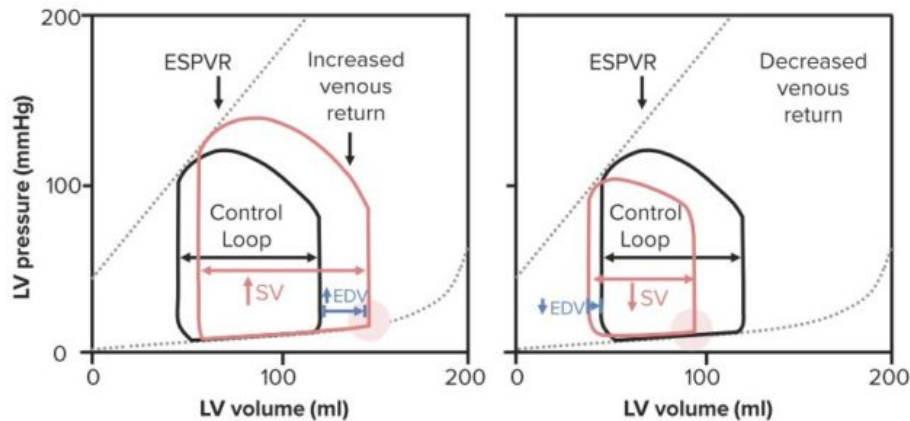


Figure 1.5: Frank-Starling mechanism: an increase in the VR leads to an increase in left ventricular end-diastolic pressure, and so of the SV. Conversely, decreasing VR, SV decreases.

In summary, carotid baroreceptors sense aortic pressure changes and they communicate them as spikes to the central nervous system (CNS). The CNS triggers the sympathetic (fes) or parasympathetic (fev) pathways to activate the regulation effectors, in particular heart rate (HR), elastance (E), systemic vascular resistance (SVR) and unstressed volume in the veins (VV)[14] as sketched in Figure 1.6.

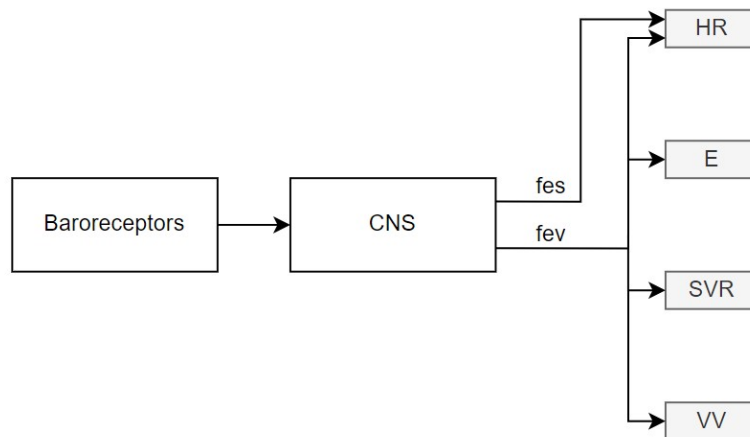


Figure 1.6: Schema of the parameters influenced by the baroreflex mechanism to control arterial pressure. CNS= Central Nervous System, fes= sympathetic pathways , fev= parasympathetic pathways, HR= heart rate, E= elastance, SVR= systemic vascular resistance, VV= unstressed venous volume.

To go into detail, the elastance is a parameter that concerns the contractility of the heart,

and it is the slope of the end systolic pressure volume relation (ESPVR), which will be furtherly discussed in the following chapters. Myocardial elastance, by its simpler definition, is the parameter that defines a relationship between stress, which is the distending force per unit cross-sectional area, and the strain, which is the lengthening that occurs when the stress is applied. It is more of practical usage, though, to relate it to the ratio of the variation of pressure and volume, which is, in other terms, the compliance.

$$E = \frac{dP}{dV} = \frac{1}{\text{compliance}} \quad (1.1)$$

The systemic vascular resistance, also known as total peripheral resistance, is the resistance that the circulatory peripheral system exercises against the blood flow in the system. It determines the mean arterial pressure (MAP), which is the average arterial pressure in one heart cycle, by means of the following relation

$$MAP = CO \cdot SVR \quad (1.2)$$

The unstressed venous volume (VV) is the volume of blood that vessels can bear without exerting stress on their wall. In other words, the filling of the vessels takes time and flow rate to occur, depending also on the compliance of the tunicas (intima, media and adventitia), and when the lumen is saturated, the blood will push the walls and stretch them, increasing the volume, which is defined the stressed venous volume. In the circulation with minimal sympathetic tone, the 25 to 30 % of the blood volume consists of the stressed one, and the remaining is merely unstressed[15].

These phenomena of nervous control bear importance and are worth taking into account because they can lead to a doubling in the cardiac output, on the assumption that the sympathetic nervous system is stimulated, and, specularly, a reduction of it that can horizon to the absence of heartbeat for a few seconds when the vagal parasympathetic system is activated. They operate in everyday life, when we get up from our bed, to prevent a collapse, or whenever bleeding occurs, constricting veins and small arteries to avoid leakage of blood from the wound. Being it a bidirectional behavior, the baroreflex can be regarded as a buffer system for arterial pressure [11]. A schema of the working principle in case of pressure decrease is given in Figure 1.7:

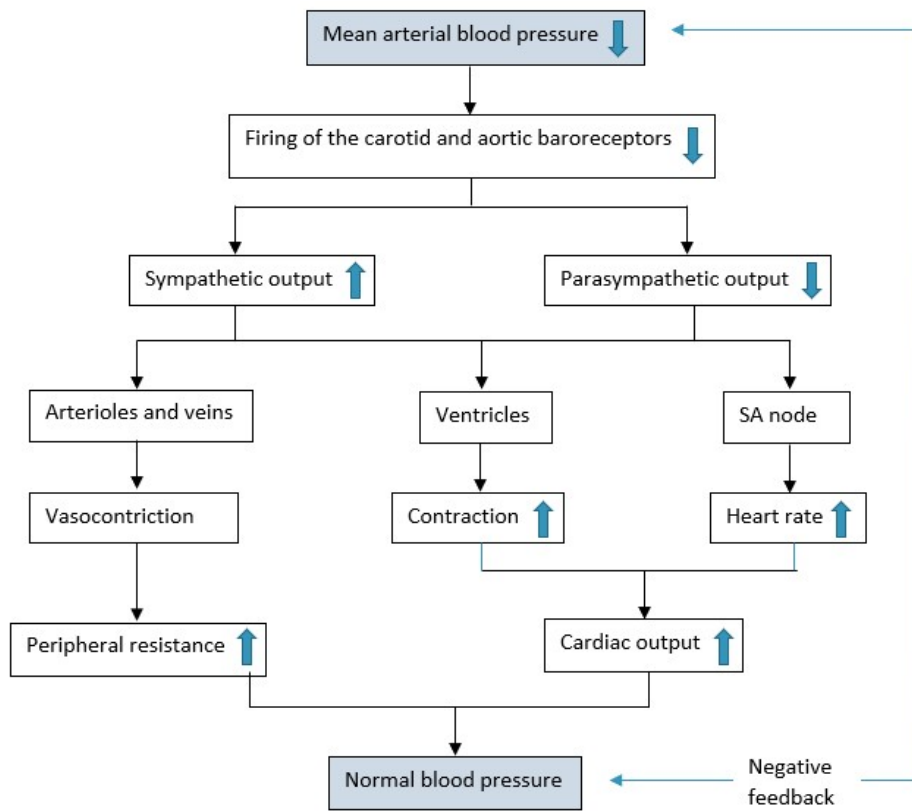


Figure 1.7: Baroreflex mechanism outline considering a pressure decrease.

## 2 | State of the Art

*In this chapter, the state of the art concerning mock loops (MCLs) is provided with a focus on hybrid ones (h-MCLs). Then, an overview of the possible modeling approaches concerning the cardiovascular system is presented investigating both lumped and distributed models. The inclusion in these mock loops of autoregulation mechanisms is investigated in Section 2.3.*

## 2.1. Hybrid MCLs

Mock circulatory loops (MCL) are used for multiple purposes like training and research but first of all, they play a key role in the in vitro assessment of Ventricular Assist Devices (VADs) and other Cardiac Assist Devices (CADs). Purely mechanical mock loops (M-MCL) reproduce the circulatory system using hydraulic or mechanical components but they are indeed constrained by costs, complexity in the building of the setup and low flexibility. On the other hand numerical MCLs (N-MCL), those that exploit lumped parameter models, have absolute reproducibility and controllability, being more flexible than M-MCLs. They are also more cost effective, not requiring a huge number of mechanical components, and more reliable, since they can take into account more districts and more phenomena that act in our body and influence the cardiovascular system. Lumped parameter modeling (LPM) works by clustering a physical system, whose properties are oftentimes space and time dependent, into compartments that do not mean to represent a specific district but to portray a generic behavior that would occur because of those very physical structures. In point of fact, simplifications are needed to meet computational demands [16].

Even if the space distribution of the system is ignored, the system still displays a topology, for example nodes and branches can be used. Each node is characterized by an intensive variable, branches instead represent the flow of extensive variables between nodes. It is rather intuitive to devise an analogy of this scheme to that of an electrical circuit, where electric terminals represent nodes and the electric wiring between nodes represent branches. Being the electric analogy valid, Kirchhoff laws must be respected.

The concept of merging numerical and physical models was exploited in the last years leading to a new concept of circulatory models called hybrid (H-MCL).

Hybrid modeling of the circulatory system is a new branch of biomedical engineering, starting in the late 1990s [17]. H-MCLs are mainly composed of an hardware part and a computational model, the interaction between the physical and the numerical model can be reached acquiring data from sensors and driving actuators using an accurate control system. These mock loops can be used not only to reproduce physiological and pathological patients' clinical condition, but also to assess his recovery in case of assistance. In fact, the greatest strenght of N-MCLs with respect to M-MCLs is the possibility to see how device and patient interact. In this framework, Ferrari et al. [18, 19] have created a numerical model of the left heart, right heart, pulmonary circulation and the systemic venous circulation, and they built an electro-hydraulic interface comprised of a servo amplifier, a DC motor and a gear pump to generate a physical flow rate that matched the



computed one. The hydraulic part, containing a reservoir and a systemic arterial tree was then built, including a silicon rubber tube, to test intra-aortic balloon pump assistance (IABP). Within this framework also Darowsky [17] used their model to simulate pathology of the left ventricle assisted by the pneumatically driven LVAD. The hybrid character of the circulatory model is exploited by two impedance transformers (TR) assigned to the left ventricle and to the aorta that allow the transformation from numerical flow to hydraulic one. The hybrid impedance transformer consists of a electrically controlled flow source (VCFS) designed using a motor driven gear pump (Figure 2.1 (a)). The LVAD connection with TR icons representing hydro-numerical signal conversions is reported in Figure 2.1 (b).

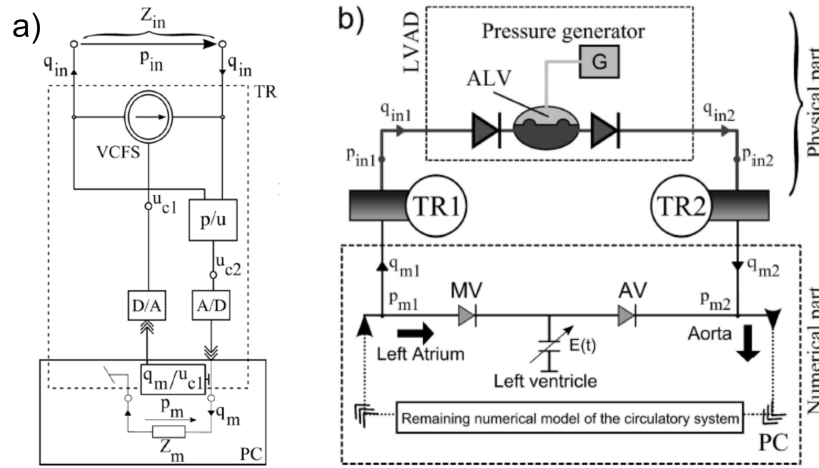


Figure 2.1: Hybrid impedance transformer (a) and circuit including VAD connection (b) as proposed by Darowsky [17]. VCFS=flow source, ALV=artificial left ventricle, TR1=ventricular impedance transformer, TR2=aortic impedance transformer.

Petrou et al.[20] developed a mock loop that has an hydraulic interface composed of four reservoirs which are pressure-controlled, so to enable the interaction of the implant with a numerical CVS. They were able to investigate:(1) aortic valve insufficiency progression during BiVAD support,(2) pulmonary vascular resistance increase during total artificial heart (TAH) support,(3) flow distribution in a total cavo pulmonary connection.

As hitherto stated, the leading reason for the exploitation of hybrid MCL's is their versatility. That is why Kozarski et al.[21] have integrated an electro-hydraulic impedance simulator into a hydraulic section to represent the input impedance of the systemic arterial tree. In many situations, it is impossible to mirror intricate characteristics, like ventricular elastance, with a physical model, thus leading Kozarski et al.[22] to the need for a numerical-physical model for the ventricle. Another application of HMCLs is the

assist devices testing as VADs [23], total artificial hearts (TAH) [14] and rotary total artificial hearts (rTAH)[24]. In that context, the advantage of the hybrid over purely numerical mock loops is the use of the real device instead of a model.

HMCLs can be also used for the evaluation of hemodynamic effects of assist devices in vitro: Timms et al.[25] developed a MCL to replicate the necessary features of the systemic and pulmonary circulatory systems, including pulsatile left and right ventricles (Figure 2.2). This setup has the ability to evaluate the hemodynamic effect of LVAD, RVAD and BiVAD assistance.

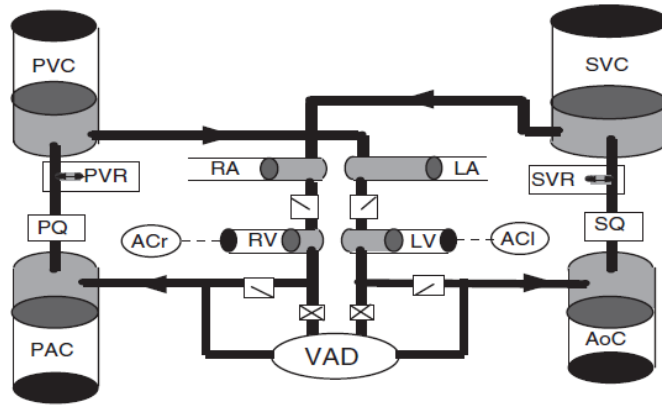


Figure 2.2: Schematic of mock circulation loop used by Timms [25]. ACl=left air compressor, ACr=right air compressor, AoC=aortic compliance, PAC=pulmonary arterial compliance, PQ=pulmonary flow rate, PVC=pulmonary venous compliance, PVR=pulmonary vascular resistance, SVC=systemic venous compliance, SVR=systemic vascular resistance, SQ=systematic flow rate.

## 2.2. Computational Models of the CVS

The computational modeling of the cardiovascular system (CVS) can be structured in several ways, in consonance with the accuracy that is to be achieved. The models can span from the 0D models (known as lumped parameter models) to the 3D models.

Lumped parameter models (LPMs) are models in which it is assumed that the 3-D spatial distribution of the physical quantities in the system can be ignored. It is a way to simplify a spatially distributed physical system considering it as the combination of a finite number of elements characterized by scalar variables describing their status, and parameters describing their properties. Because of the fact that variables are time-dependent, LPMs are associated with Ordinary Differential Equations (ODEs), they are hence 0-D models with respect to space, but 1-D models considering time. The topology of the system,

usually presented in terms of nodes and branches, is needed to explain how the multiple elements interact.

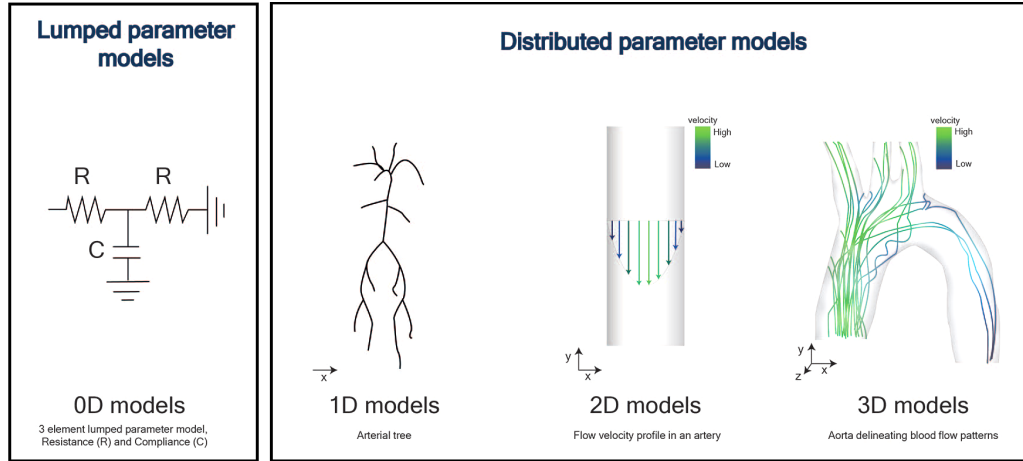


Figure 2.3: Comparison between distributed and lumped parameter models.[16]

The distributed vascular network is modeled as a lumped electrical circuit. This could be done because of the analogies to an electrical circuit, in this context, the hemodynamic parameters can be regarded as electrical parameters: pressure can be regarded as voltage, flow as current, the vessels' resistances as resistors, the vessels' elastic behavior as capacitors.

1D models of the cardiovascular system can discern a pulse wave transmission along one direction, which is useful in a case study where blood interfaces with medical devices such as a stent. The fluid motion is axial and in a compliant pipe, and the coupling of the arterial branches is reached by applying interface conditions of continuity between the single-segment models computed at the previous step [26]. 2D models can be of utility when it comes to the analysis of the velocity gradient in an axial symmetric domain.

A 3D model can furtherly widen the analysis range including real tri-dimensional geometries, like the aortic arch for instance, and studying the local velocity profile along its branches [16]. Inserting geometries implies the need of meshing those districts, which leads to a higher computational demands. Since many vascular diseases can act on large and medium-sized arteries, those may be modeled with the blood as an incompressible Newtonian fluid following the Navier-Stokes equations, and the wall following a nonlinear finite stress-strain relation. Modeling the whole CVS by means of the 3D models is not feasible due to the complexity of the computational domain [26].

Most of the models for the whole cardiovascular system are LPM because they are the least computationally demanding and, if a precise analysis of the geometry of the circulatory

system is not needed, accurate. Hanson et al.[27] modeled the CVS using LPM. They considered the four heart chambers as detached, put into communication by diodes that represent the valves, containing each one a pressure source and a generic impedance, while the aorta and the pulmonary artery are displayed as two passive compartments with a compliance. De Pater et al.[28] built an electrical analog of the CVS with a fourfold pulse generator to mirror the systolic and diastolic cycles. The vessels are approximated as if they were electrical transmission lines with around 600 different sections. This model allows to represent the signal propagation throughout the heart as well, with an astable multivibrator that acts as the sinus node, that will trigger, the univibrators representing the atria and, after applying a delay, the univibrators mirroring ventricles (Figure 2.4). That is how those univibrators become square pulse width generators where each width stands for the contraction time of the heart muscle. Vessels are then represented using a  $\Gamma$ -shaped configuration with an inductance in series with a resistance in a branch and a resistance in series with a compliance in the other (Figure 2.5). Those results were comparable to the in-vivo measurements.

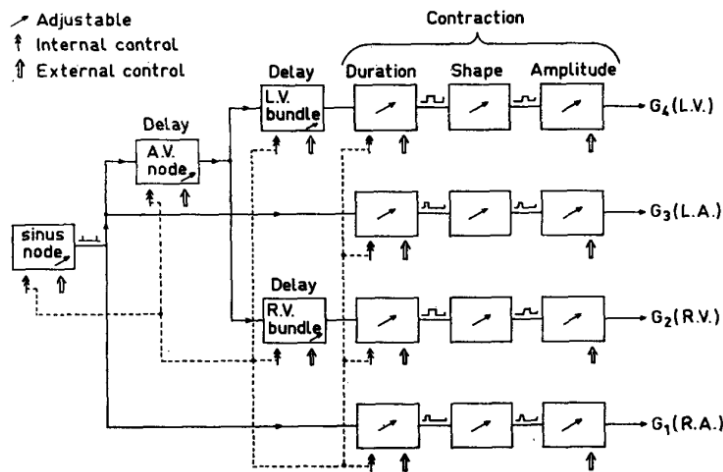


Figure 2.4: Analog of the heart innervation as proposed by de Pater [28]. The generators G1, G2, G3, G4=generators representing the action of the heart muscles.

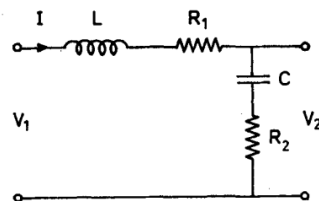


Figure 2.5: Vessel electric analog.

Ferrari et al. [29] used a lumped parameters numerical model including pulmonary and systemic circulation without considering the systemic arterial tree. By evaluating the pressure-volume loops and the pressure waveform of the left ventricle, the model has been considered valid to represent hemodynamic relationships in different conditions. Granegger et al. [30] developed a 0D model of the Fontan circulation without cavopulmonary assistance: they used a time-varying elastance model for the ventricle and Windkessel models for the systemic and pulmonary circulation. Some complete models of all the cardiovascular system have been developed. For example, Gu et al. [31] include systemic circulation, pulmonary circulation, and the heart with four chambers and Abdi et al. [32] which include arteries, veins, capillaries, and heart chambers.

Kiselev et al. [33] built the arterial tree where every single district is built using a 1D model. The equations they used are the following:

$$\partial_t A(z, t) + \partial_z Q(z, t) = 0 \quad (2.1)$$

$$\partial_z Q(z, t) + \alpha \partial_z \left( \frac{Q(z, t)^2}{A(z, t)} \right) + \frac{A(z, t)}{\rho} \delta_z p(z, t) + K_r \frac{Q(z, t)}{A(z, t)} = 0 \quad (2.2)$$

where  $z$  is the spatial variable,  $t$  the time variable,  $A(z, t)$  is the cross-sectional area,  $Q(z, t)$  the blood flow,  $p(z, t)$  is the blood pressure,  $\alpha$  is the Coriolis coefficient,  $\rho$  blood density,  $K_r$  friction coefficient. The model is very accurate and portrays realistic results when it comes to the analysis of the pulse wave profile and the velocity prediction, while it did not show a significant betterment in the prediction of systolic and diastolic pressure, compared to 0D models.

Colacino et al. [34] developed a LPM where left and right ventricles are modeled by nonlinear time-varying elastances. Adopting the time-varying elastance model means that the pressure in each chamber is dependent on its volume, it is controlled by the end-systolic pressure-volume relation (ESPVR), by the end-diastolic pressure-volume relation (EDPVR), and by the contraction function, a piecewise cosine function that describes the contraction progress of the heart chambers.

End-systolic pressure-volume relation (ESPVR) and end-diastolic pressure-volume relation (EDPVR) are respectively (2.3) (2.4):

$$\phi_a = \left[ 1 - \left( \frac{V_{pmax} - V(t)}{V_{pmax} - V_0} \right)^2 \right] \cdot P_{max} \quad (2.3)$$

$$\phi_p = E_{min} \cdot (V(t) - V_0) + \frac{K}{V_{sat} - (V(t) - V_0)} - \frac{K}{V_{sat}} \quad (2.4)$$

Where  $V(t)$  is the instantaneous blood volume,  $V_{pmax}$  is the volume at the peak pressure value,  $V_0$  is the V-coordinate for the elastance curve pivot point,  $P_{max}$  is the maximum pressure,  $E_{min}$  is the minimum elastance,  $K$  is the saturation coefficient,  $V_{sat}$  is the saturation volume.

The equation that relates blood pressure and volume within the ventricle is the following:

$$P(t) = P_0 + \phi[V(t), t] - R_i \frac{dV(t)}{dt} \quad (2.5)$$

where  $V(t)$  is the instantaneous blood volume,  $P(t)$  the instantaneous blood pressure and  $R_i$  the internal ventricular resistance.

The function  $\phi[V(t), t]$ , whose slope is the instantaneous ventricular elastance  $E(t)$ , can be found combining the ESPVR and EDPVR relations in the following equation:

$$\phi[V(t), t] = \phi_p[V(t)] + (\phi_a[V(t)] - \phi_p[V(t)]) \cdot F_{iso}\left(\frac{t}{T}\right) \quad (2.6)$$

where  $F_{iso}\left(\frac{t}{T}\right)$  is the contraction function,  $t$  is the time variable and  $T$  is the cycle period.

As for the arterial systemic and pulmonary afterloads, the model is based on a five component Nordergraaf model with L,C,R parameters, following the work of Guyton [35], while the venous systemic and pulmonary compartments are composed of a resistance  $R_v$  and a compliance  $C_v$ .

## 2.3. Feedback Control Mechanisms

The inclusion of autoregulation mechanisms in hybrid mock heart circulation loops is a difficulty that has to be faced. The main autoregulation mechanisms of the heart are the Frank-Starling mechanism, also known as preload sensitivity of the heart, which regulates, beat-to-beat, the cardiac output (CO), and the baroreflex, that regulates the aortic blood pressure (AoP) within a few minutes[36].

The main focus of this paragraph is the analysis of the literature concerning the baroreflex implementation. One of the first attempt of considering such mechanism in a cardiovascular model was the one of Ottesen [37]: this approach is based on clinically tested theories concerning physiology. The result is a non-linear feedback model with time delay focusing

on heart rate variation. Heart rate was considered as depending on blood pressure, but the feedback concerning peripheral vascular resistance, vascular tone and cardiac contractility on blood pressure was not considered.

In literature, it is clearly visible that the more widely used models are the ones by Colacino [34] and Ursino [38]. These two models were selected to be implemented for the baroreflex control system. A more detailed description of those mechanisms is to be found in Chapter 3.1.2. Here follows a brief description and a state of the art analysis of their use and versatility. Colacino et al. [34] developed a model for baroreflex controlling the arterial systemic and pulmonary resistances with a first-order dynamic. The parameters for his model were taken from the studies of the physiologist Arthur Guyton [35]. The Ursino [38] mathematical model for baroreflex shows how sympathetic and parasympathetic systems interact linearly over the heart period and act on systemic peripheral resistances, systemic venous unstressed volume, heart period and end-systolic elastance. Fresiello et al. [39] analysed the effects of a IABP on the baroreflex, the latter being modeled according to the studies of Ursino [38]. With early inflation and late inflation tests on a hybrid mock loop, it was seen how timing can generate a second pressure peak in diastole, increasing the activity of baroreceptors and inhibit the sympathetic system. Also Mushi et al. [40] implemented the Ursino [38] baroreceptor reflex model to control heart rate, ventricular contractility and systemic resistances. The aim is to obtain the desired cardiac output and systemic vascular resistance, and on that goal the model controls its actuators, which are a centrifugal pump and proportional valves. Cavalcanti et al. [41] have developed their baroreflex model. A three-element Windkessel model was used to build a dynamic relationship between Mean Arterial Pressure (MAP) and Cardiac Output (CO), and then the baroreflex control was applied to the heart rate as a non-linear feedback mechanism. A sketch is proposed in Figure 2.6. A static sigmoid curve correlates the pressure to the afferent tone ( $T_a$ ), then both the sympathetic and parasympathetic divisions are built arranging in series a sigmoidal characteristic curve, which was between  $T_a$  and  $T_s$  (sympathetic tone) for the former division and  $T_a$  and  $T_N$  (parasympathetic tone) for the latter, with a first-order linear dynamic block and a time delay. The heart rate is then evaluated by inter-modulating the sympathetic and parasympathetic tones.

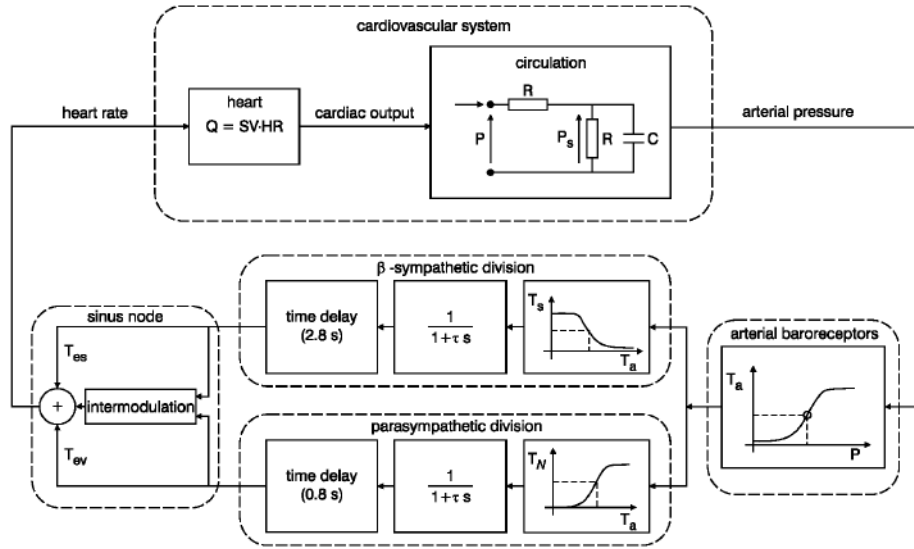


Figure 2.6: Schematic model used to study baroreflex influence on heart rate variability [41].  $P$ =arterial pressure,  $T_a$ =afferent tone,  $T_s$ =sympathetic tone,  $T_N$ =parasympathetic tone.

Both Ochsner et al.[23] and Petrou et al.[20] exploited the model from Colacino et al.[34]: the former for BiVAD and TAH validation including control mechanisms for unstressed venous volume (UVV), systemic venous and arterial resistances, as well as pulmonary arterial resistance, the latter tested a VAD. They used a H-MCL including the baroreflex, which adapted the venous resistances while keeping the heart rate constant. Fresiello et al.[39] analysed IABP effects on baroreflex using a cardiovascular hybrid model. The baroreflex computational representation was mainly taken from Ursino [38]. Jansen-Park et al.[36] implemented both the Frank-Starling mechanism and baroreflex into an M-MCL to understand the interactions between the left ventricle and the L-VAD. Cuenca-Navalon et al.[14] implemented the baroreceptor control into a H-MCL to TAH performance evaluation, neglecting elastance and HR influence on the aortic pressure because the TAH itself should be able to replicate these controls.

Granegger et al.[30] proposed a univentricular model for Fontan patients to investigate the hemodynamic effects of rotary blood pumps including a closed-loop autoregulatory baroreflex based on Ursino [38] model. The same model is then used by Petrou et al.[20] concerning Fontan cases including control for resistances, unstressed volume but also heart rate and elastance.



Table 2.1: Baroreflex control mechanism implementations

	<b>E</b>	<b>HR</b>	<b>UVV</b>	<b>SVR</b>
<b>Colacino[34]</b>	x	x	✓	✓
<b>Ottesen[37]</b>	x	✓	x	x
<b>Mushi[40]</b>	✓	✓	x	✓
<b>Ochsner[23]</b>	x	x	✓	✓
<b>Fresiello[39]</b>	✓	✓	✓	✓
<b>Cuenca-Navalon[14]</b>	x	x	✓	✓
<b>Jansen-Park[36]</b>	✓	✓	✓	✓
<b>Granegger[30]</b>	✓	✓	✓	✓
<b>Petrou[20]</b>	✓	✓	✓	✓

Baroreflex control mechanism implementations: inclusion of Elastance (E), Heart Rate (H), Unstressed Venous Volume (UVV) and Systemic Vascular Resistance (SVR) modifications.



# 3 | Materials and Methods

*In this chapter, all the components of the mock loop are presented. In Section 3.1 the numerical model is presented dealing in-depth with all its components: the circulation model, the baroreflex implementation and the user interface. In the next sections, the hardware part is exploited starting in Section 3.3 with the hydraulic circuit and then explaining the pneumatic and electric main components.*

The mock circulatory loop we are presenting is a hardware-in-the-loop system that exploits a complete numerical cardiovascular model of the circulation, to which, if its interaction with the patient wants to be assessed, a physical cardiovascular device may be paired with. The whole system can be divided into three main parts: software, hardware and the interface between them. The main software part is the numerical model of the circulatory system which allows us to have physiological waveforms. The flow rate of the tested blood pump is fed back into the numerical model, which will alter the pressure values. Software also contains the controllers for pressures and levels, which are proportional-integral (PI) controllers.

Concerning the hardware part, it can be divided into: hydraulic, pneumatic and electrical circuits. The first one, the hydraulic part, is mainly composed of two polymethyl methacrylate (PMMA) tanks that store liquid, in particular we use distilled water. The two chambers can be any anatomic district. In our studies, from the numerical model of the CVS we want to extrapolate pressure waveforms developed by the heart and PV loops, so the two chambers are the left ventricle (LV) and the aorta (Ao), if the left cannulation is chosen, or right ventricle (RV) and pulmonary artery (PA) in case of right cannulation choice. The pressures inside the two tanks are regulated by increasing or decreasing the flow of compressed air inside the tanks via the electrovalves.

The vacuum pump and the vacuum chamber are instead the main components of the pneumatic circuit. The actuators are six proportional solenoid valves: two inlet valves are connected to the compressed air regulator to let the compressed air come into the tanks, while the other four outlet valves are connected to a vacuum chamber to let the air go out of the tanks. To provide pressure and level measurements for feedback, two pressure sensors are installed on the bottom of the two tanks while an infrared range finder is placed on the top surface. The blood pump to be tested is inserted between the two tanks. The communication between hardware and software parts is achieved using a DAQ card as interface: its role consists of sensor data acquisition and communication to the model. In the following chapter, all the main features of the complete set-up will be deeply illustrated.

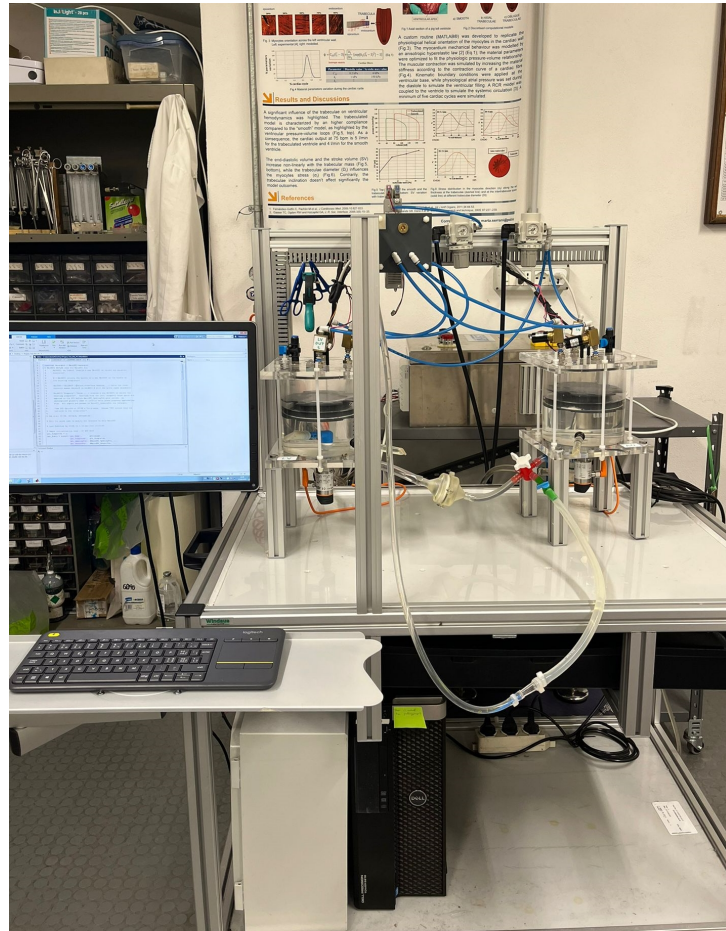


Figure 3.1: Mock loop set-up.

### 3.1. Numerical Model

This section includes all the software information of the hybrid mock loop test bench. An overview of the model is presented in Figure 3.2. The main blocks are:

- **Inputs and Process:** input acquisitions from the level sensors, pressure sensors and flowmeter. The signals coming from the level sensors, which are voltage signals [V] are converted into level measures [m] using look-up tables. Concerning the pressure acquisitions [V] instead, we use the linear fitting curve obtained during the pressure sensor calibration phase to convert voltage into pressure [mmHg or Pa].
- **Circulation Model:** circulatory system model including right heart, systemic and pulmonary circulation and baroreflex control. It is a complete blood circulatory model based on the paper of Colacino [34]. However, the model of the vascular network is not a distributed model but a lumped parameter one. More information in Section 3.1.1.

- **Level Control:** proportional-integral (PI) controller with anti-windup method for monitoring the fluid level in the two tanks. The level controller input is the acquisition from the sensor placed on the top plate of the LV chamber. The controller compensates for unbalances by changing the speed of the backflow pump. To prevent excessive filling or emptying of the ventricular chamber a relay is used to invert the backflow pump flow when the water level in the ventricular is not in the range 85-125 mm. See Section 3.5.4 for a more detailed description.
- **Pressure Control:** two PI controllers, one for the aortic and one for the ventricular pressure. The controllers' inputs are the pressure data from the sensors, on the bottom plate of the tanks. The controllers work on the opening areas of the proportional valves allowing the experimental tracings to follow the the numerical one. See Section 3.5.3 for more details.
- **Safety:** this block ensures the correct functioning of the solenoid valves and of the pump, avoiding reaching unsafe working conditions.
- **Monitoring:** this block is aimed at the visualization of the waveforms of the pressures and blood pump flow rate.
- **Outputs:** pressure and level measurements are converted into digital voltage signals to drive the actuators.

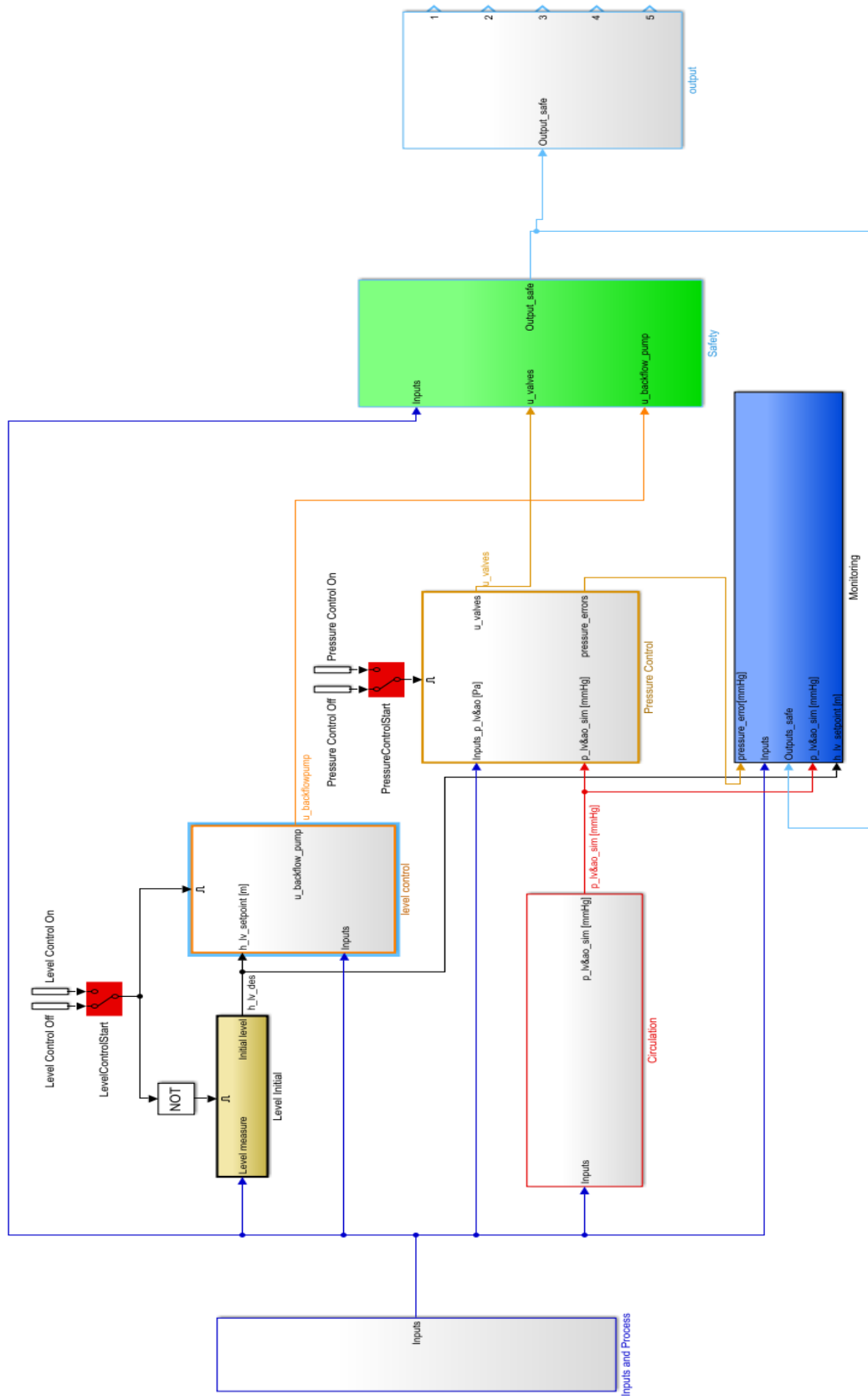


Figure 3.2: Simulink model overview.

### 3.1.1. Circulation Model

Our circulation model follows the theory concerning the LPM, neglecting the 3-D spatial distribution of the physical quantities in the system. What matters to us, in fact, is for the model to be computationally performing, and that it displays correct pressure tracings in diastolic and systolic cycles. Since 1D and 3D models have proved their usefulness when analysing the pulse wave profile or velocity gradient profiles, without revealing great differences in the systolic and diastolic pressure trends, we decided to opt for the 0D model, in accordance with the Colacino [34] model.

In Figure 3.3 the electric analog used in our study is presented.

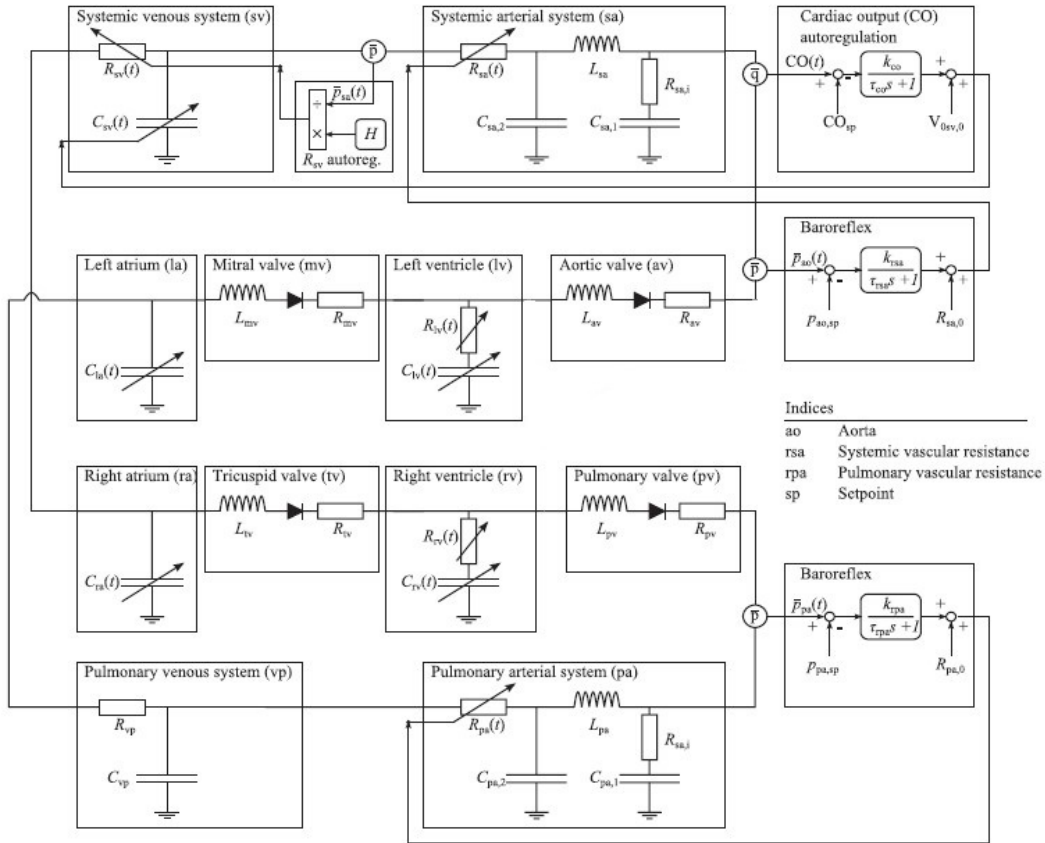


Figure 3.3: Electric analog of the cardiovascular model[23].

Our circulatory system model is implemented in MATLAB/Simulink. Simulink is a software to solve ordinary differential equations (ODEs), and it provides a real-time simulation for this test bench application. The model includes left and right heart, systemic and pulmonary arterial load, systemic and pulmonary venous return.

The main blocks of the model are:



- Left Heart: time-varying elastance model with internal resistance for both atrium and ventricle.
- Right Heart: time-varying elastance model with internal resistance for both atrium and ventricle.
- Pulmonary Circulation: described as a five element Windkessel model for the arterial system and a classic Windkessel model for the venous one.
- Systemic Circulation: the block includes a five element Windkessel model and the systemic vascular resistance autoregulation.
- Baroreflex: implementation of the pressure control mechanism based on the baroreceptors feedback. If the *VAD testing mode* is selected in the GUI this block acts on the venous compliance unstressed volume and peripheral resistances with reference to Colacino et Al. model [34]. On the other hand, if the *baroreflex control mode* is selected, the block is modified including the control of the heart rate accordingly to Ursino model [38].



An important feature of our model is the possibility to change through the GUI sliders two important parameters: heart rate and contraction fraction. The contraction fraction, in particular, is a parameter representing the amount of ventricular contraction with respect to the physiological value, i.e the percentage of the residual ventricular contractility with respect to the physiological end-systolic pressure volume relation. The less the heart is able to contract the smaller will the CF be, ranging between 0 and 1. The contraction fraction is used in our model both to compute the ventricular instantaneous pressure in the time-varying elastance function and to adjust the slope of the ESPVR curve. The end-systolic pressure-volume relation we consider is:

$$\phi_a = [1 - (\frac{V_{pmax} - V(t)}{V_{pmax} - V_0})^2] \cdot P_{max} \quad (3.1)$$

Where  $V(t)$  is the instantaneous blood volume,  $V_{pmax}$  is the volume at the peak pressure value,  $V_0$  is the V-coordinate for the elastance curve pivot point.  $P_{max}$  is the maximum pressure, and that is also an indicator that depends on the ventricle contractility fraction (CF). The instantaneous ventricular pressure equation is instead:

$$\phi = \phi_p - (\phi_a - \phi_p) \cdot F_{iso} * CF \quad (3.2)$$

Being  $F_{iso}$  the contraction function,  $\phi_p$  the EDPVR relation and  $\phi_a$  the ESPVR, as defined by Colacino [34].

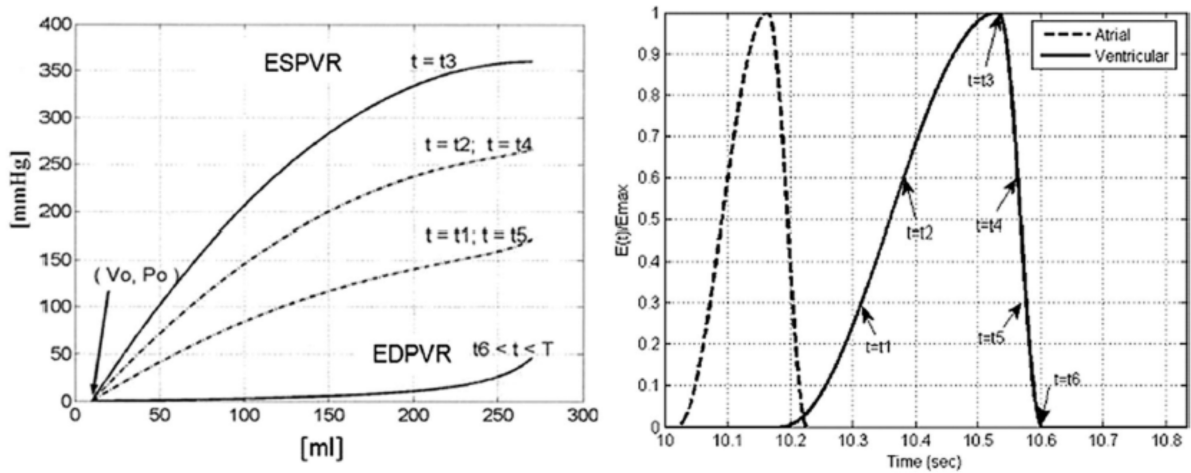


Figure 3.5: (a) LV elastance curves at different time of the cardiac cycle. (b) normalized ventricular and atrial contraction functions [34].

### 3.1.2. Baroreflex

The baroreflex control, being one of the most important pressure regulation mechanisms of the cardiovascular system, has been implemented in this work merging the model of Colacino [34] with the one of Ursino [38]. The Colacino model is exploited to adjust the pulmonary resistance (Rap), systemic peripheral resistances (Ras) and venous compliance unstressed volume (UVV). With the Ursino model we chose to control the heart rate (HR). The control mechanism ruling arterial systemic and pulmonary resistances can be described by a first order dynamic equation in the form of Equation 3.3 choosing the gain value (K) as -0.01 and the time constant ( $\tau$ ) as 1 second. The control mechanism of the venous compliance unstressed volume is a first order controller too with gain -10 and time constant 10 seconds.

$$C(s) = \frac{K}{\tau \cdot s + 1} \quad (3.3)$$

The Ursino model for the baroreflex considers the firing signals that originate when a change in pressure is detected in the carotid sinus. It is appropriate to disembodify the afferent pathway, the efferent sympathetic and parasympathetic pathways, and the response of the diverse effectors. The afferent pathway is described by a first-order linear differential equation with a static gain and a rate-dependent gain (Equation 3.4), followed right after by a sigmoidal static function (Equation 3.5).

$$\tau_p \cdot \frac{d\tilde{P}}{dt} = P_{cs} + \tau_z \cdot \frac{dP_{cs}}{dt} - \tilde{P} \quad (3.4)$$

$$f_{cs} = [f_{min} + f_{max} \cdot \exp(\frac{\tilde{P} - P_n}{k_a})] / [1 + \exp(\frac{\tilde{P} - P_n}{k_a})] \quad (3.5)$$

Here  $\tau_p$  and  $\tau_z$  are the time constants for the real pole and the real zero in the linear dynamic block.  $P_{cs}$  is the carotid sinus pressure,  $\tilde{P}$  is the output variable of the linear dynamic block (having the dimension of a pressure),  $f_{cs}$  is the frequency of spikes in the afferent fibers,  $f_{max}$  and  $f_{min}$  are the upper and lower saturation of the frequency discharge,  $P_n$  is the value of intrasinus pressure at the central point of the sigmoidal functional, and  $k_a$  is a parameter with the dimension of pressure, related to the slope of the static function at the central point.

The efferent pathways, both sympathetic and parasympathetic, behave in accordance with a monotonically decreasing exponential static curve (Equation 3.6) for the sympathetic

activity, and an analogue increasing one for the parasympathetic (Equation 3.7).

$$f_{es} = f_{es,\infty} + (f_{es,0} - f_{es,\infty}) \cdot e^{-k_{es} \cdot f_{cs}} \quad (3.6)$$

Here  $f_{es}$  is the frequency of spikes in the efferent sympathetic nerves,  $k_{es}$ ,  $f_{es,0}$ , and  $f_{es,\infty}$  are constants.  $k_{es}$  regulates the exponential decay,  $f_{es,0}$ , and  $f_{es,\infty}$  represent the initial value and the asymptotic value of  $f_{es}$  when  $t$  tends towards infinite.

$$f_{ev} = [f_{ev,0} + f_{ev,\infty} \cdot \exp(\frac{f_{cs} - f_{cs,0}}{k_{ev}})] / [1 + \exp(\frac{f_{cs} - f_{cs,0}}{k_{ev}})] \quad (3.7)$$

Here instead,  $f_{ev}$  is the frequency of spikes in the efferent vagal fibers,  $k_{ev}$ ,  $f_{ev,0}$ ,  $f_{ev,\infty}$  are constant parameters (akin to the ones for  $f_{es}$ ) and  $f_{cs,0}$  is the central value. The response of the effectors depends on both the activities. The generic response to the sympathetic action is comprised of a delay, a logarithmic static function and a linear first-order dynamics, whilst the response to the parasympathetic changes in the static function is no more logarithmic, but linear and monotonic. The equations that establish that behavior are the ones listed below:

$$\sigma_{T,s}(t) = \begin{cases} G_{\theta} \cdot \ln[f_{es}(t - D_{\theta}) - f_{es,min} + 1] & \text{if } f_{es} \geq f_{es,min} \\ 0 & \text{if } f_{es} < f_{es,min} \end{cases} \quad (3.8)$$

$$\frac{d\Delta\theta}{dt}(t) = \frac{1}{\tau_{\theta}} \cdot (-\Delta\theta(t) + \sigma_{\theta}(t)) \quad (3.9)$$

$$\theta(t) = \Delta\theta(t) + \theta_0 \quad (3.10)$$

These equations stand true for the control implementation of E, SVR, UVV according to Ursino. That's why in the equations there's a  $\theta$ , that represents in a general way one of those three parameter that we are wishing to control.  $\sigma_{\theta}$  is the output of the static characteristic,  $\tau_{\theta}$  is the time constant,  $D_{\theta}$  is the mechanism's latency.  $F_{es,min}$  is the minimum sympathetic stimulation,  $\Delta_{\theta}$  is the control parameter change caused by sympathetic activity. and  $G_{\theta}$  is a constant gain factor that can be positive or negative. Our interest though lies on the implementation of the heart rate control according to that model. Concerning the HR control, we need to take into account two different activities that should be balanced: the vagal and the sympathetic. The equations ruling heart period changes induced by sympathetic stimulation ( $\Delta T_s$ ) are obtained starting from the

previous equations, using Equation 3.11 instead of 3.9. The response to vagal activity is instead linear with the efferent frequency (Equation 3.12, 3.13). Finally, the heart period is obtained by assuming a linear interaction between the sympathetic and parasympathetic responses.  $T_0$  is the heart period without considering cardiac innervation.

$$\frac{d\Delta T_s(t)}{dt} = \frac{1}{\tau_{T,s}} \cdot [-\Delta T_s(t) + \sigma_{T,s}(t)] \quad (3.11)$$

$$\sigma_{T,v}(t) = G_{T,v} \cdot f_{ev}(t - D_{T,v}) \quad (3.12)$$

$$\frac{d\Delta T_v(t)}{dt} = \frac{1}{\tau_{T,v}} \cdot [-\Delta T_v(t) + \sigma_{T,v}(t)] \quad (3.13)$$

$$T = \Delta T_s + \Delta T_v + T_0 \quad (3.14)$$

The values chosen for the parameters are reported in 3.1:

Table 3.1: Baroreflex control mechanism parameters.

Carotid Sinus Afferent Pathway					
$P_n = 92$ (mmHg)	$k_a = 11.758$ (mmHg)	$f_{min} = 2.52$ (spikes/s)	$\tau_z = 6.37$ (s)	$f_{max} = 47.78$ (spikes/s)	$\tau_p = 2.076$ (s)
Sympathetic Efferent Pathway					
	$f_{es,\infty} = 2.10$ (spikes/s)	$f_{es,0} = 16.11$ (spikes/s)	$f_{es,min} = 2.66$ (spikes/s)	$k_{es} = 0.06$ (s)	
Vagal Efferent Pathway					
	$f_{ev,\infty} = 6.3$ (spikes/s)	$f_{ev,0} = 3.2$ (spikes/s)	$f_{cs,0} = 25$ (spikes/s)	$k_{ev} = 7$ (s)	
Effectors					
$G_{Emax(lv)} = 0.47$ (mmHg/(ml $\cdot\nu$ ))	$G_{Emax(rv)} = 0.28$ (mmHg/(ml $\cdot\nu$ ))	$E_{max(lv0)} = 2.39$ (mmHg/ml)	$E_{max(rv0)} = 1.41$ (mmHg/ml)	$\tau_{Emax} = 8$ (s)	$D_{Emax} = 2$ (s)
$G_{Ts} = -0.13$ (s/ $\nu$ )	$G_{Tv} = 0.09$ (s/ $\nu$ )	$D_{Ts} = 2$ (s)	$\tau_{Ts} = 2$ (s)	$D_{Tv} = 0.2$ (s)	$\tau_{Tv} = 1.5$ (s)

Parameters used in the baroreflex control mechanism in accordance with Ursino[38]. G: mechanism strength, f: frequency,  $\tau$ : time constant, D: time delay, E: elastance, P: pressure, k: constant. Subscript s stands for sympathetic, subscript v vagal instead.  $T_0=0.58s$ .

## 3.2. Graphic User Interface

Practicality is pivotal when it comes to the usage of hybrid mock loops. It would be far too complicated for a user to dig into the code and debug all the implemented blocks, not to mention that the whole computational structure relies on interdependencies among blocks, which means that even a little change in a parameter can lead to malfunctioning and miscalculations. That is why having a graphic user interface (GUI) proves to be much more friendly to those who are willing to run the model. It will display step by step all the possible operations that the user may wish to do, and it will show results in real-time, more specifically the PV loop and the pressure trends of the ventricular pressure and the aortic pressure in time, both numerical and experimental. The software simulates the entire circulation system, therefore the chambers could represent any anatomical district

of our interest, by readjusting the outputs we wish for. For our purposes, the software also allows tests to be performed between the right ventricle and the pulmonary artery. Since the aforementioned configuration of the left ventricle and aorta is much more used, due to the fact that loads and pressures are higher in the left heart, and thus even the likelihood of valve issues and the need for assistance devices is, we will keep talking about left ventricle and aorta for the sake of simplicity.

### 3.2.1. Main GUI

The first graphic user interface in Figure 3.6 is intended to present to the user the cannulation options, which can occur between the left ventricle and the aorta or between the right ventricle and the pulmonary artery. Since the software replicates the whole cardiovascular system, the GUI allows the immediate visualization of the waveforms the user is interested in studying. When toggling between the two options, the image on the right side varies in order to underline the district of choice. On the bottom, several recommendations and clarifications will appear, and the user has to follow those instructions to prevent the test bench from damaging and to output reliable results.

The two buttons show the possible test modalities to run. The *Device Testing* button aims at testing devices, while the *Baroreflex* button is to use the baroreflex mode to test the autoregulation capabilities of the heart when assisted with a cardiovascular device.

This latter test may be useful to see if a certain patient can recover its residual heart function after the implantation of a cardiac support device. It is worth mentioning that the baroreflex control has also been implemented in the *Device Testing* mode, but it will act on the mere systemic resistances and on the unstressed venous volume, while in the *Baroreflex* mode it was implemented to retro-act on the heart rate too. In conclusion, in the *Device Testing* mode we wish to enable the user to edit the values of heart rate and contraction fraction while the simulation is running from the keyboard, while in the baroreflex mode there will be starting values for those parameters, and they will be modified throughout the simulation.



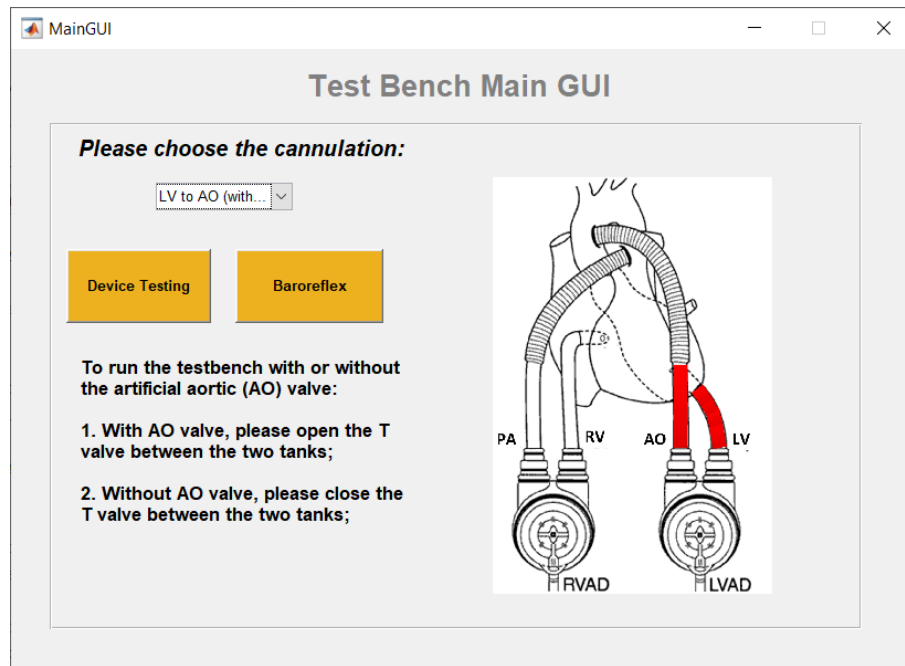


Figure 3.6: GUI in cannulation choice. Here the LV and AO cannulation has been selected, and by pressing one of the two buttons the testing mode is chosen.

### 3.2.2. Device Testing Mode

Once the *Device Testing* mode is chosen, this GUI (Figure 3.7), called *ComTest*, will pop up. The buttons are meant to be clicked in subsequent order, starting from *Load System* and going downwards. When clicking the *Load System* button, parameters of the lumped model will be initialized, according to Colacino [34] and Ursino [38] works. Two frames on the right side are prepared to display the experimental pressure tracings (upper frame) and the theoretical and experimental PV loops (lower frame). Once the loading is complete, the *Start* button will be enabled, and the simulation will begin. The pressure waveforms will be shown in the upper right figure, whilst the pressure-volume loops and the end-systolic pressure volume relation (ESPVR) and end-diastolic pressure volume relation (EDPVR) curves will be displayed in the lower right figure. Then, the *Start Level Control* can be clicked (the GUI will consequently enable the buttons that may be used, and disable them when they are no more of use). The *Level Control* button will control the backflow pump, which will adjust the water level in the tanks.

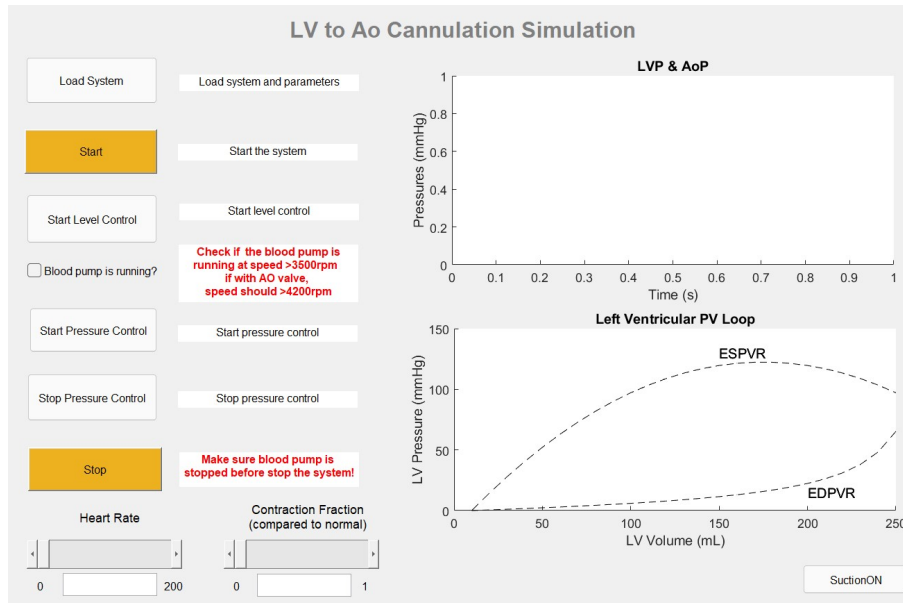


Figure 3.7: GUI if *Device testing* mode is chosen for the left cannulation: the user can manually set and change in real time heart rate and contraction fraction.

After the blood pump (VAD) is running, that button can be ticked, and then it will move on to the pressure control. The pressure control will activate the solenoid valves, connecting the two tanks to the vacuum chamber and to the compressed airline. The inflow of compressed air through the inlet solenoid valved will increase the tank pressures, while the vacuum produced by the vacuum pump and maintained into the vacuum chamber can be delivered through the two outlet valves. These intertwining phenomena emulate the systolic and diastolic pressures. When the simulation is to be stopped, click *Stop Pressure Control* and then *Stop* buttons.

The two sliders at the bottom of the window were inserted in order to change HR and CF during the simulation, without having to act directly on the code. When they are not activated by the user, the setpoints are 90 bpm for the heart rate and 0.34 for the contraction fraction. The heart rate can vary from 0 (total absence of heart beat, hence death), and 200 bpm (tachycardia), while the contraction fraction can vary from 0 (total infarction) to 1 (physiological). The user may either move the slider to regulate it or insert a specific value right below that. Those values can be changed throughout the simulation to appreciate the real-time curve changes from one condition to another.

### 3.2.3. Baroreflex Control Mode

The baroreflex control, as previously stated, is not meant to assess a specific device, but its main purpose is to test the residual abilities of the heart and to check if an improvement

in patient's conditions occurs after the implantation of the device. Here the user can not insert the values of heart rate and contraction fraction, because the code will modify them during the execution. The initial values of HR=90 bpm and CF= 0.34.

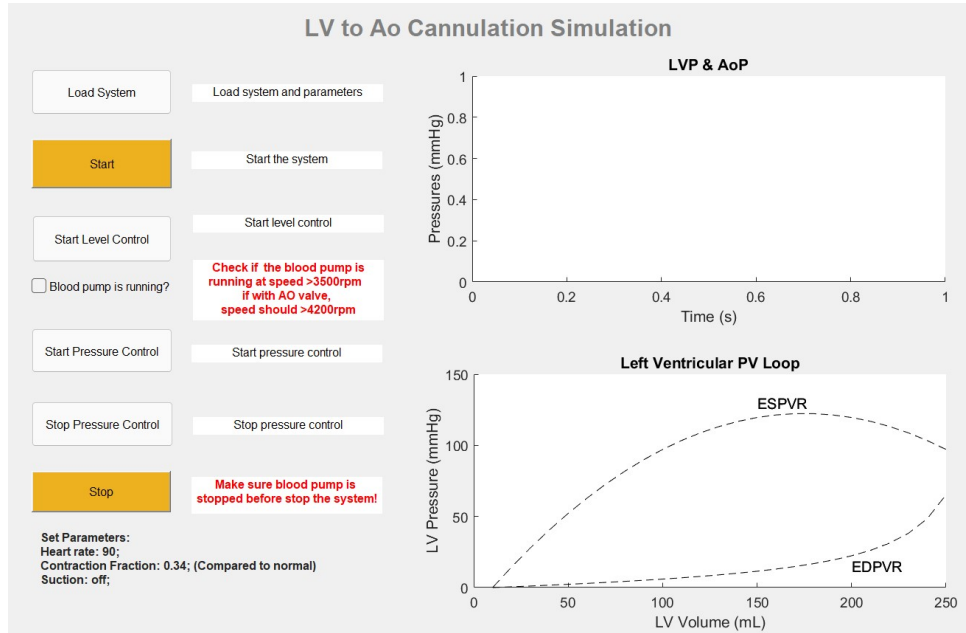


Figure 3.8: GUI if *Baroreflex* mode is chosen for the left cannulation: heart rate and contraction fraction values are fixed. There are not sliders because once the initial values are fixed, the baroreflex acts to adjust peripheral resistances, unstressed venous volume and HR too.

### 3.3. Hydraulic Circuit

The hydraulic circuit is an important part of the mock loop since without the presence of fluid flowing into the circuit we will not be able to physically reproduce flow rates and to characterise the cardiac assist device in the set-up. For the sake of simplicity the fluid flowing in our mock circulatory loop is distilled water instead of blood. In general, the hydraulic circuit's main components are the two water tanks, the backflow pump and of course all the connections and tubes that are needed. In the next two sections, we will deal in a more detailed way with this part focusing on the two chambers and on the pump.

#### 3.3.1. Chambers

As we just said, one of the most relevant components of the hydraulic circuit are the two chambers: two PMMA cylinders that are meant to store distilled water. The tanks can be any anatomic district of interest, making the mock loop versatile. In our case, we use a

numerical model of the cardiovascular system and the two chambers we are going to study will be the left ventricle (LV) and the aorta (Ao), if the left cannulation is chosen, or right ventricle (RV) and pulmonary artery (PA) in case of right cannulation choice. The two chamber's dimensions are 164x150mm. The two tanks are in contact thanks to two tubes: the first one is useful in order to insert the valve (aortic valve if we are considering the left cannulation), the second for connecting the VAD. Then, two connectors are present on the bottom of the chambers so as to easily insert the pump tubings.

### 3.3.2. Backflow Pump

The backflow pump is a self-priming volumetric progressive cavity pump (MAE25-1, CSF inox, Italy) with an electrical control cabinet that is connected to the tanks.

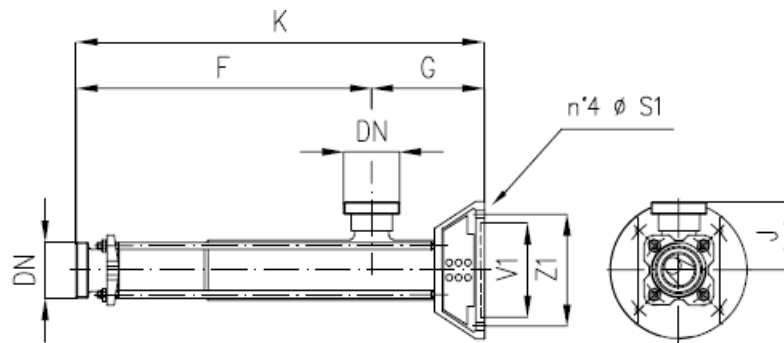


Figure 3.9: Pump overall dimensions.  $DN=$ ,  $F=236$  mm,  $G=115$  mm,  $V1=70$  mm,  $Z1=85$  mm,  $J=62$  mm.

In normal conditions, the pump is current-controlled. Since the output of the numerical method would be a tension, a voltage-current converter was placed in the cabinet to reach that goal. Its purpose is to supply fluid from the Ao tank to the LV tank when the water level is decreasing, which is due to the water stream from the LV to the Ao chamber. Its functioning is driven by the implemented software based on the level measured by the level sensors. In fact, the software will send a voltage signal that will be translated into pump rotations. As the signal increases in magnitude, the frequency of the motor increases following a linear relationship, as in Figure 3.10.

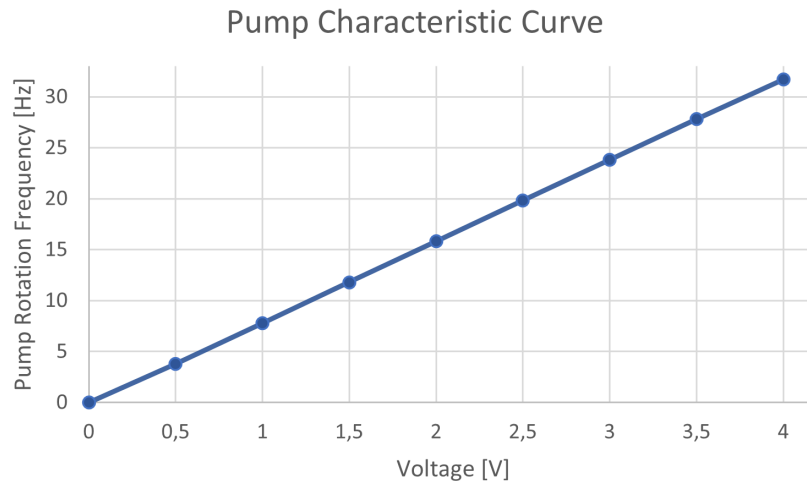


Figure 3.10: Relationship between voltage and pump rotation frequency.

Between the motor (B20 IL-2-2, WISTRO, Germany) and the pump itself a helical gearbox (FRD-02 B3H FE19, VARVEL, Italy) is placed. To correlate the rotation frequency issued to the motor to the actual rotations per minute we need to take into account a gear reduction coefficient of 2.08. Here in Table 3.2 are the values we found to convert the frequency of the motor to the actual rotations per minute.

Table 3.2: Frequency-rpm relation.

Frequency [Hz]	Rotations per minute [rpm]
10	288
20	576
30	864
40	1152
50	1440

In Figure 3.11 instead we can see how the flow rate correlates to the rotations of the pump. We chose this backflow pump because it is of the smallest size out of the industrial progressive cavity pumps analysed, it's not too encumbering and it can elaborate flow rates up to 17.5 l/min (at rpm=1400). Considering that the average cardiac output is about 5 l/min, this pump is well capable of refilling the chambers in case they empty too much. It interacts well with our fluid, and it could eventually work with fluids whose

density is closer to the blood one (3 cP). For our purposes, the pump can well withstand the head losses in the mock loop.

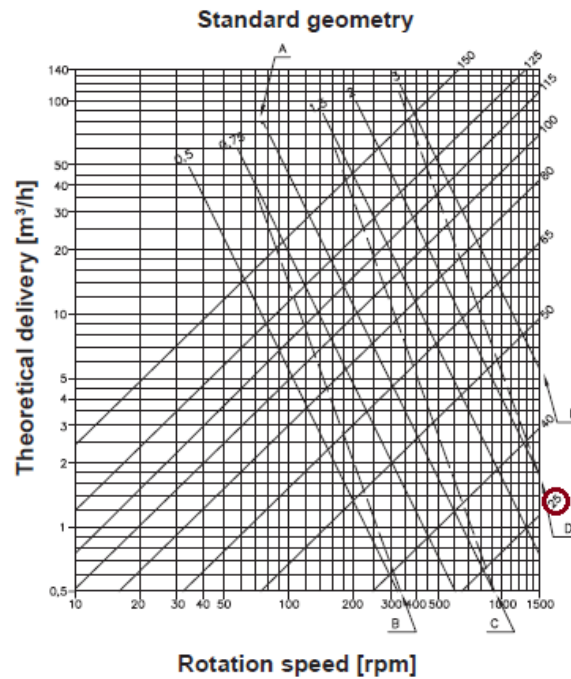


Figure 3.11: Backflow pump datasheet.

The pump can work both in automatic and in manual mode. In the case of manual mode choice, the direction of rotation of the pump can be set manually by acting on the switch on the control panel, the rotational speed instead can be changed by acting on the arrows on the display. In automatic mode, instead, the speed of the pump is driven by the numerical model and the clockwise rotation is the starting setting. The switch to anti-clockwise rotation is done automatically by the relay when needed, so when the ventricle tank is too filled.

### 3.4. Pneumatic Circuit

The pneumatic circuit is meant to deliver pressurized air to the chambers in order to allow flow rate from one chamber to another. A sketch is presented in Figure 3.14. First of all, the compressed air tube needs to be connected to a filter regulator (LFR-1/4-D-MIDI - 40  $\mu\text{m}$ , Festo, Germany). This component is a combination of an air filter and a pressure regulator in a single unit, this is the best choice for our application in order to reduce encumbrance and leaks related to connections. The regulator is equipped with a manual

throttle valve, which ensures that the pressure inside of the filter regulator chamber will be kept at a steady value throughout the simulations. The airway will then be split into two routes owing to two regulators (AR30, SMC, Japan). The air with 0.4 MPa will be provided to a vacuum ejector (ZL112-K15LOUT-E26L-Q, SMC, Japan) which will generate a vacuum pressure that rounds -80 kPa. The ejector working principle is based on the Venturi effect: compressed air is supplied through a connection and it flows through a Venturi nozzle that allows both compression and acceleration. The accelerated air slows down once again after the nozzle and vacuum is obtained. The characteristics of the vacuum ejector taken from the datasheet, are reported in Figure 3.12, Figure 3.13.

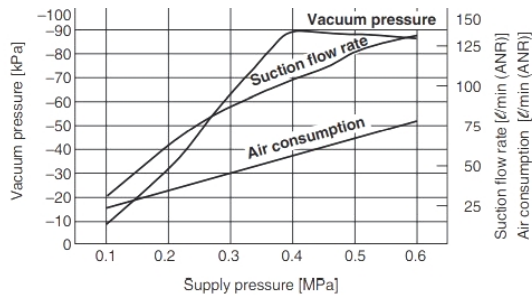


Figure 3.12: Exhaust characteristics.

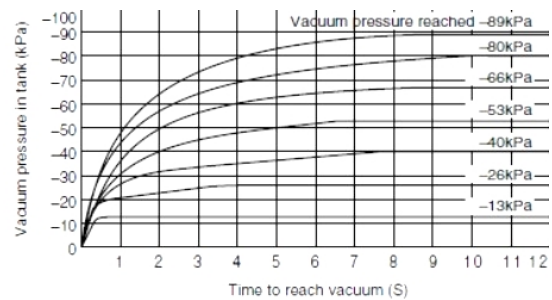


Figure 3.13: Time to obtain vacuum (1 l tank and 0,4 MPa supply pressure).

The vacuum chamber downstream the pump ensures that the pressure will be kept at the desired value, it needs to store a volume of 1L in order to reach a pressure of -80 kPa. It is needed as a buffer, to store a negative pressure that can be transmitted to the LV and Ao tanks via two proportional solenoid valves (PVQ33-5G-40-01F, SMC), which are placed on the upper plate covering the LV and Ao tanks, that can be open or closed as to administer the required pressure to the tanks.

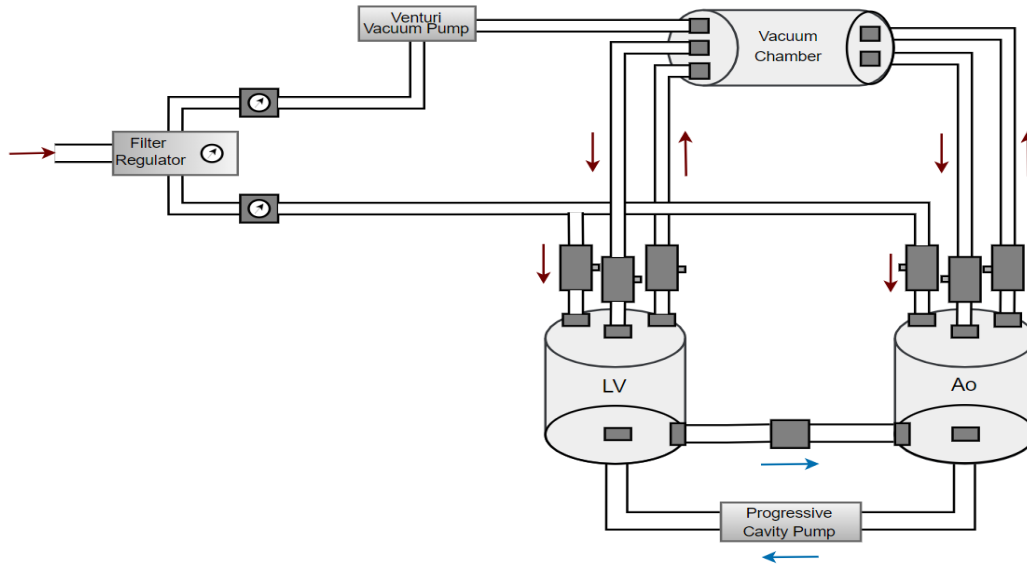


Figure 3.14: Pneumatic main components overview.

### 3.5. Electric Circuit

The electrical circuit is the core of the entire mock loop. It spans from sensors to drivers and to data acquisition. The key that enables communication from the physical measures to the software environment is the data acquisition board. De facto, the presence of the pressure sensors, the level sensors and a flow meter (HT110R, Transonic Systems Inc, USA) serve as input for the numerical software. Those are, in substance, transducers that convert physical quantities in voltage that is provided to the model. After the model is fed, it will trigger the actuators, which are comprised of proportional valves and the pump. An overview is proposed in Figure 3.15.

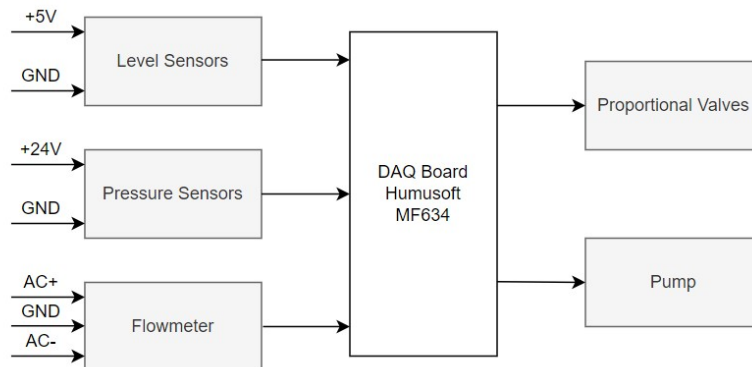


Figure 3.15: Electric schema.



The wiring of the test bench is shown in Figure 3.16 where all the connections between the parts are shown. The two extension boards of the Humusoft DAQ used for acquiring sensor signals and sending control signals are depicted: the X1 board(TB621) acquires sensor signals and it drives the pump while the X2 board(TB621) drives the opening and closing of the solenoid valves.

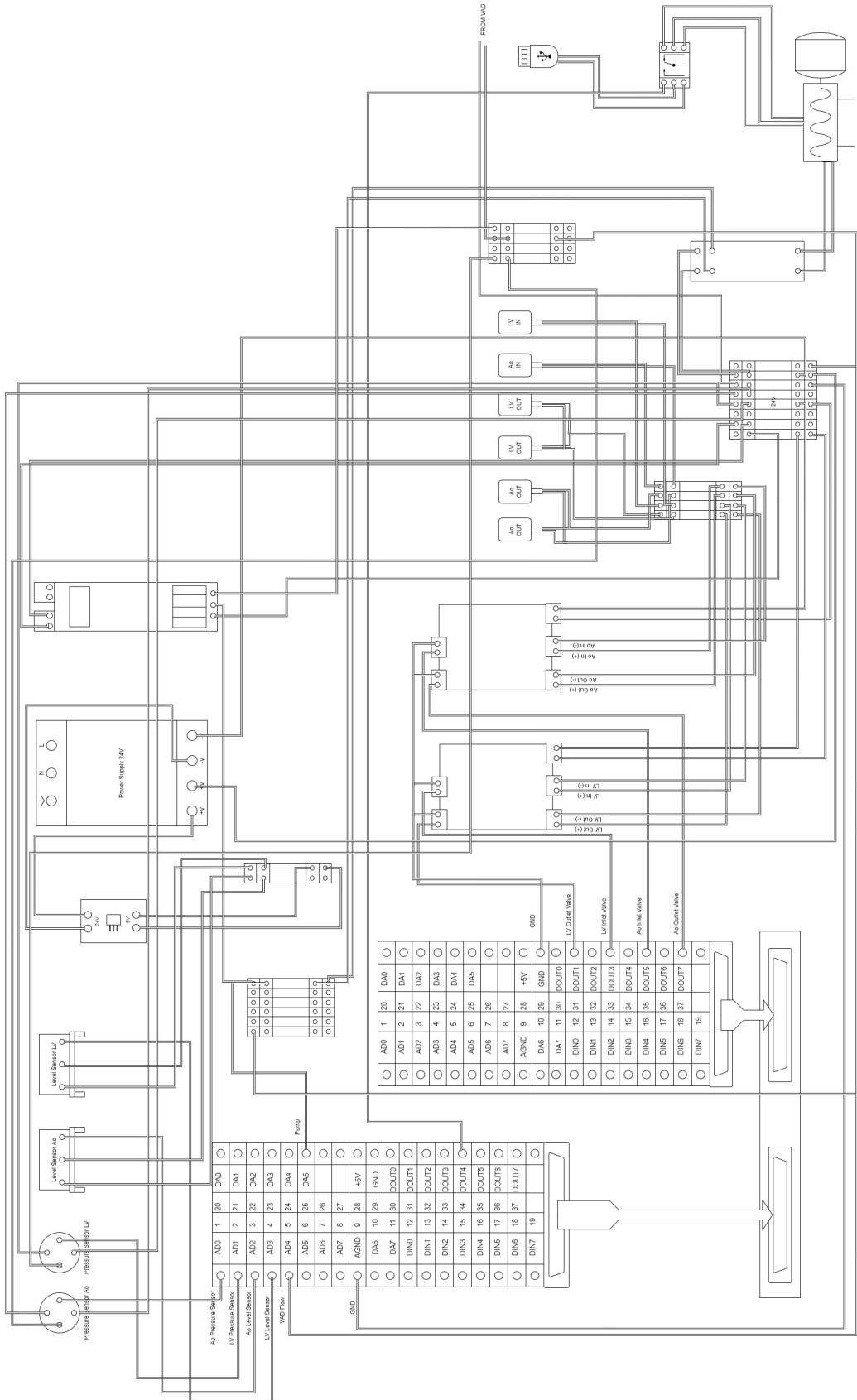


Figure 3.16: Electrical Wiring Schematic.

### 3.5.1. Data Acquisition Board

As stated before, the data acquisition board (DAQ) is really the brain of the hybrid mock loop. The Humusoft MF634 Multifunction I/O card is designed for the need of connecting computers to real world signals. The MF634 contains 8 single-ended channels 14 bits A/D converter with simultaneous sampling of all channels, 8 independent 14 bit D/A converters, 8 bit digital inputs and 8 bit digital outputs, 4 quadrature encoder inputs and 5 timers. The card is designed for standard data acquisition and control applications and optimized for use with Real-Time Windows Target for Simulink. The signals emitted from the sensors are capable to communicate with the computer only via DAQ cards. For our purpose, we have exploited two different terminal boards, as shown in Figure 3.17,3.18.

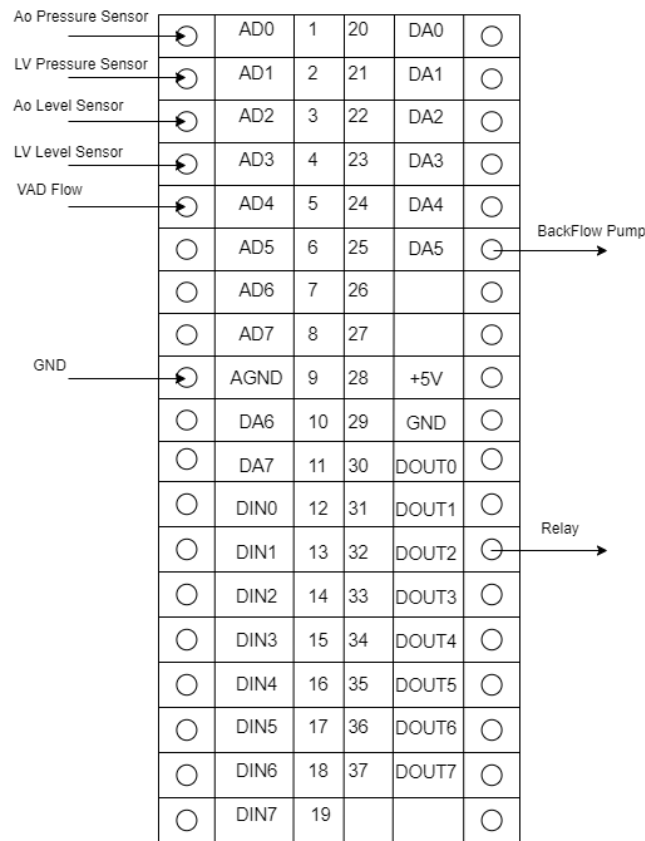


Figure 3.17: Humusoft X1 Extension Board.

○	AD0	1	20	DA0	○
○	AD1	2	21	DA1	○
○	AD2	3	22	DA2	○
○	AD3	4	23	DA3	○
○	AD4	5	24	DA4	○
○	AD5	6	25	DA5	○
○	AD6	7	26		○
○	AD7	8	27		○
○	AGND	9	28	+5V	○
○	DA6	10	29	GND	⊖ → GND
○	DA7	11	30	DOUT0	○
○	DIN0	12	31	DOUT1	⊖ → LV Outlet Valve
○	DIN1	13	32	DOUT2	○
○	DIN2	14	33	DOUT3	⊖ → LV Inlet Valve
○	DIN3	15	34	DOUT4	○
○	DIN4	16	35	DOUT5	⊖ → Ao Inlet Valve
○	DIN5	17	36	DOUT6	○
○	DIN6	18	37	DOUT7	⊖ → Ao Outlet Valve
○	DIN7	19			○

Figure 3.18: Humusoft X2 Extension Board

The first board is connected to pressure sensors (AD0, AD1) and level sensors (AD2, AD3), inputs of the Simulink model. The output of the numerical model (DA5) is used to drive the pump. The second board is instead used to drive the four solenoid valves. Those are connected to the digital outputs, since they are controlled with impulses and not analog signals. The role of those electrovalves is to open and close to provide an inflow of pressurised air from the compressed air channel or an outflow towards the vacuum chamber.

### 3.5.2. Power Supply

Because of the presence of several kinds of actuators and sensors, different supplies of energy are required. That source of energy is provided by one power supply (SDR-240, Mean Well, Taiwan) that can yield 24VDC and another one (TDK-LAMBDA DPP480-48-1, TDK, Japan) that provides 48VDC. Our level sensors (GP2Y0A41SK0F, Sharp, Japan) instead only need 5VDC. That is why we manufactured a small circuit to allot that voltage. On the grounds of that, we build a linear voltage regulation circuit welding a diode in series with a capacitor, a linear voltage regulator (L7805ACV, STMicroelectronics, Switzerland),

and another capacitor onto a small prototyping PCB board (10 mm x 7 mm). In this way not only were we sure that the output would be 5VDC, but also stabilization of voltage was kept thanks to the presence of the capacitors. The electric scheme of the linear voltage regulator can be found in Figure 3.19. The pressure sensors, the valve drivers and the vacuum pump required 24VDC. Owing to that, we used power distribution blocks to obtain enough 24VDC channels where to wire cables to supply power. The 48VDC admission channel is unused for now, but it can be useful in future applications.

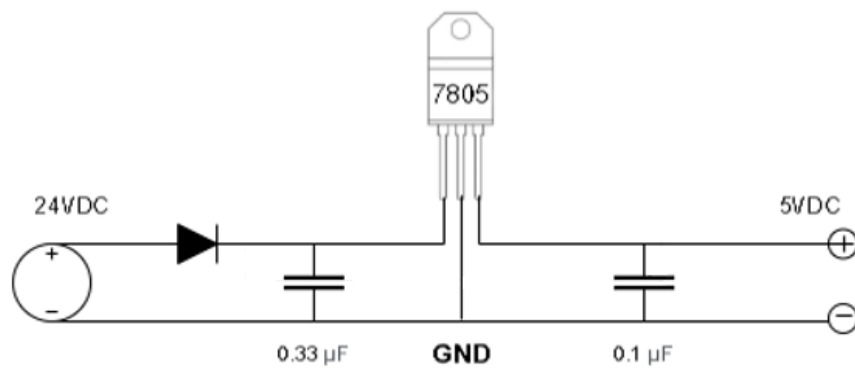


Figure 3.19: 24VDC to 5VDC voltage regulation circuit.

### 3.5.3. Pressure Sensors and Control

A pressure sensor (PN2069, IFM Electronic, Germany) is positioned under each chamber to continuously display the operating pressure. This type of pressure sensor has a measuring range spanning from -375 mmHg to +375 mmHg, which suits biomedical applications, where it is unlikely to reach peak pressure values higher than 200 mmHg. Its response is linear, so the output voltage will vary according to the input pressure linearly as shown in the datasheet in Figure 3.20.

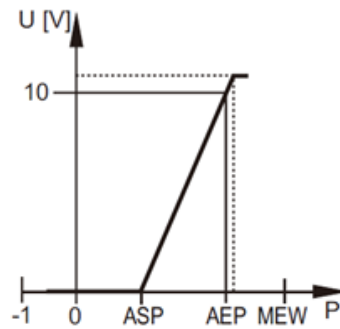


Figure 3.20: Linear Voltage Pressure Relationship. P=pressure, ASP=analog initial point in which the sensor measures 0 V, AEP=final analogue point with output 10 V and MEW=limit value.

However, the pressure sensors showed an offset when unloaded, so we took that into account in order to make sure that the input pressure in the software would be the real value. The data were gathered and collected in the Table 3.3.

Table 3.3: Pressure and voltage measurements to obtain pressure sensors operating curve.

	LV		Ao	
	Pressure [mmHg]	Sensor Vout [V]	Pressure [mmHg]	Sensor Vout [V]
<b>1</b>	2.971	2.783	3.301	3.04
<b>2</b>	3.888	2.805	4.255	3.065
<b>3</b>	4.255	2.815	4.622	3.078
<b>4</b>	5.135	2.838	5.539	3.1
<b>5</b>	5.722	2.85	6.126	3.113
<b>6</b>	6.602	2.87	7.006	3.135
<b>7</b>	7.556	2.895	7.96	3.16
<b>8</b>	8.547	2.915	8.877	3.185
<b>9</b>	8.84	2.925	9.17	3.19
<b>10</b>	9.317	2.94	9.537	3.2

Then, with a linear fitting, which, as expected, interpolated perfectly the expected linear behaviour of the pressure sensors, with an R-squared value very close to 1 ( $R_{LV}=0.9988$ ,  $R_{Ao}=0.995$ ) we portrayed the two curves that represent the Voltage-Pressure relationship

for the left ventricle in Figure 3.21 and the aortic valve in Figure 3.22. The root mean square error (RMSE) calculated for the left ventricle was 0.07 while the RMSE for the aortic chamber was 0.11. The average percentage error, which we calculated as the mean deviation from the real values and the values of our linear interpolation was 0.8% for the LV and 1.6% for the Ao.

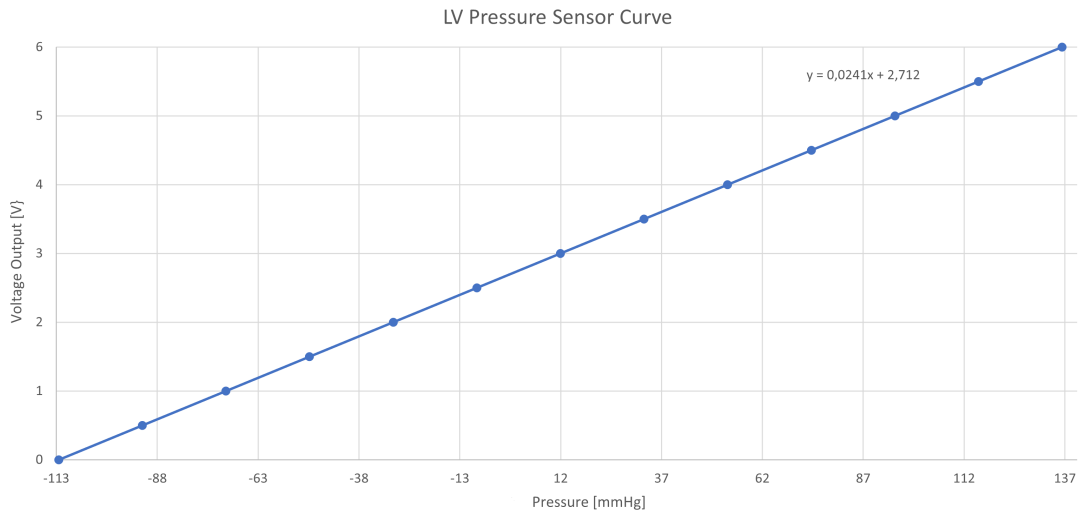


Figure 3.21: Left ventricle pressure sensor curve relating voltage and operating pressure.

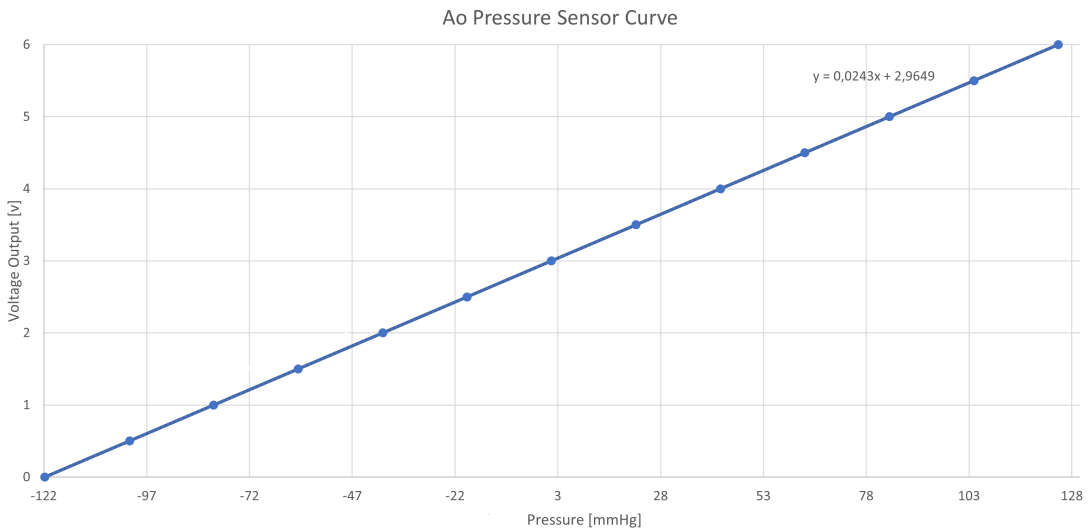


Figure 3.22: Aortic pressure sensor curve relating voltage and operating pressure.

Concerning the pressure control, two Proportional-Integral (PI) controllers are used because of the need for a continuous and modulated control of the pressures in the two tanks. The structure of the PI is almost the same but different gains are used, the values

are reported in Table 3.4.

The controller works on the opening areas of the proportional valves according to the difference between the numerical model pressures and the measured pressure data from the pressure sensors. Concerning the left ventricle, a proportional gain-scheduling control (P-scheduling) is added to improve the performance of the pressure control when the setpoint varies dramatically. Gain-scheduling control is in fact a simple adaptive control system that adjusts controllers' parameters accordingly to the process dynamics.

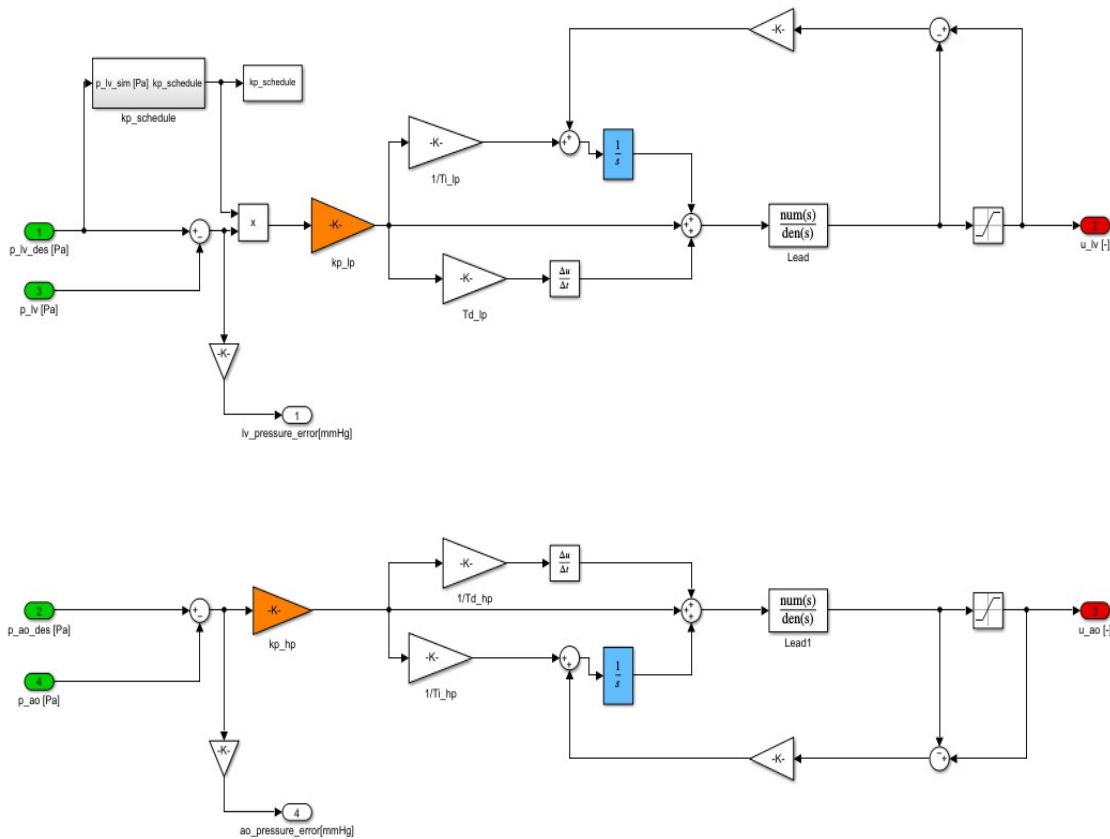


Figure 3.23: Simulink model of the pressure controller.

Table 3.4: Pressure controllers parameters.

	LV	Ao	RV	PA
$K_p$	50e-5	35e-5	5e-5	25e-5
$T_i$	0.2	0.5	0.35	0.35
$K_{aw}$	9	9	8	8

$K_p$ =proportional gain [1/mmHg],  $T_i$ =integral time [s],  $K_{aw}$ =anti-windup coefficient.



### 3.5.4. Level Sensors and Control

The levels of the two chambers are measured using two analog output distance measuring sensors. These sensors are alimented by 5 VDC and their efficient range of measure is between 4 cm and 30 cm. In particular, a diode produces light with a specific wavelength in the infrared spectrum, when an object is close to the device, the light will bounce back on a detector and the intensity of this light will be measured. This data is used to determine the distance of the object, which in our case is a floating plate. Two placed are used, one inside each chamber, and the distance between the top surface of the floater and the sensor is measured.

The operating curves are obtained relating the water level, measured using a millimeter ruler, and the output voltage. Measures are reported in Table 3.5.

Table 3.5: Level and voltage measurements to obtain level sensors operating curve.

	LV		Ao	
	Water Level [cm]	Sensor Vout [V]	Water Level [cm]	Sensor Vout [V]
<b>1</b>	12.30	2.713	12.40	2.820
<b>2</b>	11.75	2.475	12.00	2.680
<b>3</b>	11.35	2.280	11.45	2.440
<b>4</b>	10.80	2.105	10.60	2.155
<b>5</b>	10.25	1.921	10.20	2.025
<b>6</b>	9.65	1.805	9.75	1.915
<b>7</b>	9.05	1.695	9.25	1.805
<b>8</b>	8.10	1.561	8.55	1.690
<b>9</b>	7.05	1.455	7.20	1.540
<b>10</b>	6.25	1.400	6.20	1.468
<b>11</b>	5.15	1.345	5.80	1.440

The fitting process is performed using third polynomial curves of which the expressions and the R-squared values, as a measure of how close our data points are to the regression line, are reported in Figure 3.24,3.25.

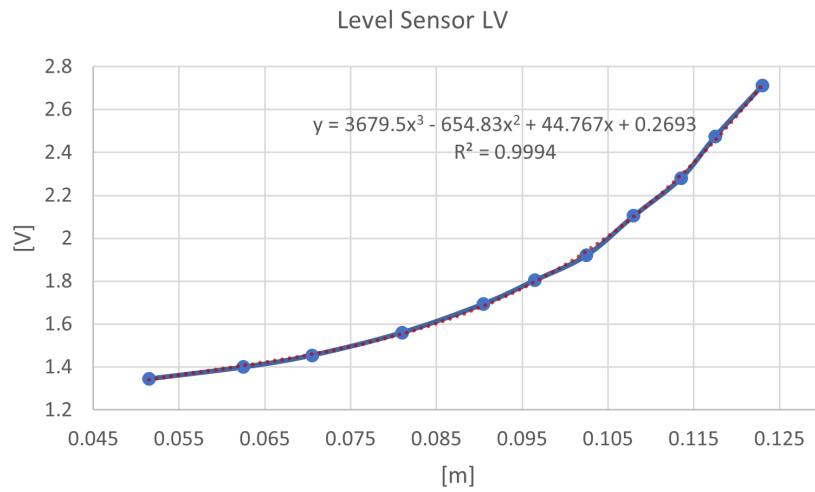


Figure 3.24: Left ventricle level sensor curve relating voltage and water level

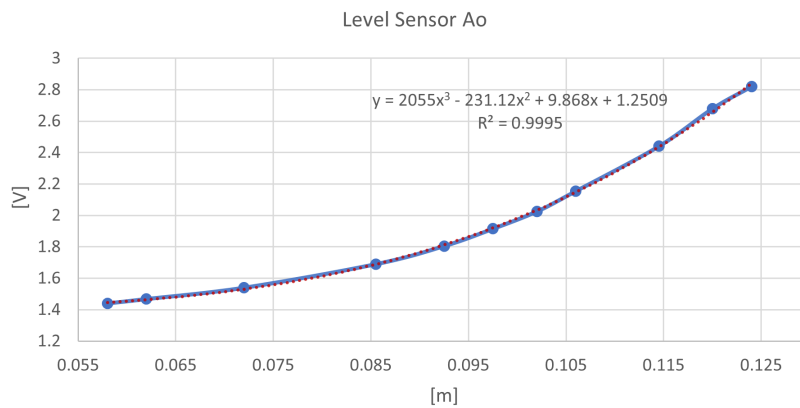


Figure 3.25: Aortic level sensor curve relating voltage and water level

To avoid overflow or suction of the two tanks, level control is introduced to keep the fluid volume balance between the two tanks and so a constant flow through the VAD. The level control acquires the level data from the LV level sensor and then it compensates for unbalances by changing the speed of the backflow pump (more details about the pump are to be found in Subsection 3.3.2). We arranged the set-up accordingly to the work of Ochsner[23], as in the sketch in Figure 3.26. The backflow pump is placed between the tanks and elaborates fluid opposedly to the VAD.

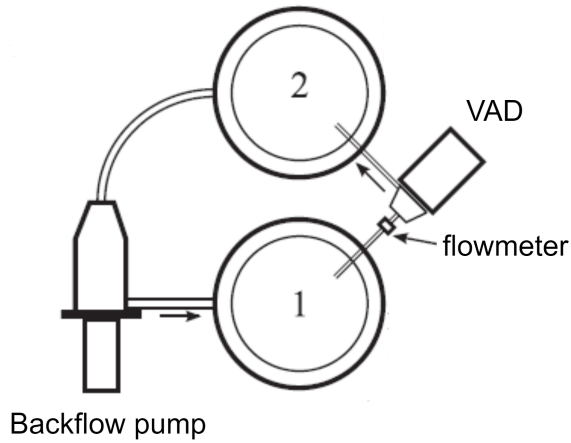


Figure 3.26: Overview of the VAD and the backflow pump connecting the two chambers (1 and 2).

PID controllers are used when the error needs to be continuously monitored. The general equation for a PID controller is:

$$u(t) = K_p \cdot e(t) + K_i \cdot \int_0^t e(t)dt + K_d \cdot \frac{de(t)}{dt} \quad (3.15)$$

A Proportional-Integral (PI) controller, a variation of the PID including only the proportional and integral terms, with anti-windup method is implemented for our task.

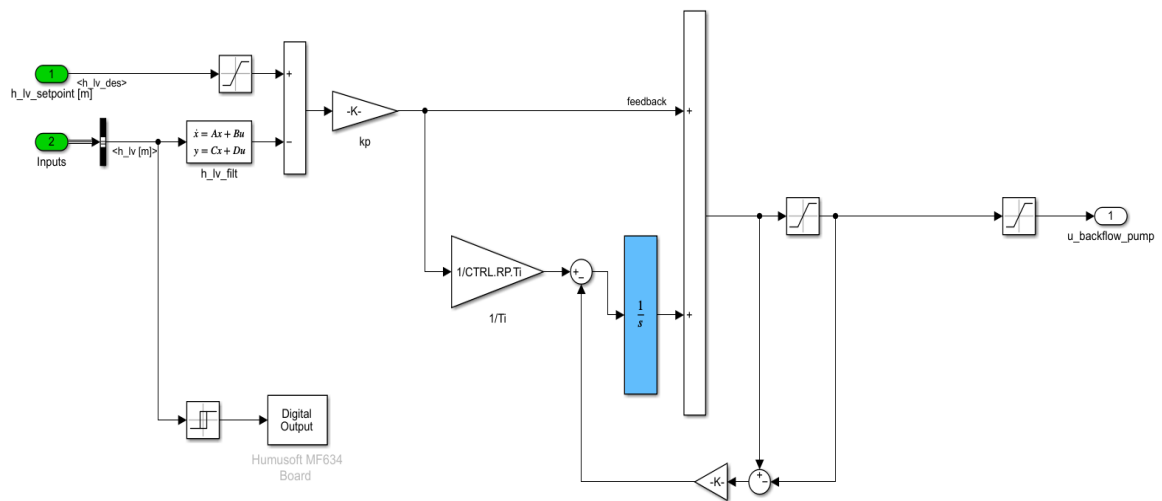


Figure 3.27: Simulink model of the level controller.

The parameters used in the model are reported in Table 3.6.

Table 3.6: Level controller parameters.

<b>Proportional Gain</b>	150 (1/m)
<b>Integral Time</b>	2 (s)
<b>Anti-windup parameter</b>	5

To safeguard the well functioning of the circuit, we decided to implement a further control mechanism. That was achieved with the insertion of a relay (JQC-3FF-S-Z, Tongling, China) to control the flow direction of our progressive cavity backflow pump. Indeed, in normal conditions, the backflow pump is supposed to restore the water level of the left ventricle by means of the level controller. When functioning, the mock loop will produce a pressure difference that will issue a flow from LV to Ao, so the control level will logically be required only to bring the fluid back to the left ventricle to prevent the shortage of fluid in the LV tank. What may happen, in extreme conditions, is that the regurgitation fraction of the valve is too high that the water will flow back from the valve towards the left ventricle tank. In that case, the pump by itself is inadequate to restore the water levels, because it would work unidirectionally from Ao to LV. The implementation of a relay that we decided to apply comes in handy for this reason. The external structure of the relay can be seen in Figure 3.28.



Figure 3.28: External structure of the relay.

The voltage supply it requires is 5VDC. We decided to exploit the USB port, which delivers exactly that tension in a stable way, to power it. The digital output port triggers the switch and activates the relay. The internal circuit, and thence its functioning, can be seen in Figure 3.29

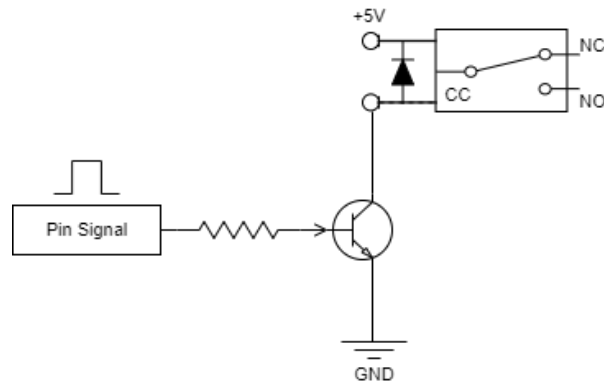


Figure 3.29: Internal circuit of the relay.

When the pin signal, i.e. the digital output, is zero, the common contact (CC) closes the circuit with the normally closed (NC) cable. This makes that configuration the standard one. Hence, in our case, the NC situation is the one that will drive our backflow pump counterclockwise, generating flow from the Ao chamber to the LV chamber. When the digital output is 1, instead, the common contact will switch onto the normally open (NO) cable, which will revert the rotation direction and causing water flow from LV to Ao. As we said, this is an unconventional case. We have set this mechanism to start when the water level in the left ventricle goes either above 125mm or below 85mm. Those values were chosen under two considerations. First, because the chambers are 150mm high, thus, taking into account the encumbrance of the floating plates that are needed for the level sensors to work, the maximum water level that can be allowed to stop them from going against the rabbet is around 130 mm. The second main reason is that, according to the level sensors data sheet (Figure 3.31), they output different voltages for the same water level when it is lower than 85 mm. However, that does not happen if the level stays over 85 mm, which means we will not get any mismatch due to that.



Figure 3.30: Left ventricular chamber. The fluid must stay between 125-85 mm. The floating plate is needed to allow level detection by the sensor.

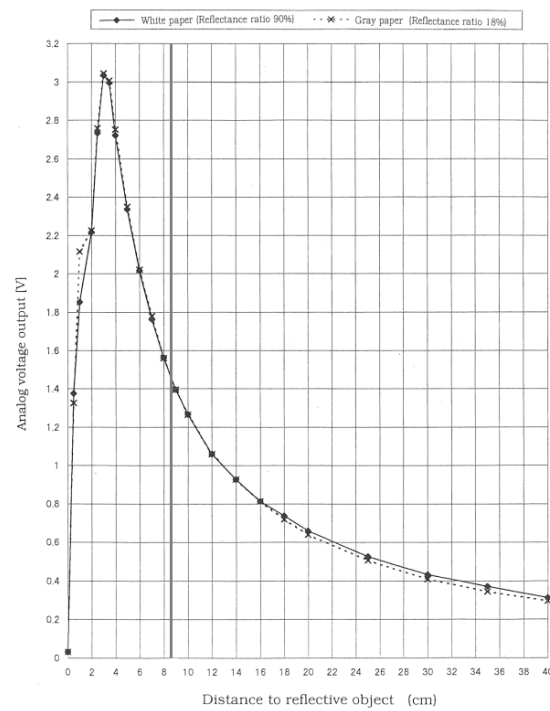


Figure 3.31: Level sensors voltage-height correlation.

Once the water level goes back in a range within 85 mm and 125 mm, then the common contact switches back to the normally closed mode and the simulator restarts to work ordinarily.

### 3.6. Test Protocol

The mock circulatory loop has been tested under several conditions. In particular, part of our tests were aimed at validating the numerical model and the experimental waveforms, and the other ones were peculiar to reckon the interaction within the numerical CVS and the inserted device. Our tests can be gathered with those following purposes:

- Tests for the numerical model validation.
- Tests for the experimental waveforms validation.
- Integration between VAD and simulator

At first, we want to assess the validity of the numerical model to see if it is able to replicate different patients' conditions varying pressure tracings consistently with the input parameters chosen by the user. Then we want to evaluate the ability of the system to respond in real-time to HR and CF changes made by the user simply using the sliders in the GUI during the simulation. The physiological values we set as initial conditions for CF and HR are respectively 1 and 60 bpm. Although every parameter in the model bears its relevance and can be varied, we choose to make the former parameter variation easier for the user because they are both paradigmatic for the evaluation of patients' clinical conditions. In particular, the contraction fraction value represents the ratio between the residual amount of ventricular contraction and the physiological one, as described more in detail in Section 3.1.1.

In order to assess the mock loop versatility, after the validation concerning CF and HR variations, we perform a test varying the inflow resistance of the aortic valve so to mimic a stenotic one. Just as an example of the great adaptability of the model, we want to see how pressures and flow rates adapt. When the valve is inserted in the test bench, the two tanks are put in communication, so the faucet between them is left open. A flow meter has to be placed either upstream or downstream the valve if an information concerning the actual flow rate is required. In that case, though, the code has to be modified and the flow meter signal has to be isolated from the inputs that enter the *Circulation* block in Simulink. The code may furtherly be edited by inserting the real valve parameters in the *Valve* block included in the *Circulation* model. For our tests, we changed the aortic valve resistance  $R_{dir}$  from the file *parameter\_cola.m*.

The last validation of the numerical part is done considering and assessing the correct functioning of the baroreflex mechanism to see how it influences the pressure tracings acting on heart rate, peripheral resistances and unstressed venous volume.

Once the numerical model has been completely validated, we move to the comparison between the expected simulated results and the experimental one.

The two main curves we computed to come up with all these considerations are pressure tracings over time and PV loops. Then the results has been evaluated considering three functional indexes:

- Left ventricular pressure error ( $err_{LV}$ ) or right ventricular pressure error ( $err_{RV}$ ) and aortic pressure error ( $err_{AO}$ ) or pulmonary artery pressure error ( $err_{PA}$ ): these indexes are calculated by averaging the error throughout the entire simulation, so the sum of the differences among the  $P(t)$  tracings simulated numerically and the experimental  $P(t)$  tracings is then divided by the number of the acquisitions. This calculation allows us to assess the likelihood between the two waveforms in every part of the cycle.

$$err = \frac{\sum |P(t)_{exp} - P(t)_{num}|}{\frac{t_{simulation}}{\Delta t}} \quad (3.16)$$

- Stroke work (SW): it is the area within the pressure-volume loop

$$SW = \oint P_{LV} dV \quad (3.17)$$

This value represents the external work done by the ventricle to eject blood into the aorta. We choose to use this index because it is representative of patient's ventricular functionality and its improvement. When dealing with the confront between the real and expected PV loops, we use the percent difference between the experimental and the simulated loop areas:

$$\Delta SW = \frac{|SW_{num} - SW_{exp}|}{SW_{num}} \cdot 100\% \quad (3.18)$$

Other parameters worth mentioning concerning the PV loops, that were qualitatively analysed, are:

- Potential Energy (PE), that is the one stored in the ventricle wall
- Total Mechanical Energy (PVA) that is:



$$PVA = SW + PE \quad (3.19)$$

In Figure 3.32 an overview concerning the meaning of those parameters is given.

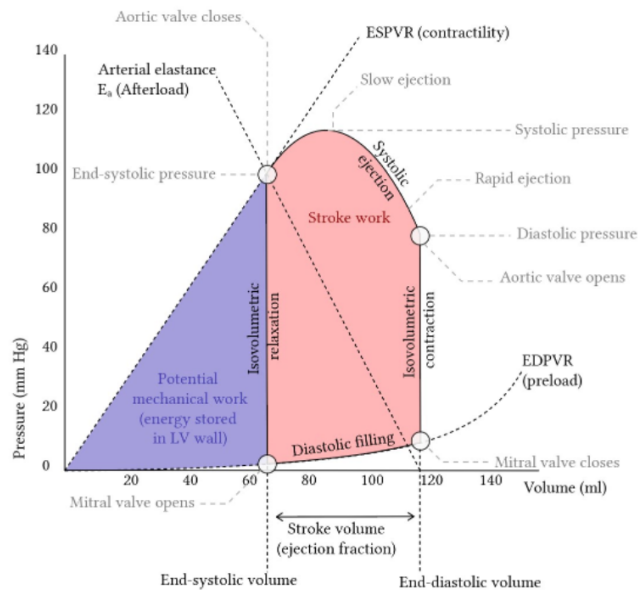


Figure 3.32: Overview on PV loop parameters: potential mechanical work, i.e. potential energy, in purple. Stroke work in red.

When coping with numerical simulations, all tests are done by running the *MainGui.m* in MATLAB by directly clicking on the desktop icon set up to ease the process. Then the cannulation configuration is chosen. Instructions to follow will continue to pop up by clicking the GUI's buttons from *Load System* to *Stop*:

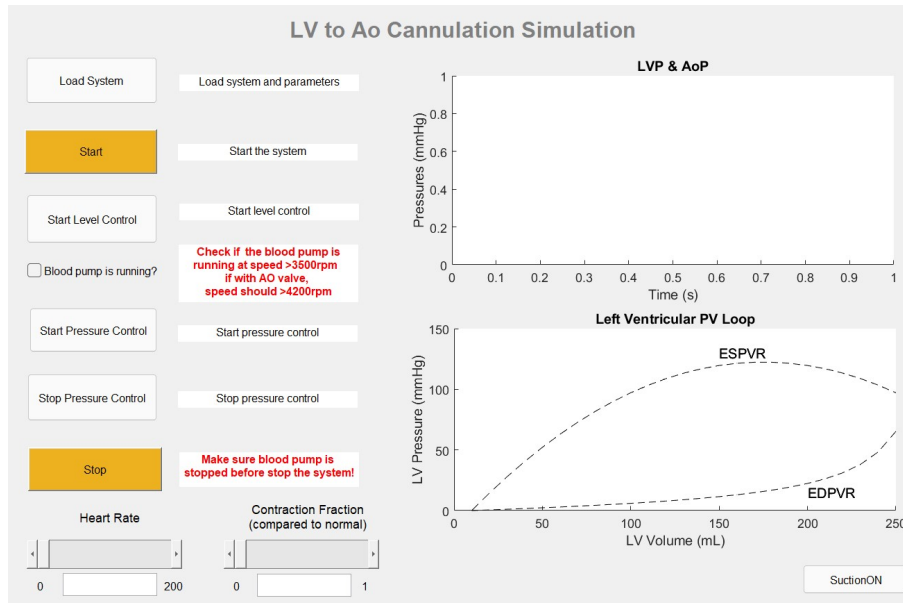


Figure 3.33: Graphic user interface if *Device testing* mode is chosen for the left cannulation.

Concerning the experimental validations, each component of the mock loop must be working: first of all the compressed air supply and the backflow pump are turned on, the air filter throttle valve is progressively rotated so to deliver compressed air at 0.4 MPa to the venturi vacuum pump, which achieves a vacuum pressure of around -80 KPa. The two manual valves on the top of the tanks and the faucet in between them are closed. In order not to have a rapid increase in the level of the LV tank the tubing connecting the two tanks is clamped. When the simulator is ready, the *MainGui.m* can be run.

When assessing the VAD performance instead, the assistance device must be connected to the tubing between the two chambers, the flow meter should be placed downstream the VAD (Figure 3.34). The effect of VAD assistance can be seen both in the pressure-time graph and in the pressure-volume one. The VAD must be turned after the *Start Level Control* button has been clicked, to prevent the aortic chamber from overfilling. When the *Stop Pressure Control* is clicked, one can turn the VAD off.

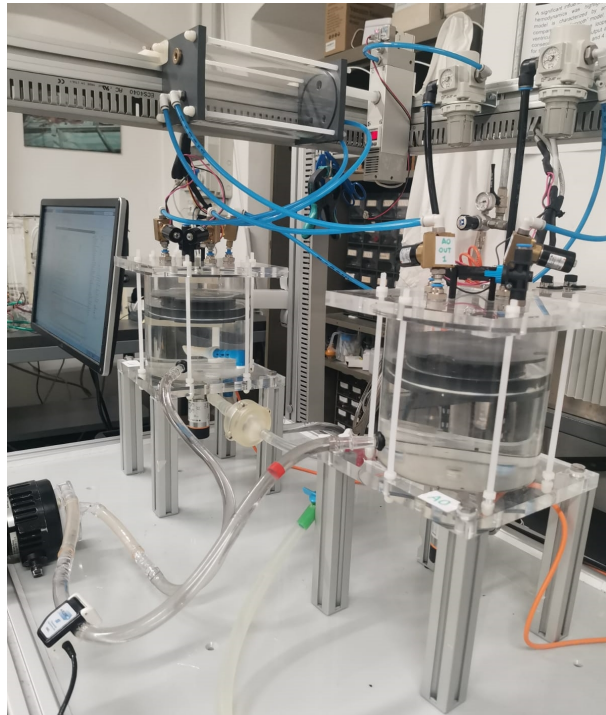


Figure 3.34: Connection of the centrifugal pump to the circuit. The flow probe is placed downstream the pump and the aortic valve is positioned in its holder in between the two chambers.



# 4 | Results

*This chapter seeks to validate the numerical model to see if volumes, pressures and flow rates change accordingly to model parameters variations. In Section 4.1.1 and 4.1.2 we assess the mock loop ability to adjust pressures when heart rate and contraction fraction are real-time changed. This evaluation is done in three conditions: (1) baroreflex control on peripheral resistances  $R_{Sa}, R_{Pa}$  and unstressed volume  $UVV$ , (2) baroreflex control on  $R_{Sa}$ ,  $UVV$  and  $HR$  and (3) no baroreflex control. The analysis concerning  $HR$  and  $CF$  variability is also performed by considering  $PV$  loops in Subsection 4.1.3. More considerations about the influence of the baroreflex control mechanism are made in the last part of the chapter. In Subsection 4.1.5 we deal with a few numerical considerations concerning the aortic valve resistance  $R_{dir}$ . An overview on the results that involve the experimental tracings is provided in Section 4.2. Section 4.3 refers to the analysis of the mock loop performance when coupled with a VAD.*

## 4.1. Numerical Model Assessment

The first section of our tests seeks to validate the numerical model the pressures rely on. It is crucial for the numerical model to replicate the physiological tracings, in order to proceed with the experiments on physical devices. Additionally, a strong feature of our model lies in its flexibility, because HR and CF may be changed in real time by the user. Even so, the computational tracings have to adjust within milliseconds. Theoretical pressure tracings and PV loops have been analysed precisely for this purposes. Along with it, the numerical model of the baroreflex needs to show that a readjustment of the pressure tracings occurs in pathological condition to try and restore a physiological situation.

The values we have taken as the physiological conditions of our tests are represented in the Table 4.1.

Table 4.1: Physiological Parameters.

<b>Heart Rate (HR)</b>	60 bpm
<b>Contraction Fraction (CF)</b>	1
<b>Max Left Ventricular Pressure</b>	130 mmHg
<b>Min Left Ventricular Pressure</b>	0 mmHg
<b>Max Aortic Pressure</b>	130 mmHg
<b>Min Aortic Pressure</b>	80 mmHg
<b>Max Right Ventricular Pressure</b>	27 mmHg
<b>Min Right Ventricular Pressure</b>	0 mmHg
<b>Max Pulmonary Artery Pressure</b>	27 mmHg
<b>Min Pulmonary Artery Pressure</b>	10 mmHg

### 4.1.1. HR Real-Time Variation

In these tests we compute the pressure tracings  $P(t)$  and we look at their behavior when changing the heart rate from GUI.

In Figure 4.1 the heart rate starts at 120 bpm, then it is switched by user to 80 bpm, and then again at 40 bpm. The contraction fraction parameter is kept constant at the physiological value of 1. The baroreflex control is implemented for the unstressed venous volume (UVV) and the systemic vascular resistance (SVR), represented by  $R_{Sa}$  so we see

that the ventricular pressure tracings readjust to physiological values after a few heart cycles. Aortic pressure ranges between 90 mmHg and 130 mmHg when the HR is at 120 bpm, its minimum decreases with the decrease of the heart rate, in particular the minimum value is 80 mmHg at 80 bpm and 60 mmHg at 40 bpm.

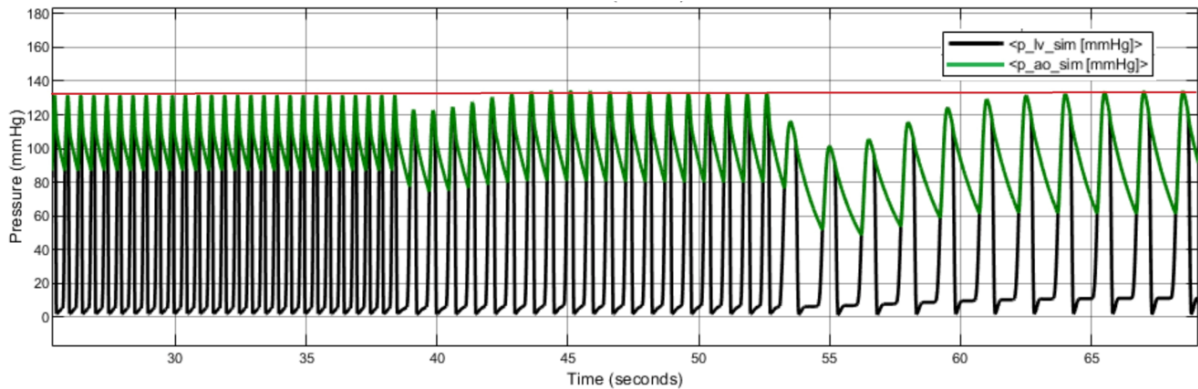


Figure 4.1: Numerical pressure tracings for LV (black line) and Ao (green line) varying the HR with UVV and SVR baroreflex control.

In Figure 4.2 the heart rate variations are again from 120 bpm to 80 bpm and then to 40 bpm, and the CF is still 1. In this case though, the baroreflex control is not active and accordingly to that, pressure peaks lower when HR decreases, no control is performed to try to rise to physiological values.

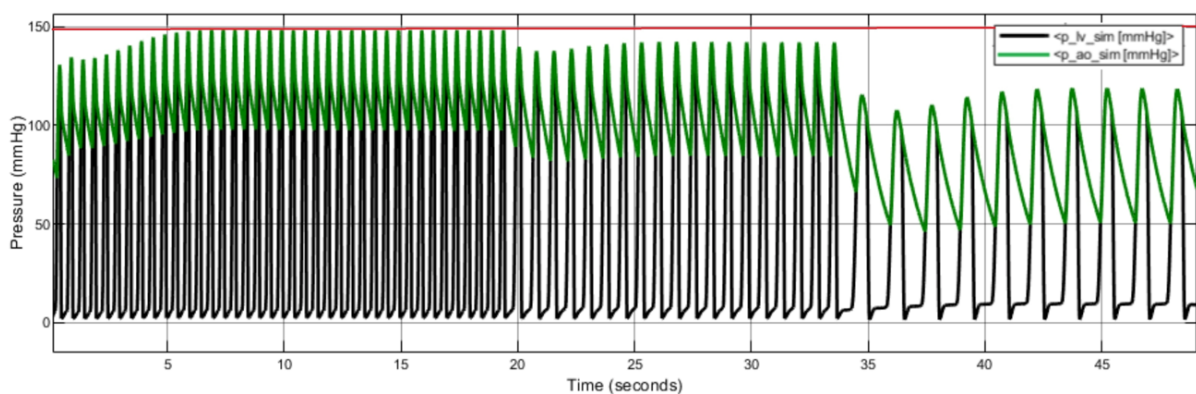


Figure 4.2: Numerical pressure tracings in time for LV (black line) and Ao (green line) varying the HR without baroreflex control.

The following tests in Figure 4.3, 4.4, 4.5 still intend to analyse  $P(t)$  for the LV and the Ao, but this time the baroreflex control is active not only for SVR and UVV, but also for

the heart rate (HR). The HR will vary as well to lean towards a physiological functioning of the heart. The HR baroreflex starts after 20 seconds. We set that limit because our model shows a highly unstable transient phase in the first seconds (Subsection 4.1.4), which would have altered the tracings. After 20 seconds, the HR plateaus to a constant value. In Figure 4.3 the simulation is started setting HR=40 bpm, the CF is fixed at 1. The baroreflex control activation,  $t=20$ s (red line), after an initial numerical oscillation, leads to an increase of the frequency to a more physiological condition.

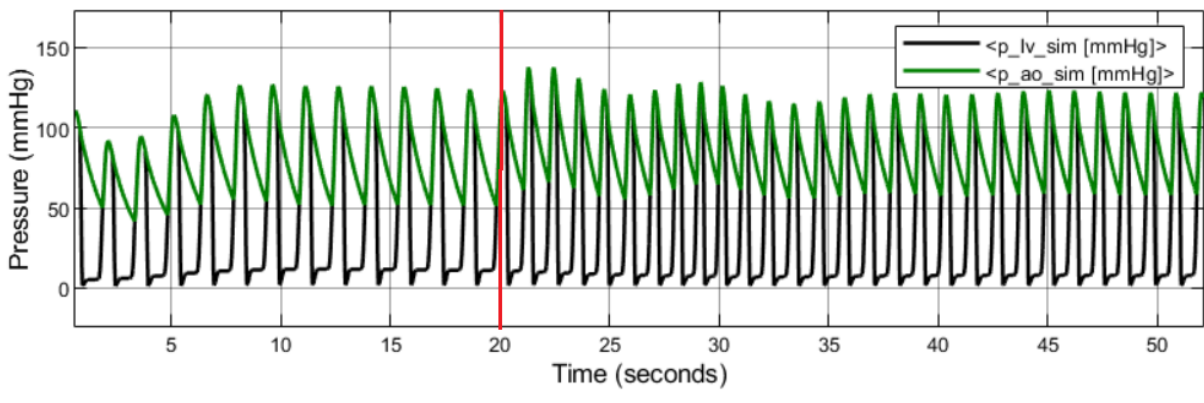


Figure 4.3: Numerical pressure tracings in time for LV (black line) and Ao (green line) with HR=40 bpm as initial condition and HR,UVV,SVR baroreflex control.

In Figure 4.4 the HR starts at 80 bpm, the CF is fixed at 1, and after the activation of the baroreflex control for the HR the frequency of cycles slightly decreases.

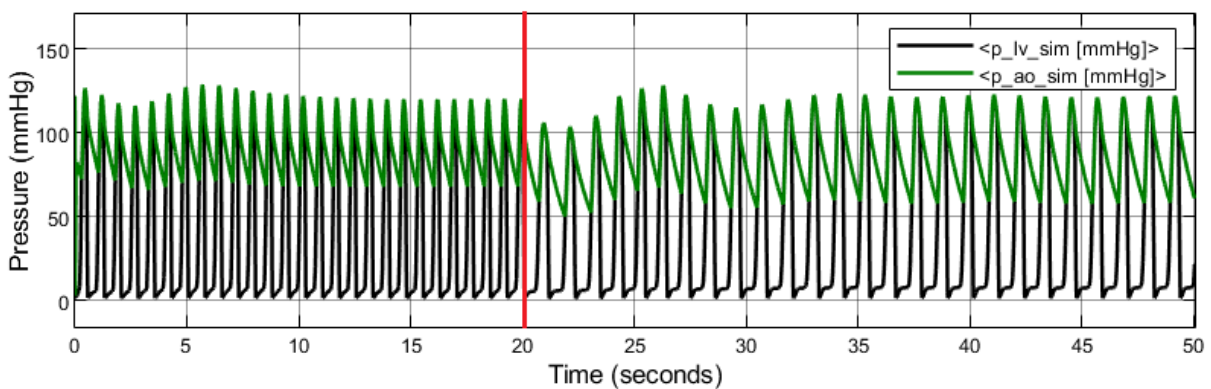


Figure 4.4: Numerical pressure tracings in time for LV (black line) and Ao (green line) with HR=80 bpm as initial condition and HR, UVV, SVR baroreflex control.

In Figure 4.5 the HR starts at 120 bpm, the CF is fixed at 1, and after the activation of the baroreflex control for the HR the frequency of cycles visibly decreases.



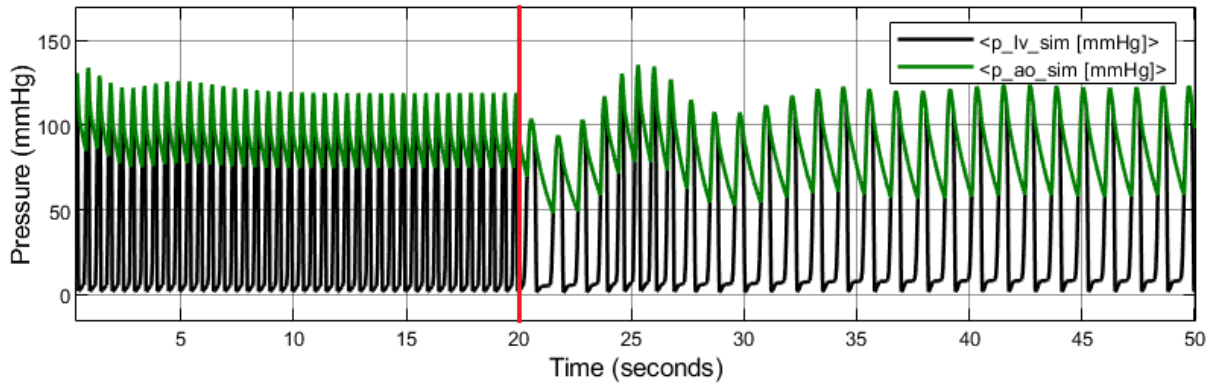


Figure 4.5: Numerical pressure tracings in time for LV (black line) and Ao (green line) with HR=120 bpm as initial condition and HR, UVV, SVR baroreflex control.

#### 4.1.2. CF Real-Time Variation

In these tests the variation of the contraction fraction is issued from GUI, and the pressure tracings adjust subsequently.

In Figure 4.6 the contraction fraction starts at CF=1, and then it gets switched by the user to 0.5 and then again to 0.2, while the HR parameter is kept constant at 60 bpm. The baroreflex control is implemented for the UVV and the SVR, because of that we see that pressure tracings readjust to physiological values after a few heart cycles when CF=0.5. However, when CF=0.2 the minimum of the ventricular pressure increases progressively, the maximum drops to 70 mmHg and then it remains almost constant.

In Figure 4.7 instead, the CF variations are again from 1 to 0.5 and then to 0.2, while HR is still at 60 bpm. Here, though, the baroreflex control is not applied, and what is shown is that the pressure tracings peaks always lower when CF decreases.

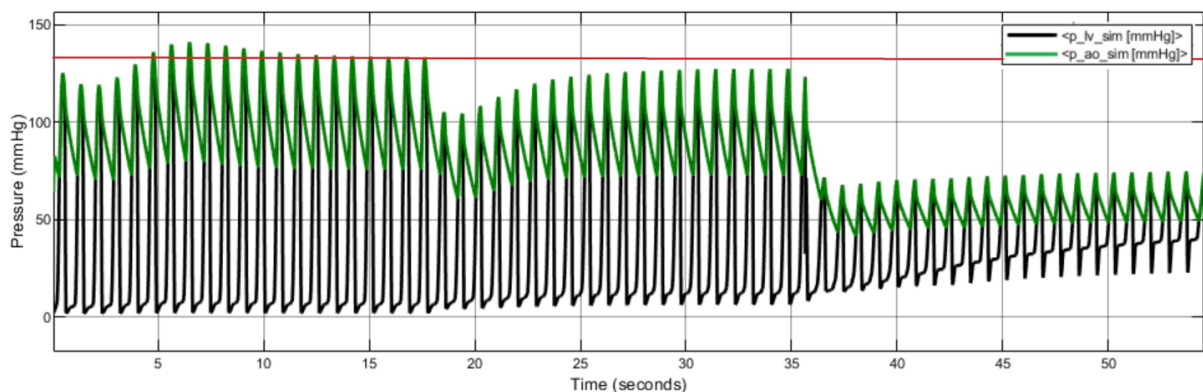


Figure 4.6: Numerical pressure tracings for LV (black line) and Ao (green line) varying the CF with UVV and SVR baroreflex control.

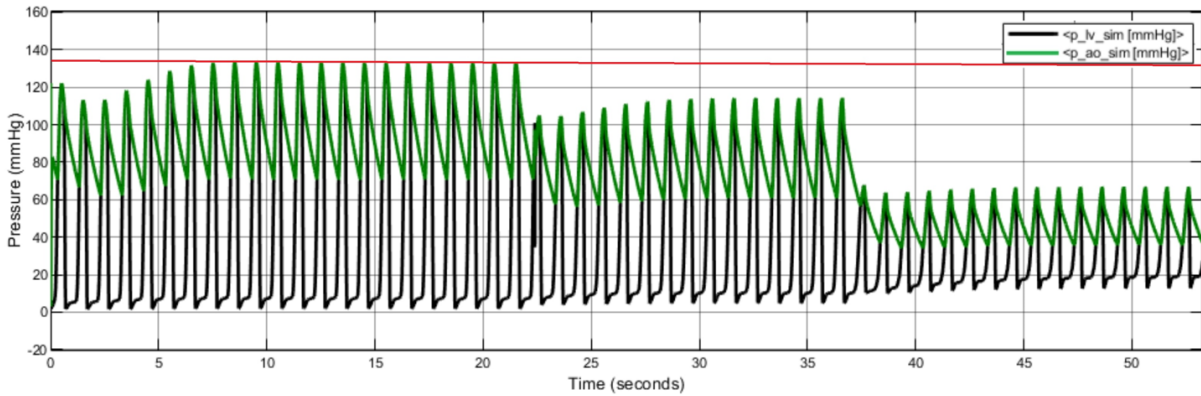


Figure 4.7: Numerical pressure tracings for LV (black line) and Ao (green line) varying the CF without UVV and SVR baroreflex control.

In Figure 4.8 the whole baroreflex control, including HR adjustment, is implemented. As before, the activation will occur after 20 seconds (red line). The CF starts at 1 here, with HR=60 bpm, i.e. the physiological scenario. After an initial transient phase, the theoretical pressure waveforms change very little in frequency or pressure peaks.

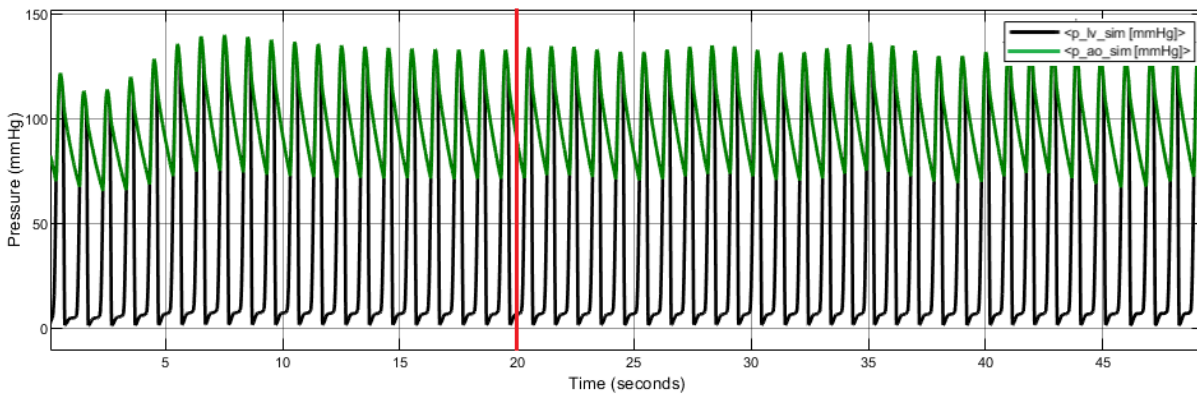


Figure 4.8: Numerical pressure tracings in time for LV (black line) and Ao (green line) with CF=1 and HR, UVV, SVR baroreflex control.

In Figure 4.9 instead the CF starts at 0.2 while HR is still 60 bpm, and, after 20 seconds, a visible increment in frequency is visible, while pressure peaks maintain low values.

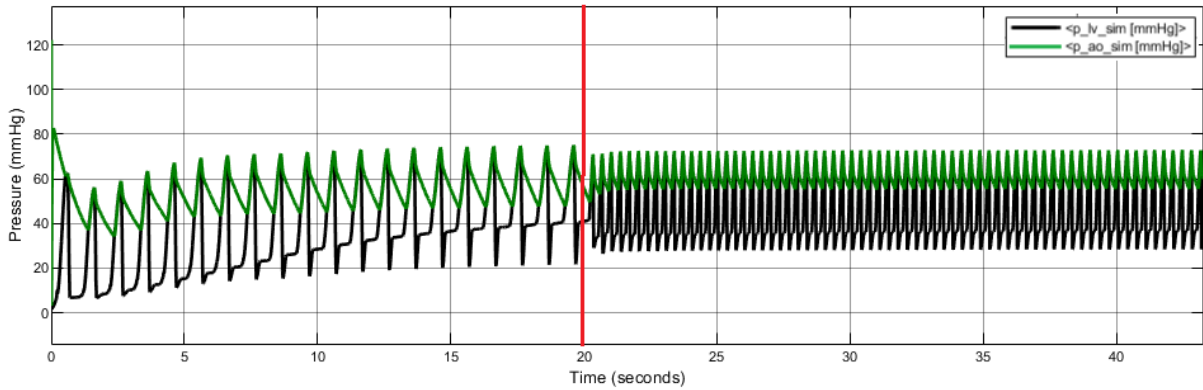


Figure 4.9: Numerical pressure tracings in time for LV (black line) and Ao (green line) with  $CF=0.2$  and HR, UVV, SVR baroreflex control.

### 4.1.3. PV Loops: Contraction Fraction and Heart Rate Variability

Once the pressure trends in time have been validated, the pressure-volume curves need to be considered. The aim is to see if the changes in stroke work (SW), end-diastolic volume (EDV), end-systolic volume (ESV), potential energy (PE) and pressure-volume area (PVA) are consistent with the set patient conditions.

In Figure 4.10 contraction fraction is fixed while heart rate is varied between 30 and 120 bpm so to see the response in reproducing PV loops from bradycardiac to tachycardiac patients. Because the contraction fraction is fixed to the value of 1, the ESPVR curve does not change. Moreover, as can be seen from Figure 4.10, ESV is fixed while EDV reduces with the increase of the heart rate. We can also notice that the potential energy of the heart and so the area between the ESPVR and the EDPVR curves on the left-hand side of the P-V loop is fixed, while the ventricular stroke work decreases:

- Figure 4.10 a. (HR=30 bpm, CF=1) has a  $SW= 9860 \text{ mL} \cdot \text{mmHg}$
- Figure 4.10 b. (HR=60 bpm, CF=1) has a  $SW= 7442 \text{ mL} \cdot \text{mmHg}$
- Figure 4.10 c. (HR=90 bpm, CF=1) has a  $SW= 6733 \text{ mL} \cdot \text{mmHg}$
- Figure 4.10 d. (HR=120 bpm, CF=1) has a  $SW= 4999 \text{ mL} \cdot \text{mmHg}$

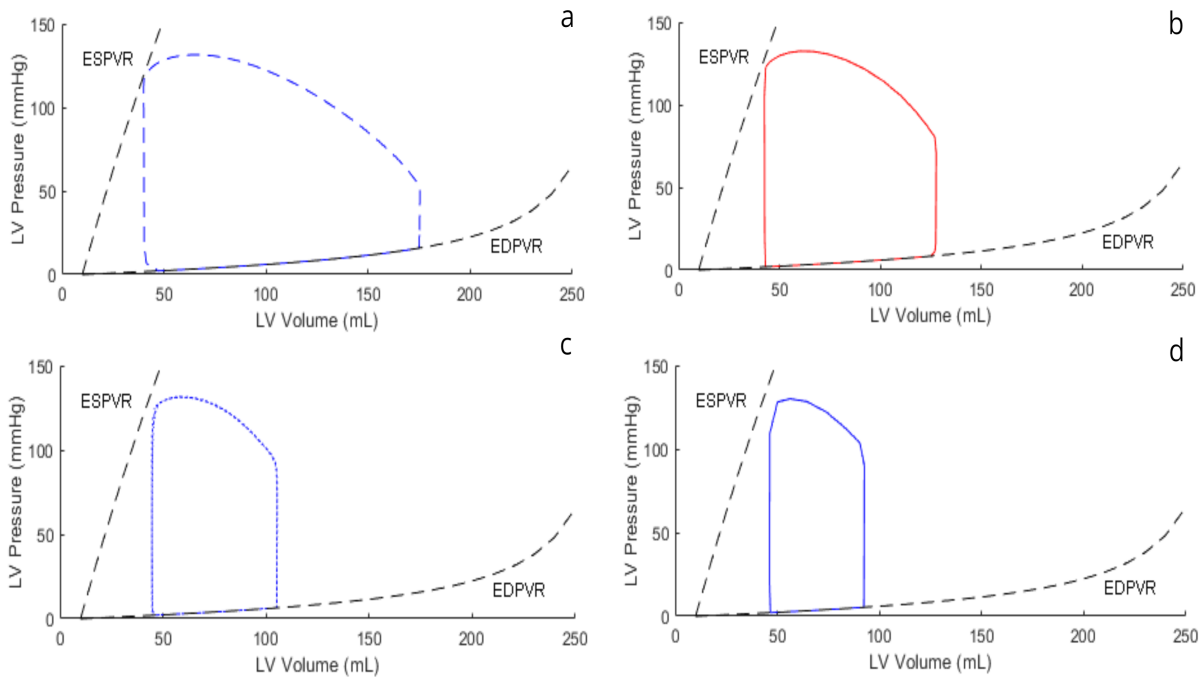


Figure 4.10: Simulated left ventricular P-V loops considering HR variability. HR=30 bpm (a), HR=60 bpm (b), HR=90 bpm (c), HR=120 bpm (d).

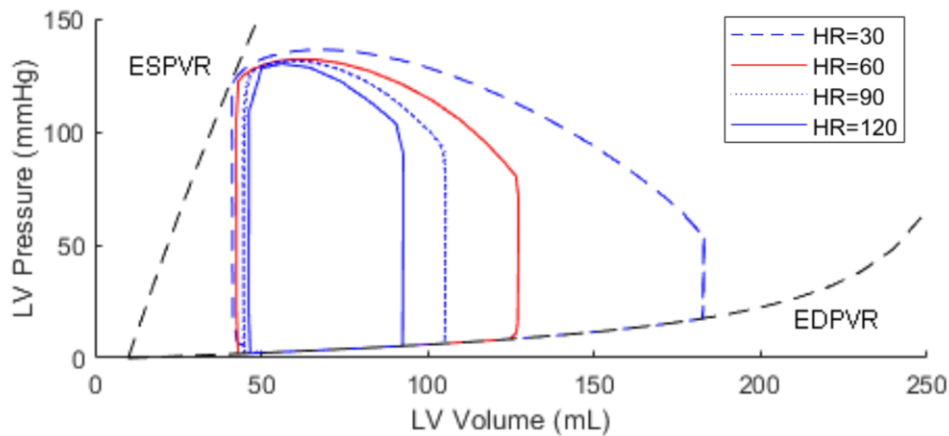


Figure 4.11: Simulated left ventricular P-V loops comparison varying HR. HR=30 bpm (dashed blue line), HR=60 bpm (solid red line), HR=90 bpm (dotted blue line), HR=120 bpm (solid blue line).

The next validation is done by changing the contraction fraction from 1 (healthy) to 0.4 (pathological) and maintaining HR constant at 60 bpm. The Frank-Starling curve slope diminishes and it shifts to the right. In this case SW decreases with the reduction of

contractility while PE, on the contrary, increases.

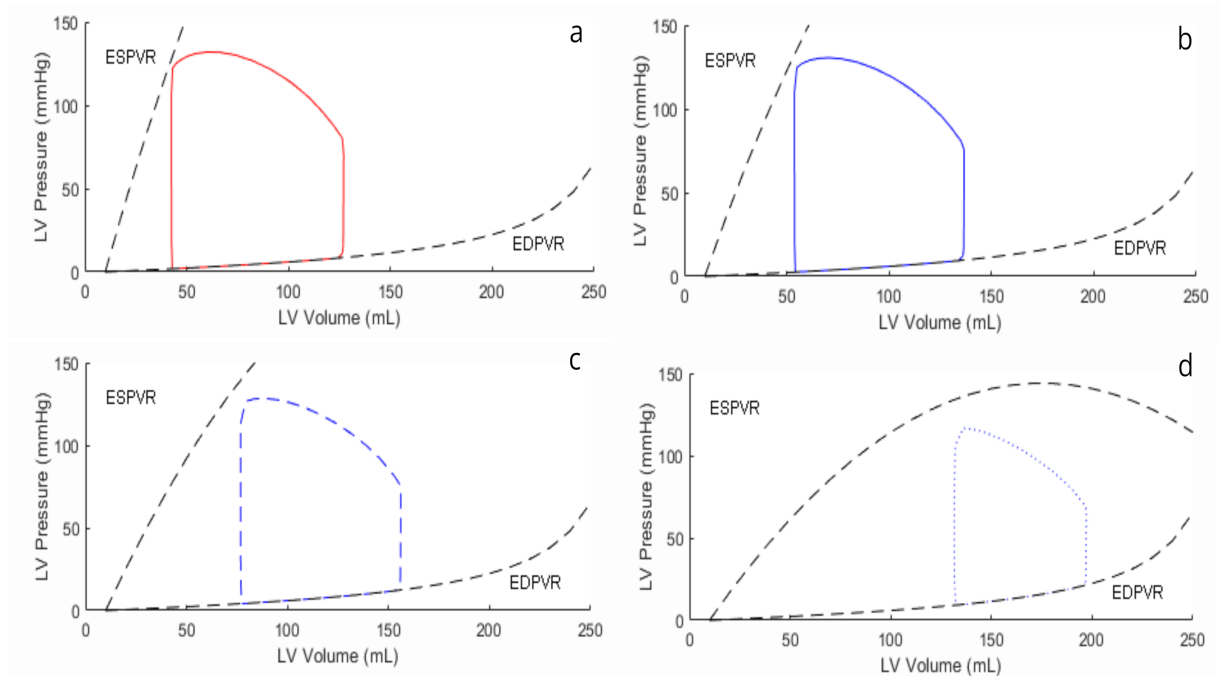


Figure 4.12: Simulated left ventricular P-V loops considering CF variability. CF=1 (a), CF=0.8 (b), CF=0.6 (c), CF=0.4 (d).

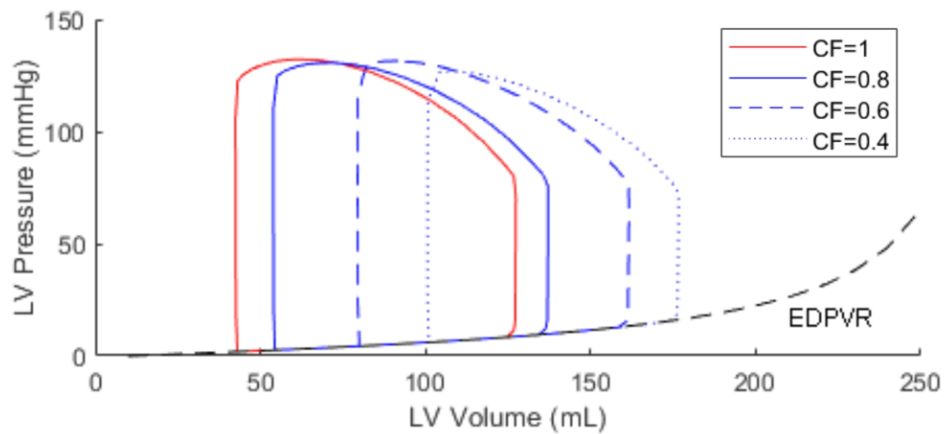


Figure 4.13: Simulated left ventricular P-V loops comparison varying CF.

#### 4.1.4. Baroreflex Configuration Evaluation

In this section the functionalities of our baroreflex model are analysed. Setting the physiological values concerning HR and CF, the aortic pressure ( $P_{Ao}$ ) ranges between 80-130

mmHg so the reference curve is the purple one (Figure 4.14). The Figures 4.14, 4.15, 4.16 below show the variations in heart rate and systemic arterial resistance (Rsa) changing the  $P_{Ao}$  from 50-80 mmHg to 90-140 mmHg. In particular, five simulations have been run feeding the baroreflex block at different pressure values.

In Figure 4.14 the HR variations are reported. The initial value for HR is set equal to 60 bpm. By increasing the pressure waveform values, HR decreases, while, when considering a very low pressure, ranging from 50 to 80 mmHg as minimum and maximum value respectively, HR rises. Having a transient behaviour that is highly unstable when the baroreflex mechanisms starts to act on the HR, we decided to delay its activation by 20 seconds, which is when the curves reach a plateaued value. In the mean time the fixed initial value set for the heart rate was the one we fed to our model.

The trend is almost the same for the systemic arterial resistance: a rise in Rsa occurs when AoP decreases, the resistance value drops instead when high pressure is considered. The initial value for Rsa is  $1.11 \text{ mmHg} \cdot \text{s/ml}$ .

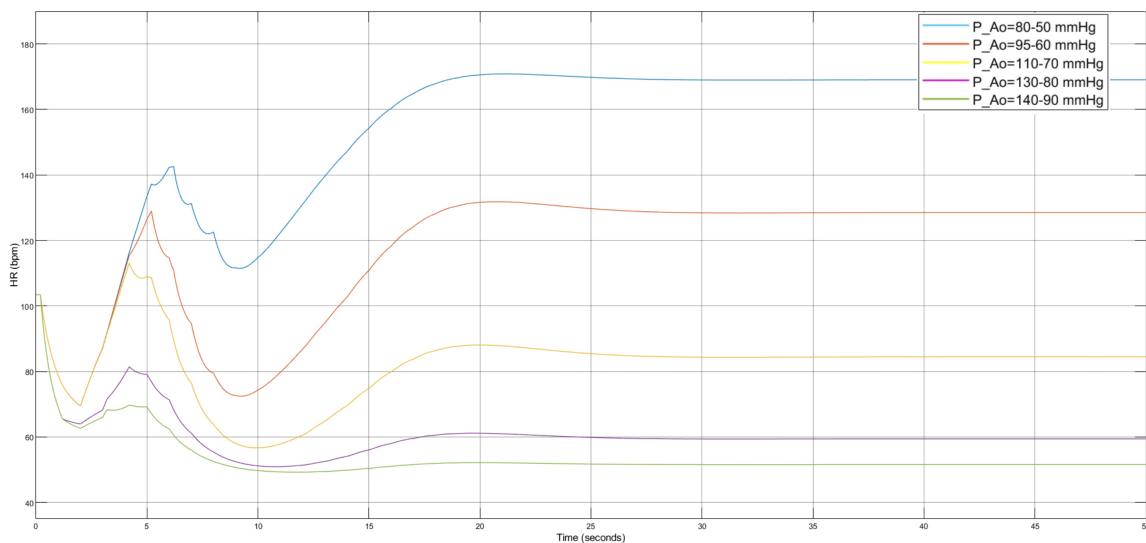


Figure 4.14: HR variability changing the input aortic pressure.

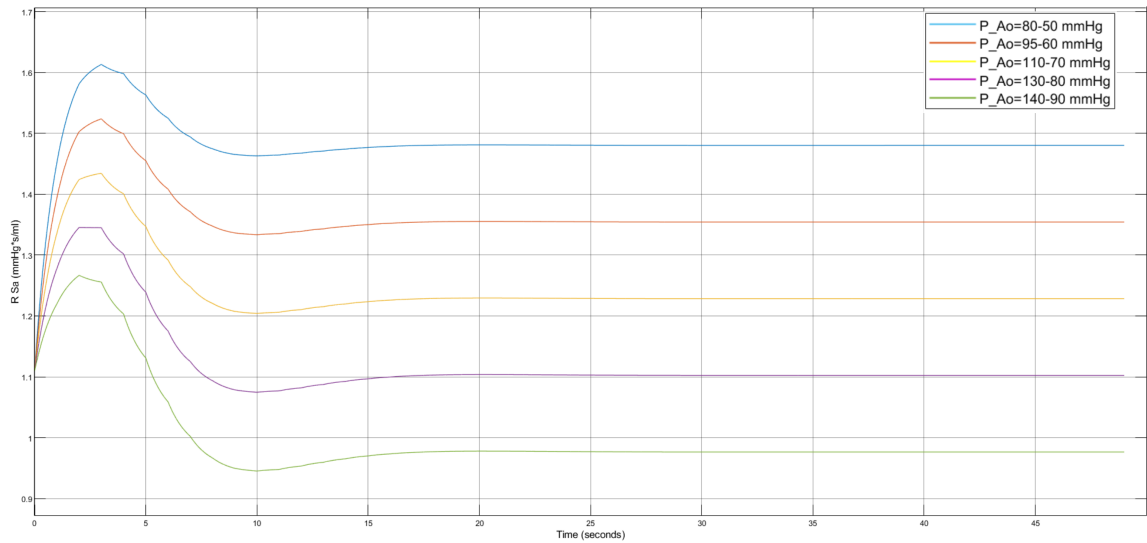


Figure 4.15: Systemic arterial resistance variability changing the input aortic pressure.

Concerning the unstressed venous volume (UVV) variations, we act on the cardiac output (CO) value instead of the aortic pressure. Five simulations have been done, the purple curve is the one considering a physiological cardiac output. With a smaller CO the UVV decreases too (Figure 4.16). It increases instead when considering higher cardiac output. In this case, the steady-state is achieved in 35-40 seconds, but since the variations are rather small, we allow that control from the very beginning.

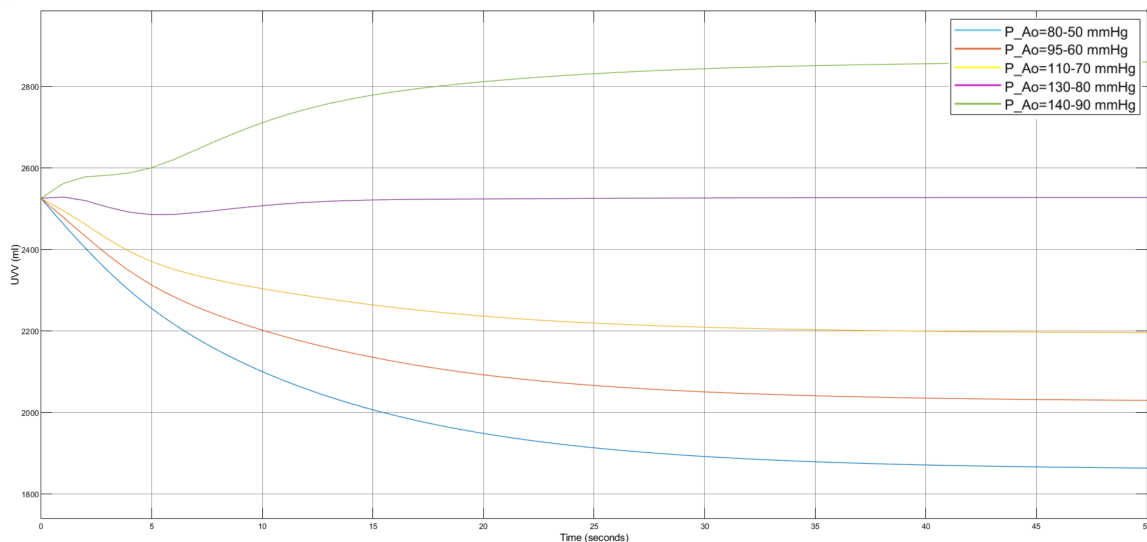


Figure 4.16: Unstressed venous volume variability changing the input cardiac output.

### 4.1.5. Aortic Valve Resistance Variation

One of the most important features of the mock loop is its flexibility. Loads of parameters can be changed directly in the numerical model to represent different clinical conditions. In this framework, just as an example of the great adaptability of the model, we vary the aortic resistance so as to mimic a stenotic heart valve and to see how pressures and flow rates adapt. Using constant HR and CF, we compare two different conditions: (1) Valve inflow resistance= $0.00375 \text{ mmHg} \cdot \text{s}/\text{ml}$ , (2) Valve inflow resistance= $0.08 \text{ mmHg} \cdot \text{s}/\text{ml}$ . In Figure 4.17 ventricular and aortic pressures in the two conditions are reported:  $p_{ao}$  does not change,  $p_{lv}$  increases when the valve resistance is higher.

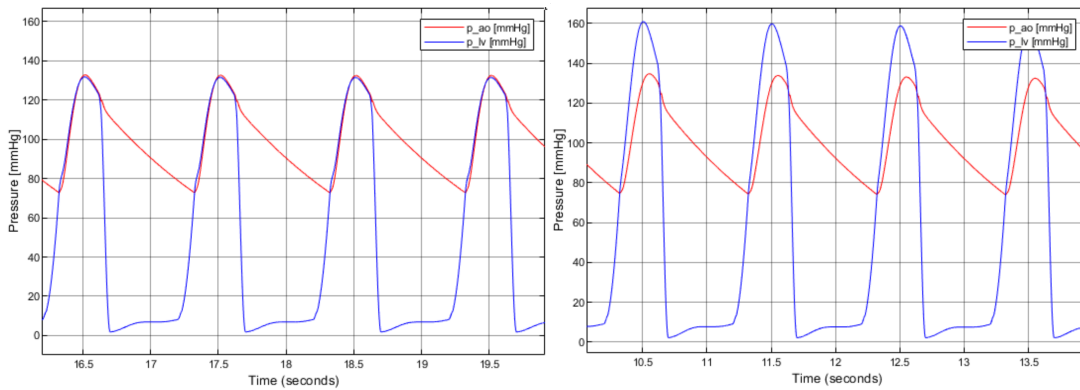


Figure 4.17: Left heart pressures at different aortic valve resistance: on the left  $R_{valve} = 0.00375 \text{ mmHg} \cdot \text{s}/\text{ml}$ , on the right  $R_{valve} = 0.08 \text{ mmHg} \cdot \text{s}/\text{ml}$ .

Increasing the valve resistance in the numerical model causes the numerical the flow rate through the simulated valve to decrease.

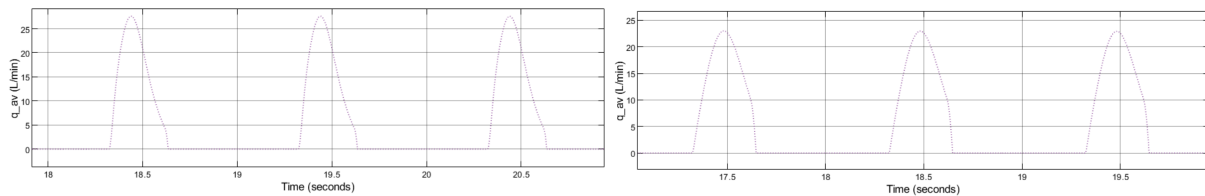


Figure 4.18: Numerical flow rate through the valve: on the left  $R_{valve} = 0.00375 \text{ mmHg} \cdot \text{s}/\text{ml}$ , on the right  $R_{valve} = 0.08 \text{ mmHg} \cdot \text{s}/\text{ml}$ .



## 4.2. Experimental Pressure Waveforms and PV Loops

Once the numerical model has been validated, the next step is to make a comparison between the experimental pressure tracings that actually occur in the two chambers and the ones from the numerical model. The pressure control is supposed to follow the numerical tracing, minimizing the average difference (which we are going to refer to as  $err_{LV}$  and  $err_{Ao}$ ) between the experimental tracings and the numerical ones, and to trigger the electrovalves' opening and closure consistently.

### 4.2.1. Left Ventricle Simulation

These tests aim is to assess the capability of the experimental  $P(t)$  to follow the numerical pressure tracings varying HR and the left ventricle CF real-time. The CF of the right ventricle will be fixed at 1 in all of our tests, in order to isolate the tests concerning only the LV. With regards to pressure accordingly to HR variations, at first, the heart rate is set to 120 bpm, then it is decreased to 80 bpm and then reduced again to 40 bpm. Concerning the contraction fraction variability analysis, HR is constant at 60 bpm while CF is diminished from 1 to 0.5 and then to 0.2. As in Section 4.1.1 and Section 4.1.2 we first make HR and CF vary with the baroreflex control acting on peripheral resistances and unstressed venous volume (Figure 4.19, 4.21), then we switch off this control and we look at the pressure tracings using constant values for  $R_{sa}$ ,  $R_{pa}$  and  $UVV$  (Figure 4.20, 4.22). In particular,  $R_{sa}=1.1$  mmHg·s/ml,  $R_{pa}=0.1$  mmHg· s/ml,  $UVV=2525$  ml. Numerical tracings and pressure trends have already been analyzed in Section 4.1, the important additional result is that also the experimental  $P(t)$  follows the simulated tracings when real-time changes are applied.

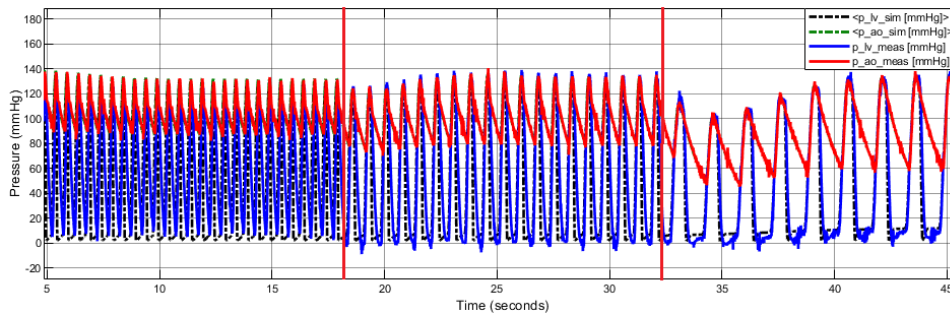


Figure 4.19: Numerical and experimental pressure tracings comparison for LV and Ao varying the HR with UVV and SVR baroreflex control. The solid red line represents the experimental  $P_{Ao}$ , the solid blue line the experimental  $P_{LV}$ , the dotted green line the numerical  $P_{Ao}$  and the dotted black line the numerical  $P_{LV}$ . Vertical red lines show when the HR is changed.

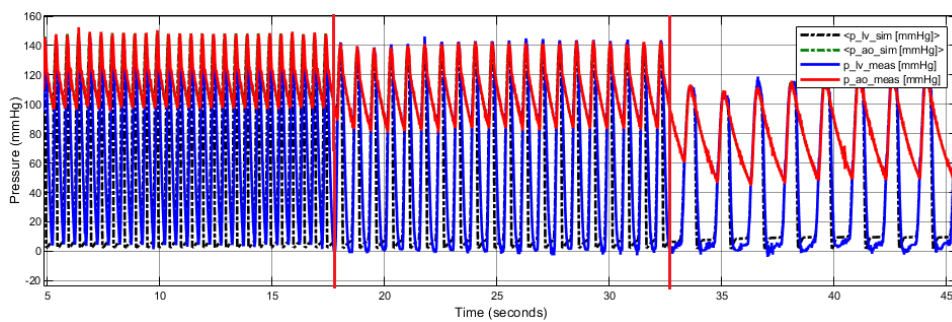


Figure 4.20: Numerical and experimental pressure tracings comparison for LV and Ao varying the HR without baroreflex control. The solid red line represents the experimental  $P_{Ao}$ , the solid blue line the experimental  $P_{LV}$ , the dotted green line the numerical  $P_{Ao}$  and the dotted black line the numerical  $P_{LV}$ . Vertical red lines show when the HR is changed.

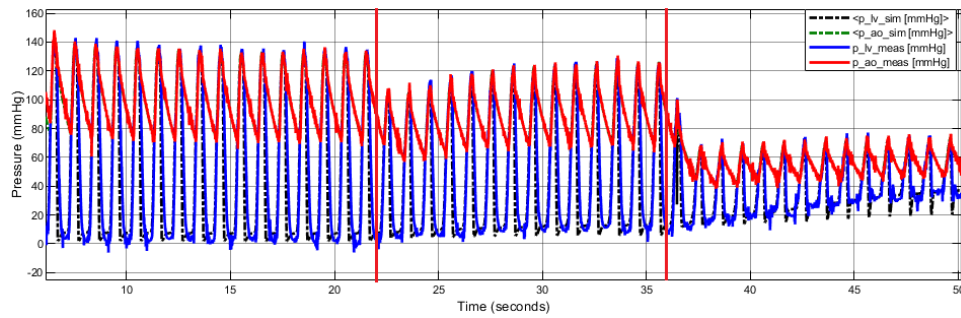


Figure 4.21: Numerical and experimental pressure tracings comparison for LV and Ao varying the CF with UVV and SVR baroreflex control. The solid red line represents the experimental  $P_{Ao}$ , the solid blue line the experimental  $P_{LV}$ , the dotted green line the numerical  $P_{Ao}$  and the dotted black line the numerical  $P_{LV}$ . Vertical red lines show when the CF is changed.

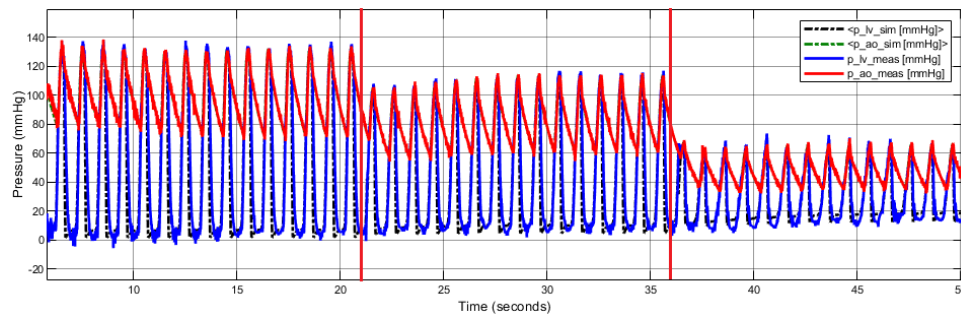


Figure 4.22: Numerical and experimental pressure tracings comparison for LV and Ao varying the CF without baroreflex control. The solid red line represents the experimental  $P_{Ao}$ , the solid blue line the experimental  $P_{LV}$ , the dotted green line the numerical  $P_{Ao}$  and the dotted black line the numerical  $P_{LV}$ . Vertical red lines show when the CF is changed.

In Figure 4.23 tracings concerning aortic and ventricular pressure are reported when choosing  $HR=30$  bpm. The numerical and experimental paths are well overlapped, except for few seconds after the isovolumic relaxation. The graph below in Figure 4.23 represents the instantaneous difference between the numerical and experimental tracings of LV and Ao. Using the Equation 3.16, the mean errors for the left ventricular and aortic pressure are respectively:  $err_{LV}=5.82$  mmHg,  $err_{AO}=1.20$  mmHg.

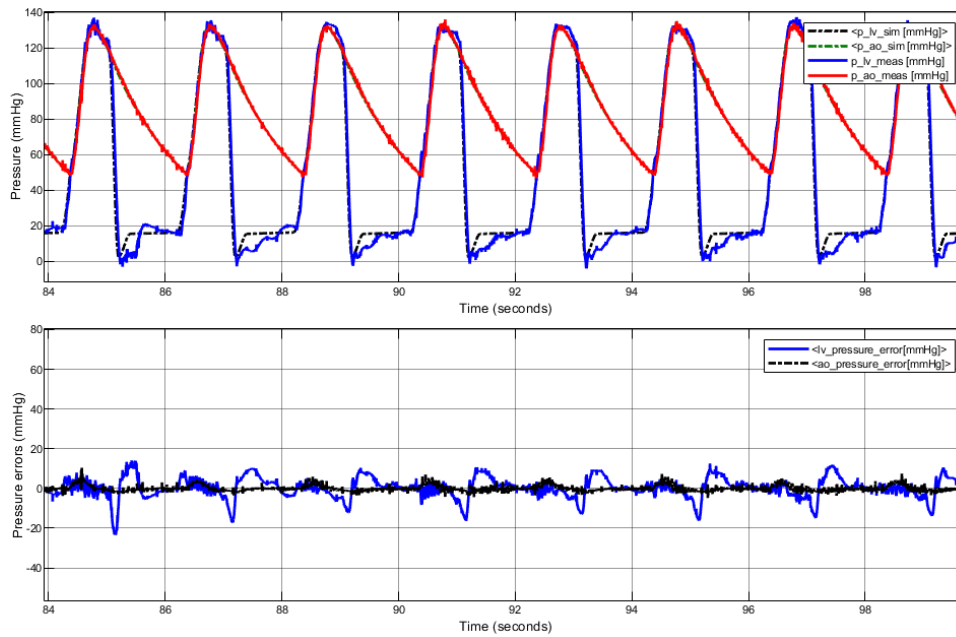


Figure 4.23: Left ventricle pressure waveforms and errors at HR=30 bpm and CF=1. The solid red line represents the experimental  $P_{Ao}$ , the solid blue line the experimental  $P_{LV}$ , the dotted green line the numerical  $P_{Ao}$  and the dotted black line the numerical  $P_{LV}$ .

Increasing the heart rate from 30 bpm to 60 bpm the aortic pressure minimum increases as noted also in Figure 4.1. Pressure tracings are superimposed except for the end of the isovolumic relaxation where the numerical curve slope is higher than the experimental one. Mean errors are:  $err_{LV}=10.82$  mmHg,  $err_{AO}=1.46$  mmHg.

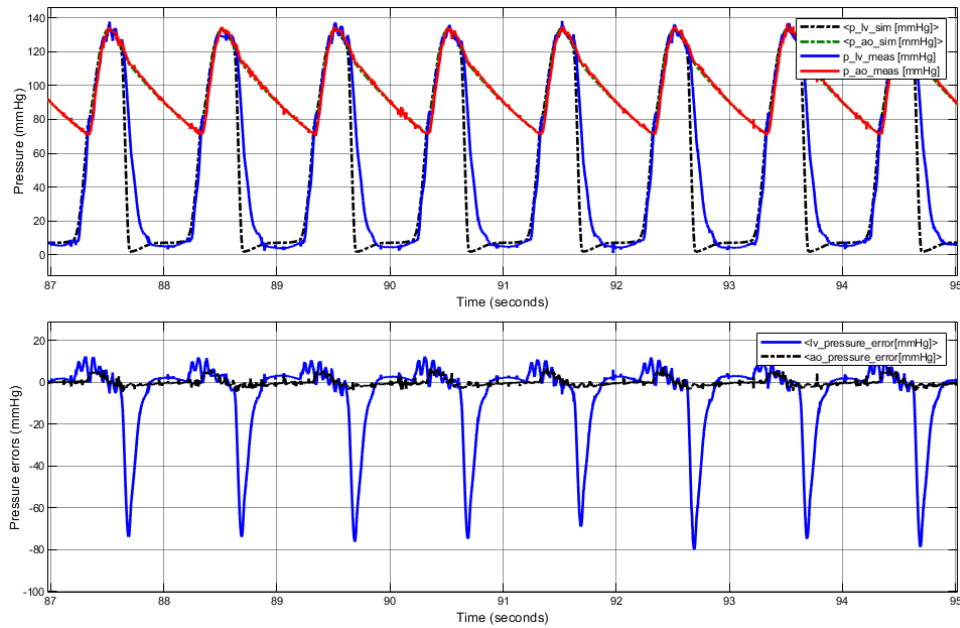


Figure 4.24: Left ventricle pressure waveforms and errors at HR=60 bpm and CF=1. The solid red line represents the experimental  $P_{Ao}$ , the solid blue line the experimental  $P_{LV}$ , the dotted green line the numerical  $P_{Ao}$  and the dotted black line the numerical  $P_{LV}$ .

In Figure 4.25 the HR is set to 90 bpm, the ventricular pressure descending phase, the one concerning the isovolumic relaxation, is hard to follow for the controller. The results are good instead for the aortic pressure in general and both for the isovolumic contraction and the ejection of the left ventricle. Mean errors increases, especially for the left ventricle:  $err_{LV}=17.04$  mmHg,  $err_{AO}=1.47$  mmHg.

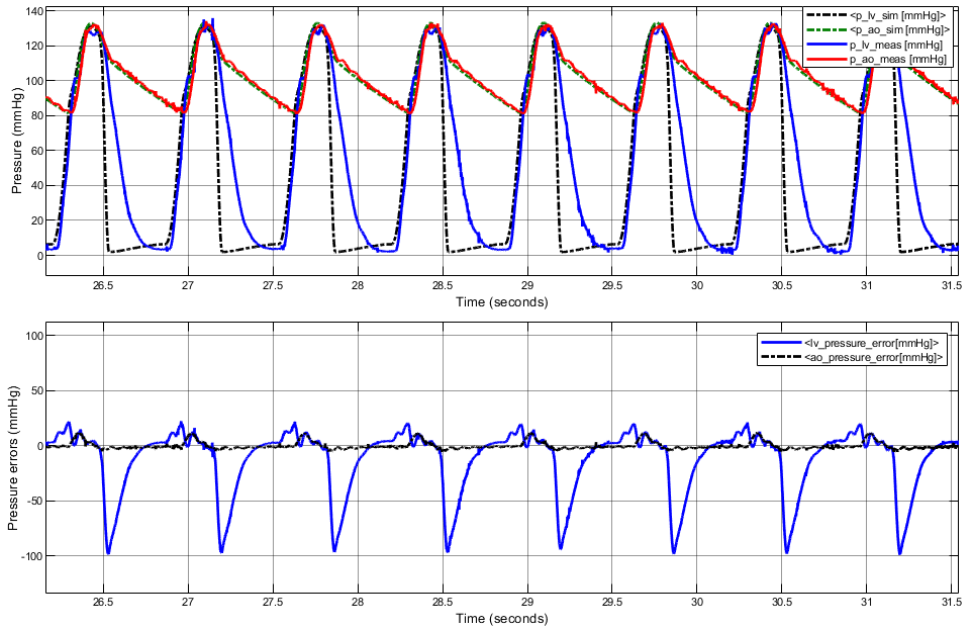


Figure 4.25: Left ventricle pressure waveforms and errors at HR=90 bpm and CF=1. The solid red line represents the experimental  $P_{Ao}$ , the solid blue line the experimental  $P_{LV}$ , the dotted green line the numerical  $P_{Ao}$  and the dotted black line the numerical  $P_{LV}$ .

The last test concerning HR variability is done by setting the hart rate to 120 bpm. In this case we can see that, concerning ventricular pressure, there is a small delay in the ascending phase while the delay became higher during the descending one. The peak value (130 mmHg) of the ejection phase is easily reached. Concerning aortic pressure, differently from the tests at other frequencies, a small delay is present. Mean errors increase:  $err_{LV}=19.7$  mmHg,  $err_{AO}=2.54$  mmHg.

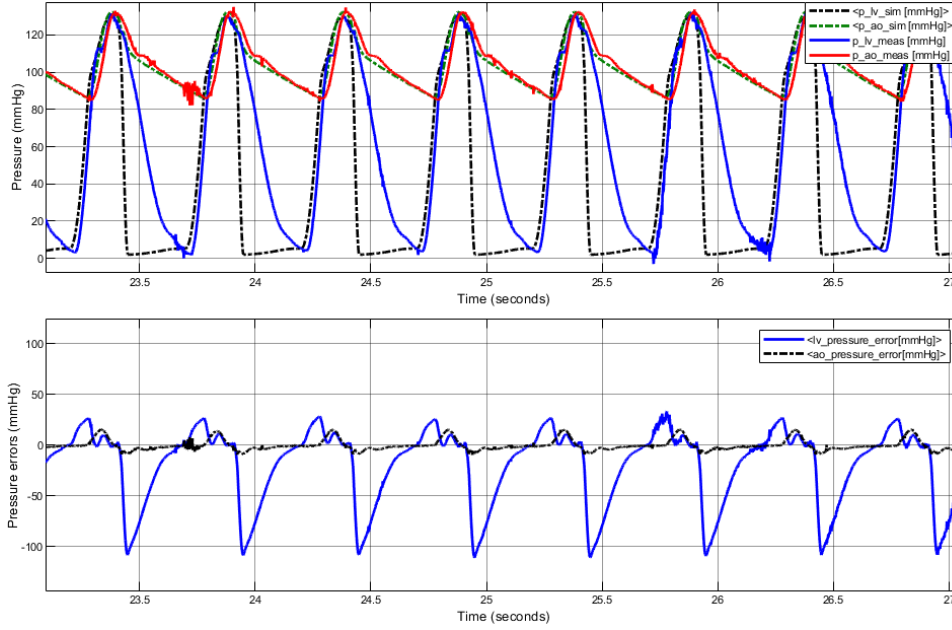


Figure 4.26: Left ventricle pressure waveforms and errors at HR=120 bpm and CF=1. The solid red line represents the experimental  $P_{Ao}$ , the solid blue line the experimental  $P_{LV}$ , the dotted green line the numerical  $P_{Ao}$  and the dotted black line the numerical  $P_{LV}$ .

Being the pressure-volume loop of significant relevance, the ultimate proof on how performing our model is derived by this analysis. The left and right ventricular contraction fractions are set to 1 while the HR is varied. In particular the HR values are the same used from Figure 4.28 to Figure 4.31, so to have a complete overview of pressures tracings and pressure-volume loops for that HR values. The stroke work (SW) parameter was taken into account. The discrepancy between the two loops will be assessed therefore analysing the  $\Delta SW$ .

$$\Delta SW = \frac{|SW_{num} - SW_{exp}|}{SW_{num}} \cdot 100\% \quad (4.1)$$

It goes without saying that, the closer to zero, the more similar the two PV loops are.

In Figure 4.27 numerical and experimental PV loops are plotted with four different parameter settings:

- Figure 4.27 a shows the theoretical and experimental PV loops at HR=30 bpm CF=1  $\Delta SW=3.87\%$
- Figure 4.27 b shows the theoretical and experimental PV loops at HR=60 bpm CF=1  $\Delta SW=14.90\%$

- Figure 4.27 c shows the theoretical and experimental PV loops at HR=90 bpm CF=1  $\Delta SW=25.91\%$
- Figure 4.27 d shows the theoretical and experimental PV loops at HR=120 bpm CF=1  $\Delta SW=19.57\%$

The HR=30 bpm condition leads to an almost perfect superimposition of the two curves, increasing the heart rate the ejection phase and the isovolumic contraction are well reproduced while for the experimental curves is hard to follow the isovolumic relaxation and the filling phase.

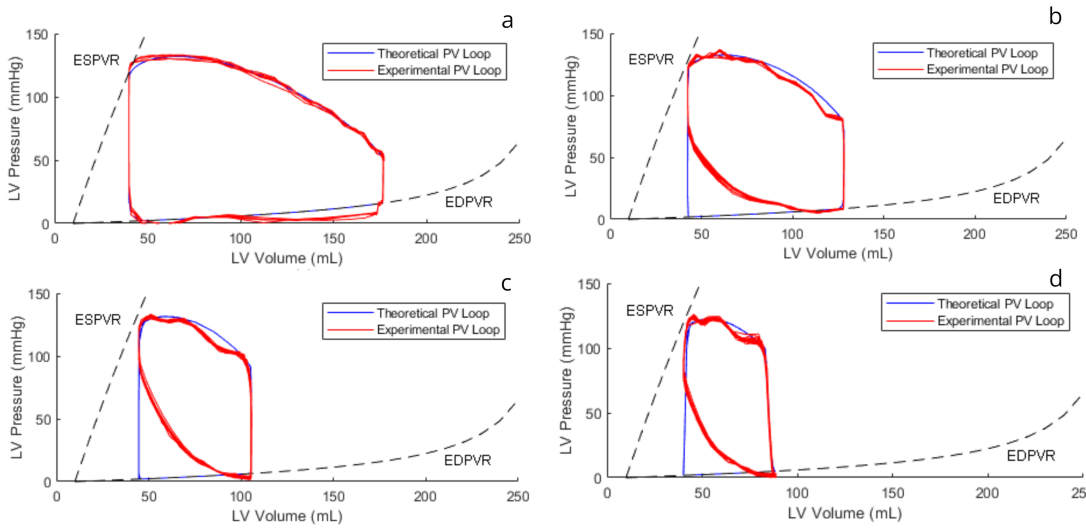


Figure 4.27: Theoretical and experimental left ventricular PV loops considering HR variability. HR=30 bpm (a), HR=60 bpm (b), HR=90 bpm (c), HR=120 bpm (d).

#### 4.2.2. Right Ventricle Simulation

As the LV analysis, firstly we took into account the variations in HR keeping the contraction fraction of both left and right ventricle fixed to 1. We plotted the pressure tracings of the right ventricle, both experimental and numerical, and the average errors between the numerical and the correspondent experimental one.

In Figure 4.28 the  $P(t)$  waveforms were computed at HR=30 bpm. Some oscillations are shown in the third and fifth cycle, but overall the experimental curves seem to superpose to the numerical ones. The graph below in Figure 4.28 represents the instantaneous difference between the numerical and experimental tracings of RV and Pa, which we will refer to as "error". Here  $err_{Pa}=0.91$  mmHg, while  $err_{RV}=1.68$  mmHg. The waveforms peak values between 30 to 35 mmHg, which is coherent with the physiology of the right



ventricle.

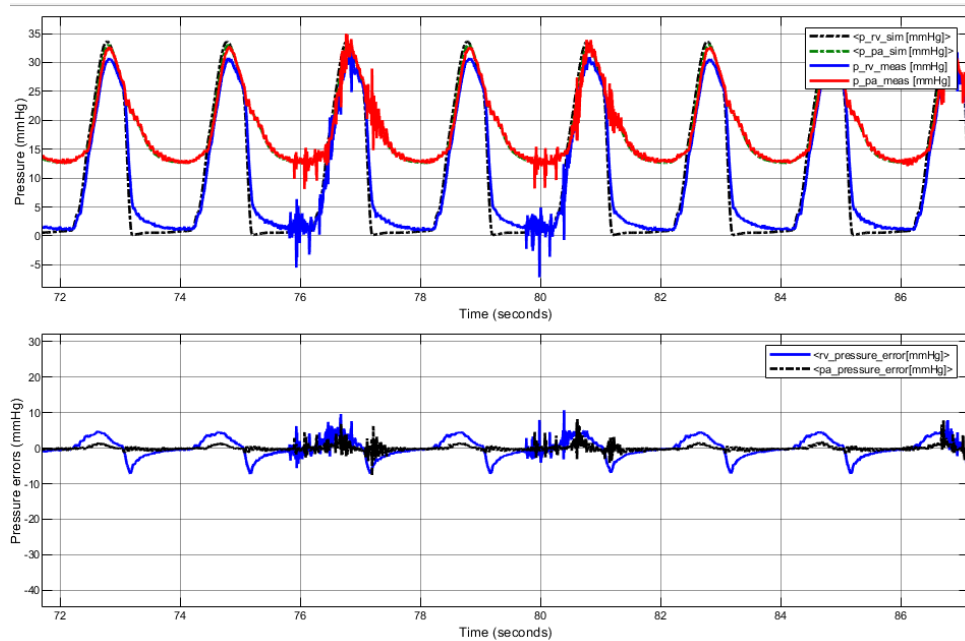


Figure 4.28: Right cannulation pressure waveforms and errors at  $HR=30$  bpm and  $CF_{RV} = CF_{LV} = 1$ . The solid red line represents the experimental  $P_{Pa}$ , the solid blue line the experimental  $P_{RV}$ , the dotted green line the numerical  $P_{Pa}$  and the dotted black line the numerical  $P_{RV}$ .

In Figure 4.29 the  $P(t)$  waveforms were computed at  $HR=60$  bpm. Less oscillations, compared to the previous case, are present. However, the RV pressure tracing does not touch peak at the same value as the Pa pressure tracing. Moreover, a delay in the isovolumic relaxation of the systolic ejection is noticeable. In spite of that, the experimental pressure  $P(t)$  follows rather smoothly, with a small difference, the numerical tracings in the isovolumic contraction, in the diastolic phase of the RV, and in the Pa tracing. In fact, the average errors are  $err_{Pa}=0.98$  mmHg, while  $err_{RV}=2.78$  mmHg. In Figure 4.30 the  $P(t)$  waveforms were computed at  $HR=90$  bpm. A few oscillations are shown in the pulmonary artery pressure tracing. The peak of the RV tracing does not reach the same as the Pa one. Compared to the previous case, here a slight delay is noticeable in the isovolumic contraction as well, and the delay in the isovolumic relaxation phase increases. In correspondence of that delay, the average error tracing shows peaks that reach  $-15$  mmHg. Overall, the average errors are  $err_{Pa}=1.18$  mmHg, while  $err_{RV}=3.42$  mmHg.

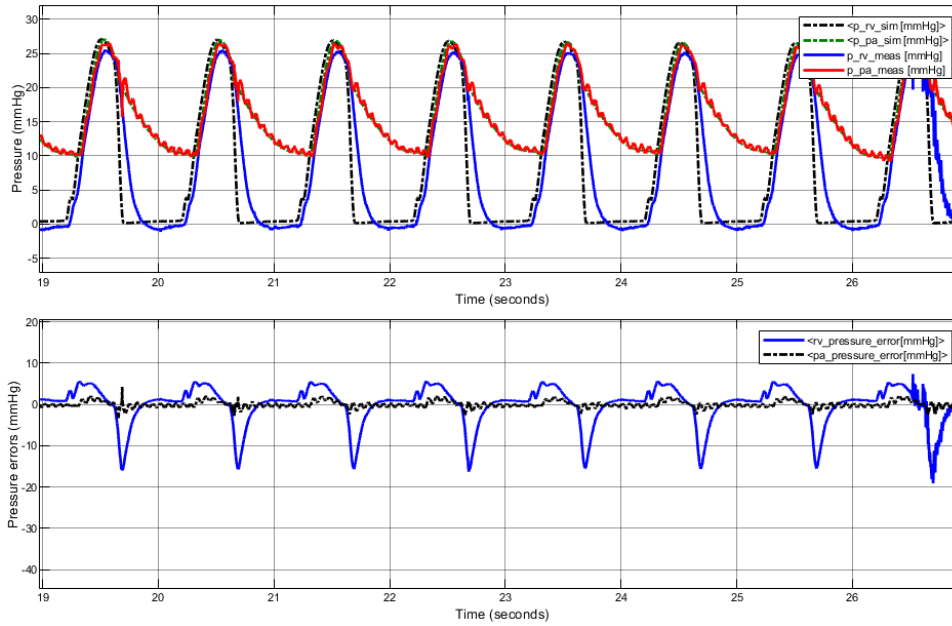


Figure 4.29: Right ventricle pressure waveforms and errors at  $HR=60$  bpm and  $CF_{RV} = CF_{LV} = 1$ . The solid red line represents the experimental  $P_{Pa}$ , the solid blue line the experimental  $P_{RV}$ , the dotted green line the numerical  $P_{Pa}$  and the dotted black line the numerical  $P_{RV}$ .

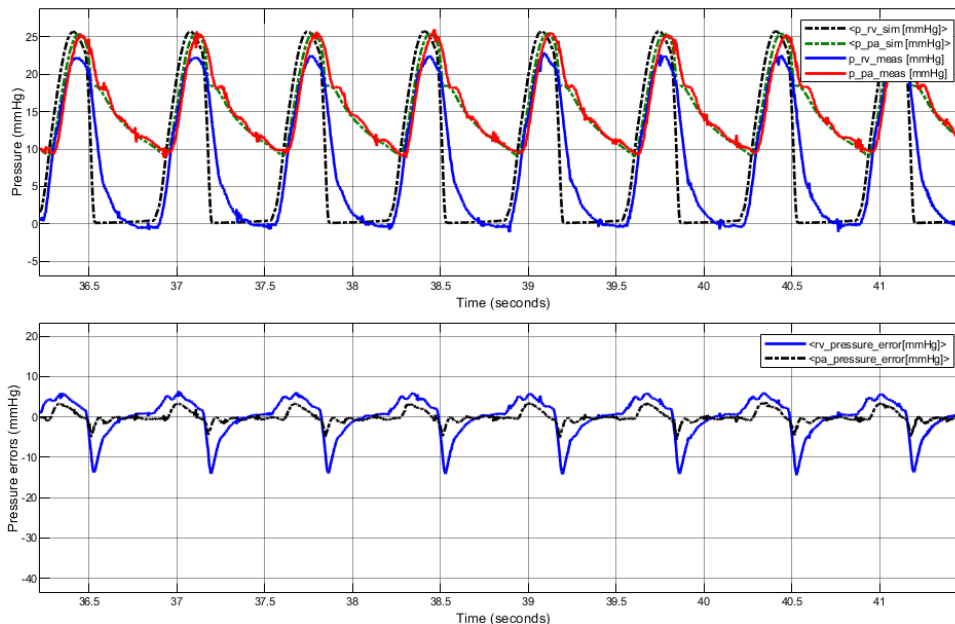


Figure 4.30: Right ventricle pressure waveforms and errors at  $HR=90$  bpm and  $CF_{RV} = CF_{LV} = 1$ . The solid red line represents the experimental  $P_{Pa}$ , the solid blue line the experimental  $P_{RV}$ , the dotted green line the numerical  $P_{Pa}$  and the dotted black line the numerical  $P_{RV}$ .

In Figure 4.31 the  $P(t)$  waveforms were computed at  $HR=120$  bpm. Oscillations are much more evident in the  $P(t)$  tracing of the  $P_a$ . The pressure peak of the  $R_V$  tracing is lower with respect to the numerical expectation. At this frequency, the experimental tracings are shifted in time, which causes the average error to increase to values of  $err_{P_a}=1.39$  mmHg, while  $err_{R_V}=5.02$  mmHg.

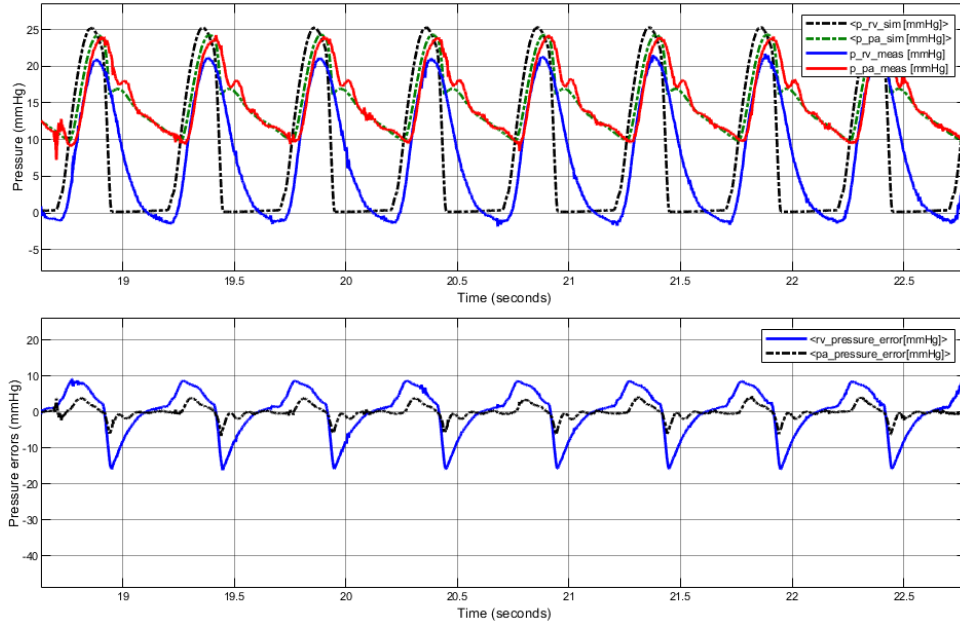


Figure 4.31: Right ventricle pressure waveforms and errors at  $HR=120$  bpm and  $CF_{RV} = CF_{LV} = 1$ . The solid red line represents the experimental  $P_{P_a}$ , the solid blue line the experimental  $P_{R_V}$ , the dotted green line the numerical  $P_{P_a}$  and the dotted black line the numerical  $P_{R_V}$ .

Forthcoming acquisitions aim to analyse once again the pressure tracings and the average errors, but from a different point of view. In this case, the  $HR$  will be kept at a fixed value of 60 bpm, and the  $CF_{RV}$  parameter will be changed.  $CF_{LV}$  will instead be kept to 1 in all the simulations, in order to clearly appreciate the influence of the  $CF_{RV}$  on the waveforms and, later in the results, on the PV loops.

We have already analysed the case where  $HR=60$  bpm and  $CF_{RV}=1$  in Figure 4.29. This will be our reference physiological tracing also under these test conditions.

In Figure 4.32 the  $P(t)$  waveforms were computed at  $HR=60$  bpm and  $CF_{RV} = 0.8$ . Oscillations are present in the  $P_{P_a}$  tracing. Here the peak of  $P_{R_V}$ , which is about 25 mmHg, can almost reach the numerical value, which is about 27 mmHg. The delay in the descending

part of the systolic ejection is bigger than when  $CF_{RV} = 1$ . However, since the tracings overlap for most of the time, the average errors are  $err_{P_a} = 0.8$  mmHg, while  $err_{RV} = 3.07$  mmHg.

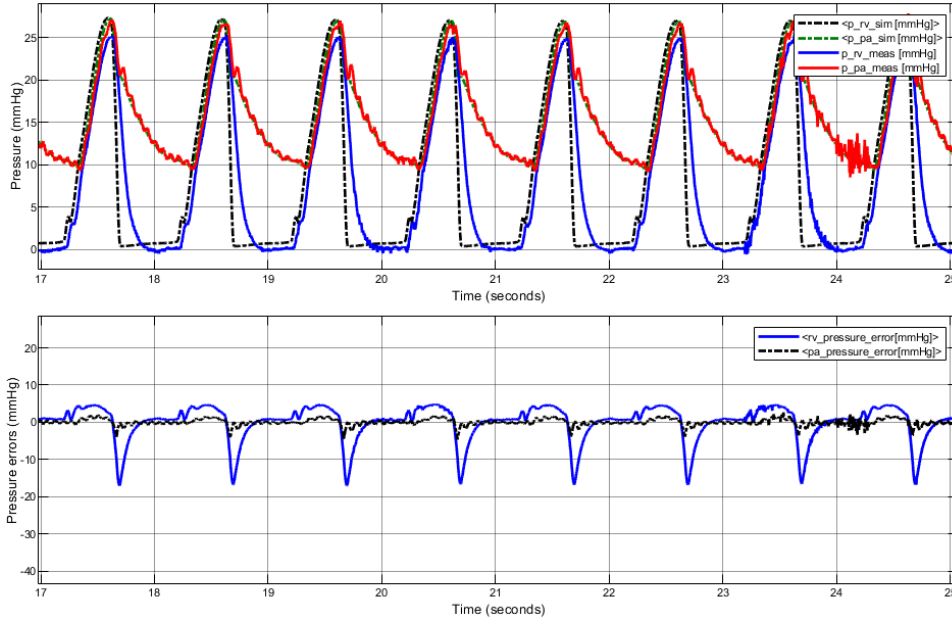


Figure 4.32: Right ventricle pressure waveforms and errors at HR=60 bpm and  $CF_{RV} = 0.8$ ,  $CF_{LV} = 1$ . The solid red line represents the experimental  $P_{P_a}$ , the solid blue line the experimental  $P_{RV}$ , the dotted green line the numerical  $P_{P_a}$  and the dotted black line the numerical  $P_{RV}$ .

In Figure 4.33 the  $P(t)$  waveforms were computed at HR=60bpm and  $CF_{RV} = 0.6$ . Oscillations are still present in the  $P_{P_a}$  tracing. The peak value of the  $P_{P_a}$  is at around 27 mmHg, while the peak of  $P_{RV}$  is lower and reaches 23 mmHg. A delay in the isovolumic relaxation phase is more influential. Smaller delays in the uprising tract of both the pressure waveforms come to light. Nonetheless, still can we appreciate a good capability of the pressure controller to recreate experimental curves that follow the theoretical ones. The average errors are  $err_{P_a} = 0.79$  mmHg and  $err_{RV} = 3.07$  mmHg. In Figure 4.34 the  $P(t)$  waveforms were computed at HR=60 bpm and  $CF_{RV} = 0.5$ . Instabilities are shown in both the  $P_{P_a}$  and  $P_{RV}$  tracings.

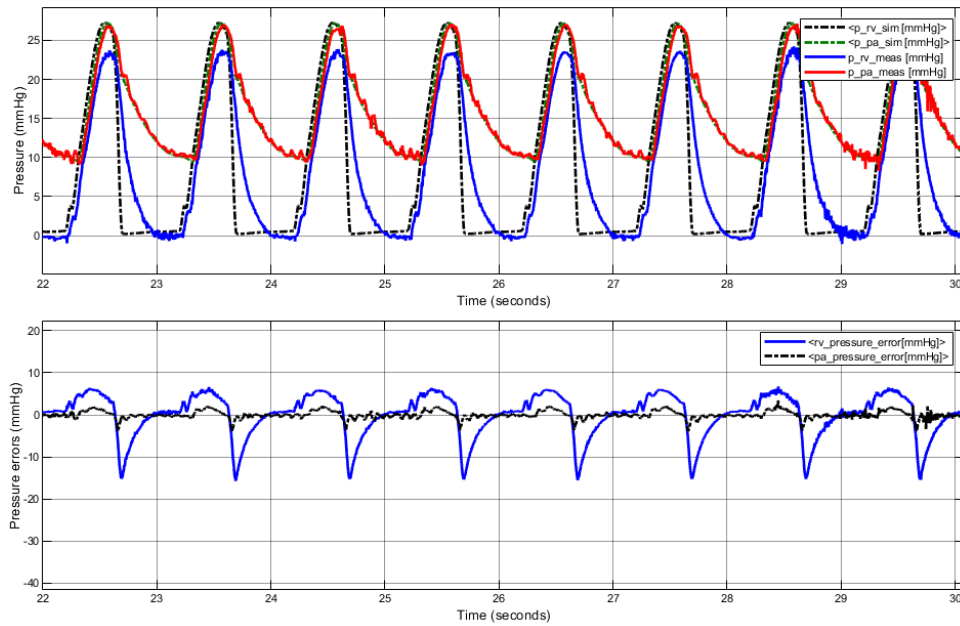


Figure 4.33: Right ventricle pressure waveforms and errors at  $HR=60$  bpm and  $CF_{RV}=0.6$ ,  $CF_{LV}=1$ . The solid red line represents the experimental  $P_{Pa}$ , the solid blue line the experimental  $P_{RV}$ , the dotted green line the numerical  $P_{Pa}$  and the dotted black line the numerical  $P_{RV}$ .

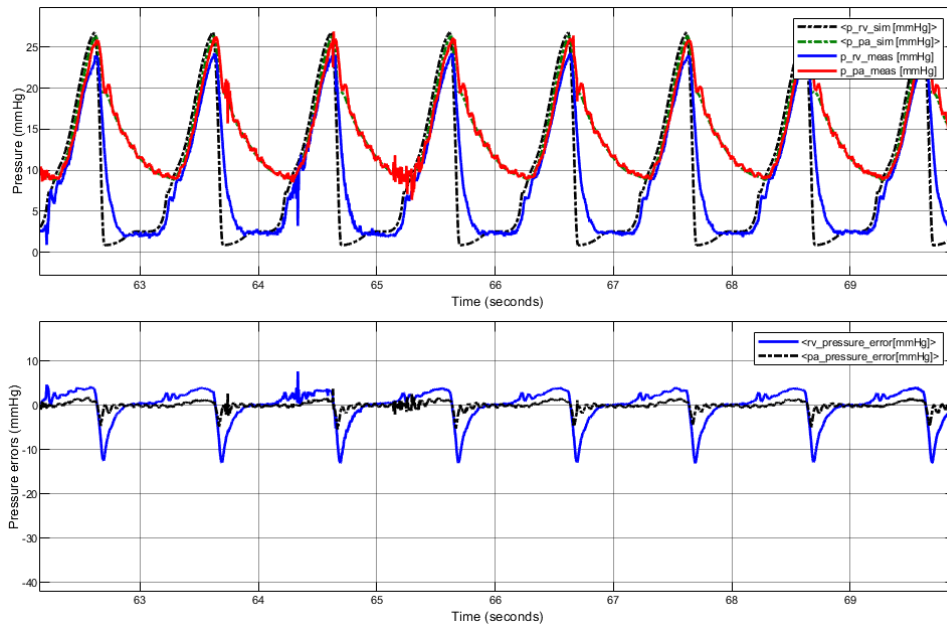


Figure 4.34: Right ventricle pressure waveforms and errors at  $HR=60$  bpm and  $CF_{RV}=0.5$ ,  $CF_{LV}=1$ . The solid red line represents the experimental  $P_{Pa}$ , the solid blue line the experimental  $P_{RV}$ , the dotted green line the numerical  $P_{Pa}$  and the dotted black line the numerical  $P_{RV}$ .

To see our model's performance, the last proof will be derived by the PV loop analysis like we did concerning the left ventricle. Numerical and experimental PV loops are plotted in Figure 4.35 with four different parameter settings:

- Figure 4.35 a shows the theoretical and experimental PV loops at HR=30 bpm CF=1  $\Delta SW=10.53\%$
- Figure 4.35 b shows the theoretical and experimental PV loops at HR=60 bpm CF=1  $\Delta SW=18.15\%$
- Figure 4.35 c shows the theoretical and experimental PV loops at HR=90 bpm CF=1  $\Delta SW=20.03\%$
- Figure 4.35 d shows the theoretical and experimental PV loops at HR=120 bpm CF=1  $\Delta SW=23.78\%$

It's visible that, at lower frequencies, the two tracings tend to be more similar to each other. In every case the main issue is to follow the isovolumic relaxation phase and the ventricular ejection phase. In fact, the experimental tracing gets close but doesn't touch the numerical tracing where the tricuspid valve and the pulmonary valve are meant to open. What's more, we can see that, the smaller the HR, the bigger the right ventricular volume variation is, and, by extension, the bigger the stroke work gets.

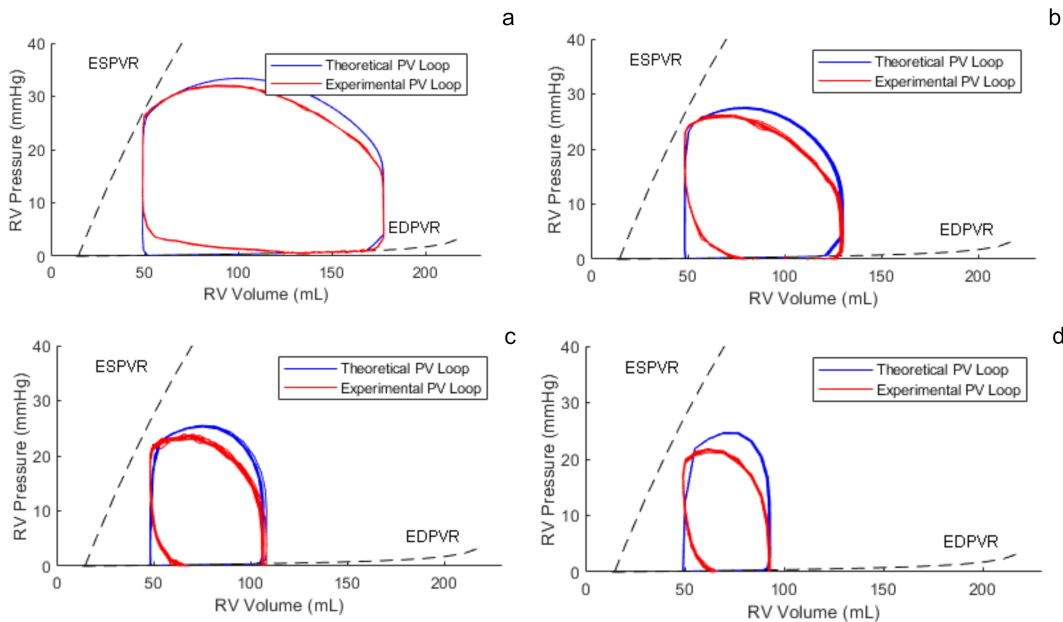


Figure 4.35: Theoretical and experimental right ventricular PV loops considering HR variability. HR=30 bpm (a), HR=60 bpm (b), HR=90 bpm (c), HR=120 bpm (d).

In Figure 4.36 instead PV loops were analysed by varying the CF and keeping the HR to 60 bpm. More specifically:

- Figure 4.36 a shows the theoretical and experimental PV loops at HR=60 bpm CF=1  $\Delta SW=18.15\%$
- Figure 4.36 b shows the theoretical and experimental PV loops at HR=60 bpm CF=0.8  $\Delta SW=18.69\%$
- Figure 4.36 c shows the theoretical and experimental PV loops at HR=60 bpm CF=0.6  $\Delta SW=19.27\%$
- Figure 4.36 d shows the theoretical and experimental PV loops at HR=60 bpm CF=0.5  $\Delta SW=20.95\%$

Here the tracings get more similar as the CF increases. Still the issue of following the isovolumic relaxation and the ventricular ejection is present. When CF decreases, the PV loops shift towards higher values of ventricular volume. The stroke work decreases with a decrease in contraction fraction.

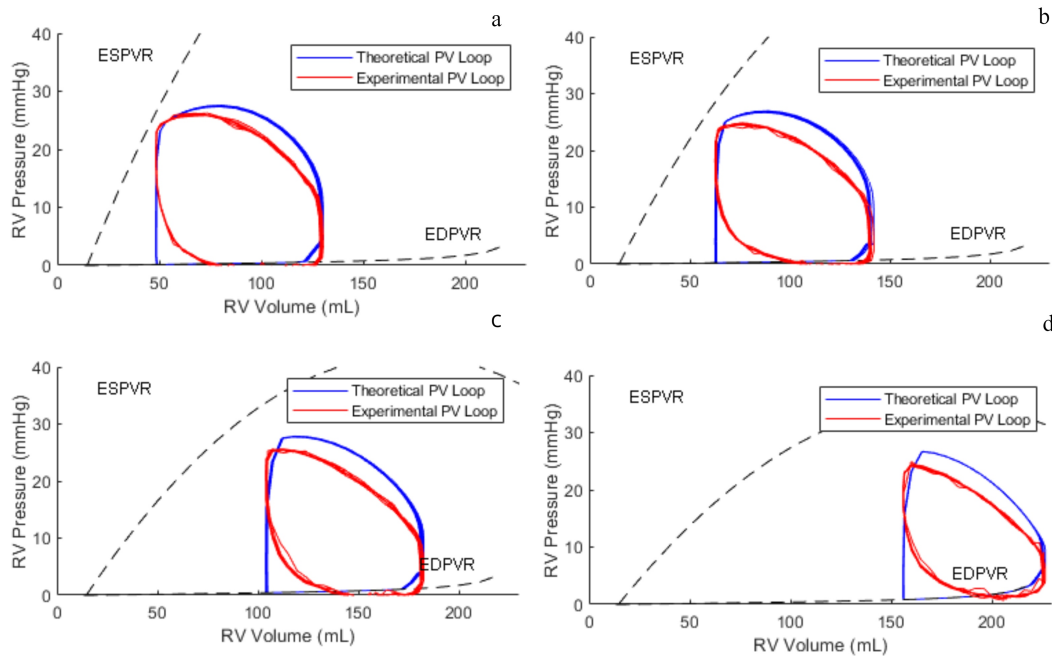


Figure 4.36: Theoretical and experimental right ventricular PV loops considering CF variability. CF=1 (a), CF=0.8 (b), CF=0.6 (c), CF=0.5 (d).

An additional analysis has been made concerning experimental and numerical pressure-volume loops. Not only we want to see if the two tracings are comparable at the same parameters settings, but we also want to verify that the variations of the theoretical PV loop due to a change in a parameter leads to the same amount of variation in the experimental PV loop. With this goal, we extrapolated the SW values for all the following pressure-volume curves. Those values are listed in the table below:

Table 4.2: Experimental and numerical stroke work values.

SW [mL · mmHg]		
	Theoretical	Experimental
<b>CF=1</b>	2028.4	1659.8
<b>CF=0.8</b>	1986.5	1615.2
<b>CF=0.6</b>	1727.8	1394.8
<b>CF=0.5</b>	1375.6	1087.4

Now, analysing a different  $\Delta SW$ , which we'll define as  $\Delta SW_{CF}$  as:

$$\Delta SW_{CF} = \frac{|SW_{CF_i - \Delta_i} - SW_{CF_i}|}{SW_{CF_i}} \cdot 100\% \quad (4.2)$$

We get that:

Table 4.3:  $\Delta SW$  calculations varying contraction fraction.

	Theoretical $\Delta SW_{CF}$	Experimental $\Delta SW_{CF}$
$\Delta SW_{CF=1/CF=0.8}$	2.07%	2.7%
$\Delta SW_{CF=0.8/CF=0.6}$	13.02%	13.64%
$\Delta SW_{CF=0.6/CF=0.5}$	20.4%	22.04%
$\Delta SW_{CF=1/CF=0.6}$	14.82%	15.97%
$\Delta SW_{CF=1/CF=0.5}$	32.18%	34.49%

As we can see from this elaboration, even though the PV loop tracings are incapable of following all the phases of the PV cycle, when changing the CF both theoretical and experimental PV loops vary almost of the same amount.



### 4.3. VAD Assessment

In this section we integrate in the system a ventricular assist device. The tests performed in this section are aimed at understanding how the numerical model interacts with the device and how pressure tracings, volumes and flow rates are influenced by its presence. LVAD can be designed to generate two patterns of perfusion: pulsatile and continuous flow. In the following tests we used a pulsatile VAD and we simulated a continuous one using a centrifugal pump.

For the first tests, we connected the pulsatile VAD (Berlin Heart EXCOR VAD, p25p) to our hybrid mock loop. Therefore, it would put in communication the two LV and Ao tanks by allowing unidirectional flow from the ventricle to the aorta. Before starting the tests, we tuned the beats per minute of the VAD at 90 bpm and the percentage of systole time at 40%. In general, VADs can be used in synchronous and asynchronous ways. Since clinically, the asynchronous configuration is the most widespread, and since we didn't have the possibility to synchronize a VAD with an ECG tracing, we chose to test our VAD as asynchronous. What we did though was to set the frequency of the VAD at the same pathological value we considered in the model, which is 90 bpm. In Figure 4.37 we get the numerical and experimental pressure tracings and the numerical LV volume tracing. This latter tracing is interesting because it shows that the ventricular emptying happens in two subsequent moments, as if two systoles were occurring in a cardiac cycle, showing how the asynchronous VAD is acting.

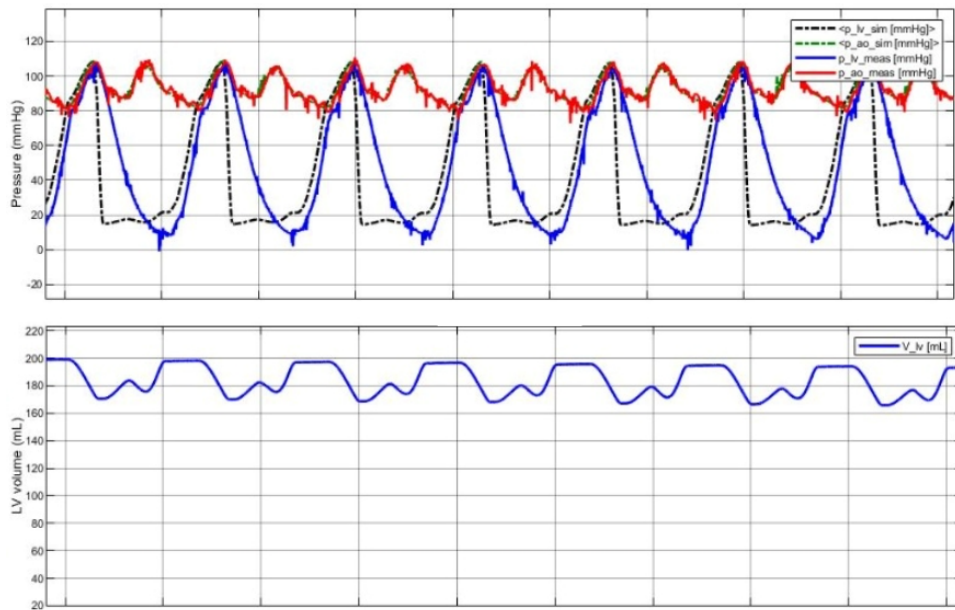


Figure 4.37: Pressure waveforms when VAD assisted (upper). Left ventricle volume waveform when VAD assisted (lower).

The result of the test concerning the VAD applied to the left ventricle can be appreciated also by analysing the PV loops in Figure 4.38.

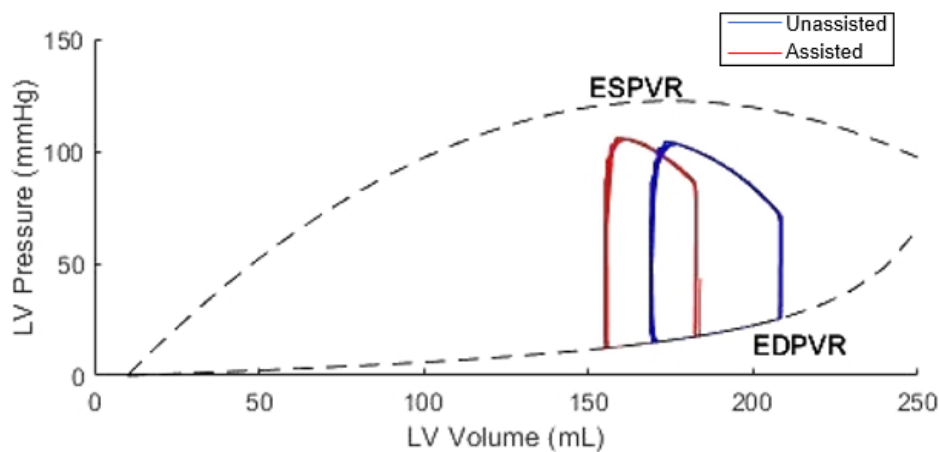


Figure 4.38: PV loop when the left ventricle is working in assisted (red) and unassisted (blue) conditions.

From Figure 4.38 and 4.40 we can clearly see that the VAD is unloading the ventricle. In fact, the area inside of the PV loop, which represents the ventricular stroke work, has reduced. Moreover, the PV loop has slightly shifted leftwards, meaning that the blood

volume inside the ventricle is decreasing. That is a sign that suggests that the VAD is transporting blood from the LV to the Ao. An evident diminishing of the peak pressure is not evident.

This pulsatile VAD has small dimensions, which makes it suitable for non severe heart pathologies, and at its top performances it elaborates an average flow rate of 1.8 l/min and peaks in the flow at around 13-14 l/min, as we can see in Figure 4.39.

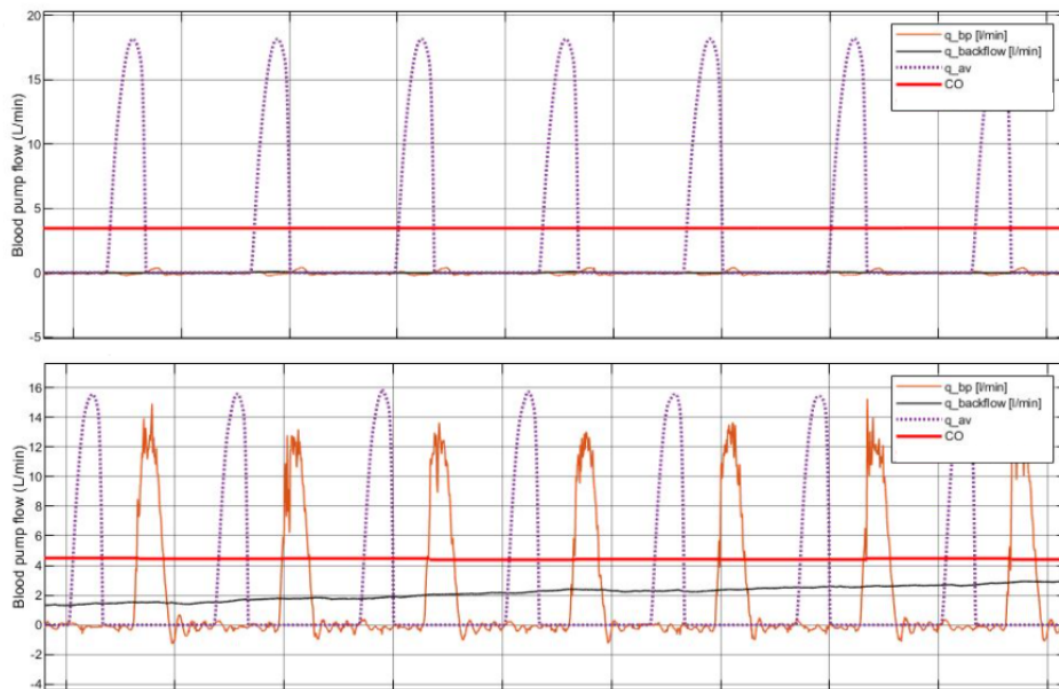


Figure 4.39: Plots of the blood pump flow rate vs time without assistance (upper figure) and with assistance (lower figure).

As for the right ventricle, the results plotted in Figure 4.40 are in accordance with our expectations. Here the VAD was working at an average flow rate of 1.8 l/min, and it is even more noticeable how the PV loop is shifting towards lower volumes. Also a smaller decrease in the peak pressure and a reduction in the PV loop width are present.

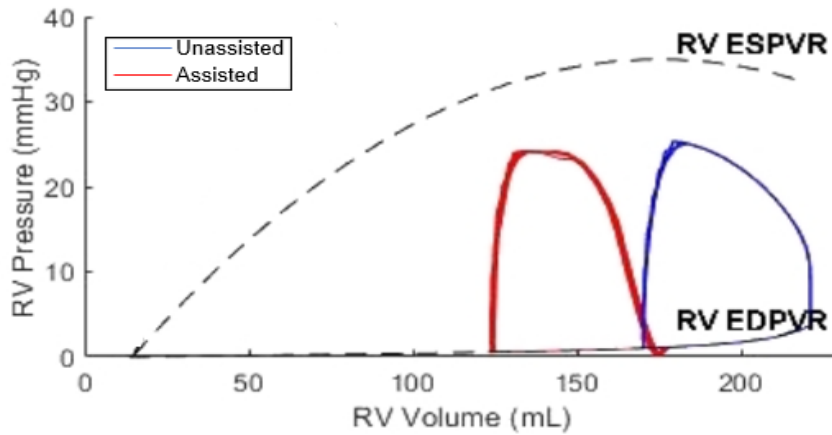


Figure 4.40: PV loop when the right ventricle is working in assisted (red) and unassisted (blue) conditions.

As anticipated, we also performed other tests using a continuous centrifugal pump (Terumo Sarns 3M Delphin, Terumo, Japan) which can be seen as an analogue of a centrifugal flow VAD as far as its functioning is concerned. The centrifugal pump is sensitive to its after-load, which means that the elaborated flow rate, given a constant value of rotations per minute (rpm), may vary due to the different height of the column of fluid in the chamber downstream, or, more in general, because of the pressure in the chamber. We placed a flow probe (H9XL, Transonic systems Inc, USA) downstream the pump, so that our results would be based on an exact measure of the flow rate, instead of the value of rotations per minute, which could have led to uncertainties. In Figure 4.41 pressure tracings and PV loops at different levels of assistance are shown. Pathological conditions of  $HR=90$  bpm and  $CF=0.34$  were chosen for the left ventricle.

As we can see from the results, when the elaborated flow rate increases, the PV loop shifts leftwards (i.e. the LV volume decreases), and the experimental PV loop superposes to the theoretical one better, except for the last part of the isovolumic relaxation and the beginning of the diastolic filling, which is the same issue we noticed in Subsection 4.2.1. We can also see that the  $P_{A_0}$  tracing tends towards a straight line with higher flow rates, while the  $P_{LV}$  tracings slightly shift to lower pressures, with peaks going from about 110 mmHg to about 95 mmHg and valleys from 20 mmHg to 5 mmHg.

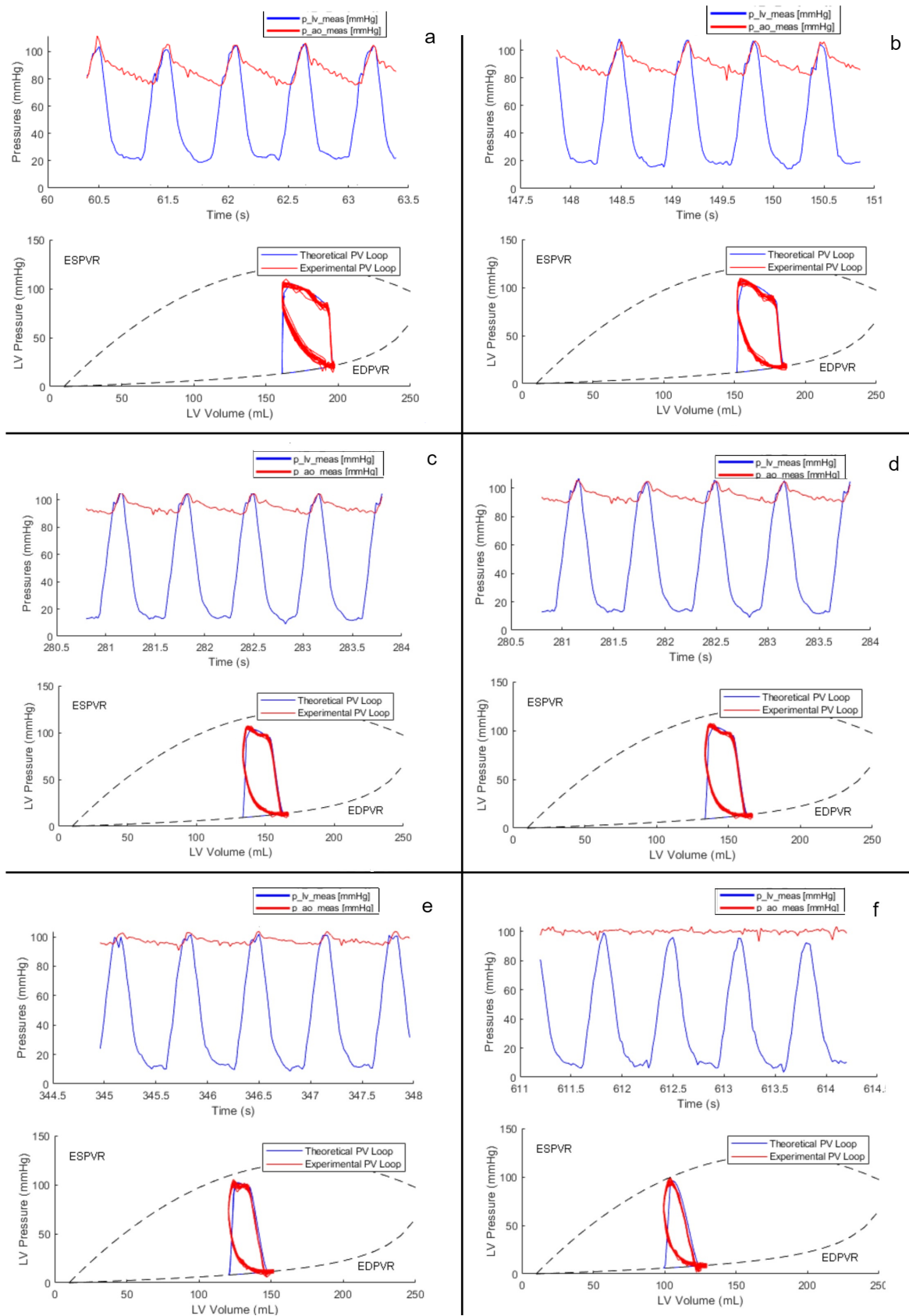


Figure 4.41: Numerical and experimental pressure tracings and PV loops with different levels of assistance. a)  $q_{bp} = 1.1$  l/min. b)  $q_{bp} = 2.1$  l/min. c)  $q_{bp} = 2.7$  l/min. d)  $q_{bp} = 3.3$  l/min. e)  $q_{bp} = 4.1$  l/min. f)  $q_{bp} = 4.8$  l/min.

In Figure 4.42 and Figure 4.43 we analysed the numerical models of the PV loops to see how they changed from the non-assisted condition (solid blue line) to the assisted (dashed blue line) at 4.85 l/min. The pathological conditions were set to HR= 90 bpm and CF= 0.34 for the left ventricle and at HR= 90 bpm,  $CF_{RV} = 0.5$ ,  $CF_{LV} = 0.9$  for the right ventricle. As before, the PV loops shift to the left and their area (SW) reduces.

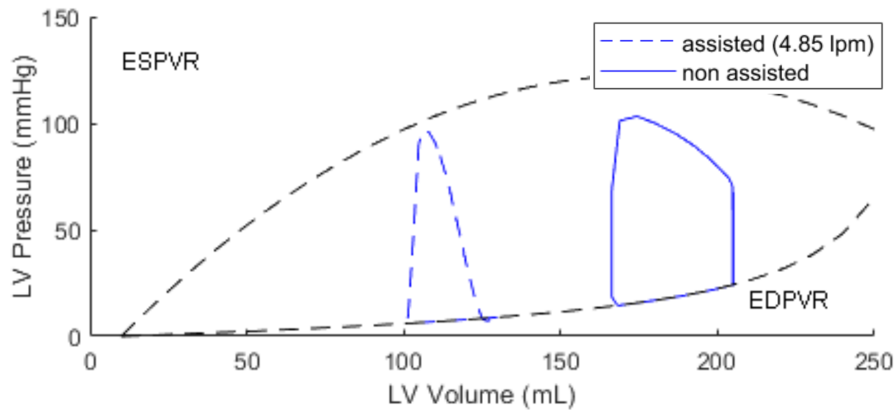


Figure 4.42: Theoretical LV PV loops with and without VAD assistance

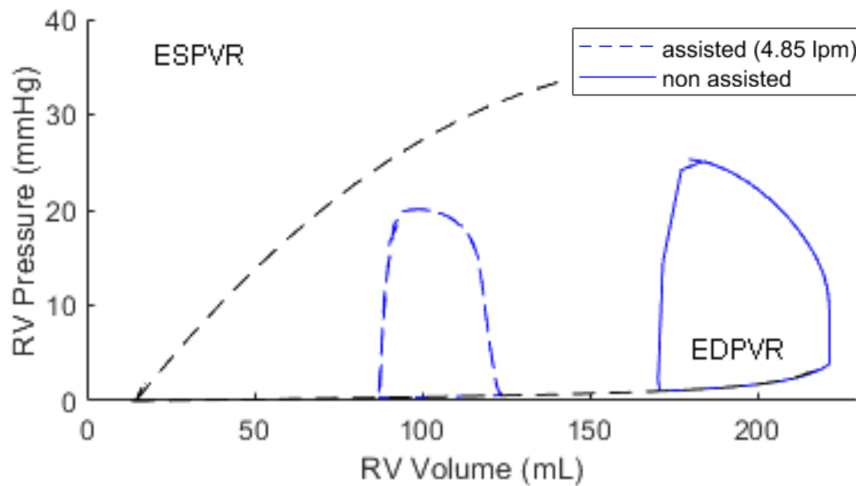


Figure 4.43: Theoretical RV PV loops with and without VAD assistance

In Figure 4.44 the waveform of the flow rate ( $q$ ) with respect to time is portrayed. The purple dashed line ( $q_{av}$ ) represents the numerical tracing of the flow rate passing through a numerically-modeled aortic valve. The solid orange line ( $q_{bp\_MEAN}$ ) instead represents the flow rate generated by the centrifugal pump. The conditions we set for this scenario are once again the pathological ones of HR= 90 bpm and CF= 0.34. At the

beginning of the simulation, no assistance was given by the blood pump (BP), which is shown by the fact that the BP mean flow rate is at zero and the numerical model shows the flow rate the heart would elaborate under those pathological conditions. When assistance is given,  $q_{bp\_MEAN}$  reaches a value of 4.85 l/min, the information is fed from the flowmeter to the numerical model, and the numerical aortic valve flow rate significantly decrease.

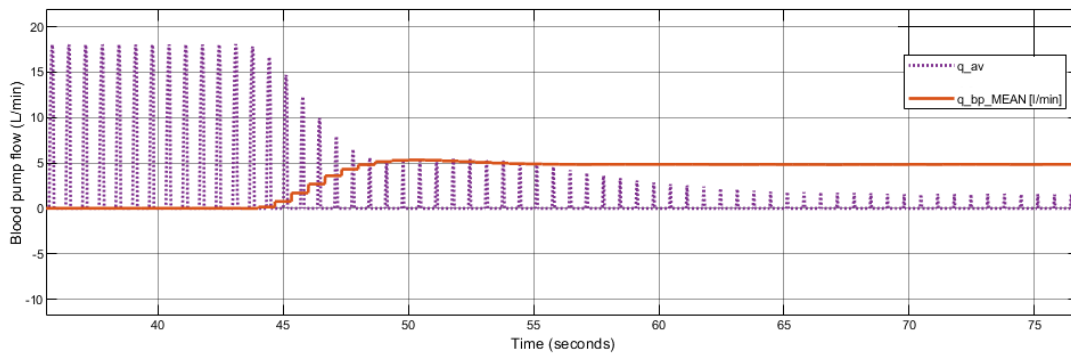


Figure 4.44: Simulated flow rate and actual flow rate elaborated by the centrifugal pump

In Figure 4.45 we can appreciate how the numerical model readjusts when the continuous pump is working when the left ventricle is in pathological conditions. As in Figure 4.44 the pump assistance is delivered starting from  $t=44$  s. The numerical LV pressure ( $p_{lv\_sim}$ ) experiences a widening in its peak-to-valley pressure range, reaching also minimum values around 10 mmHg, whereas the numerical aortic pressure curve ( $p_{ao\_sim}$ ) flattens at 100 mmHg. The left ventricle volume decreases with assistance, going from a range between 170-210 mL to 110-140 mL. In other words, the ventricle gets emptier with assistance. In Figure 4.46 we can see that even the pressures measured by the sensors have the same trend and follow the simulated waveforms.

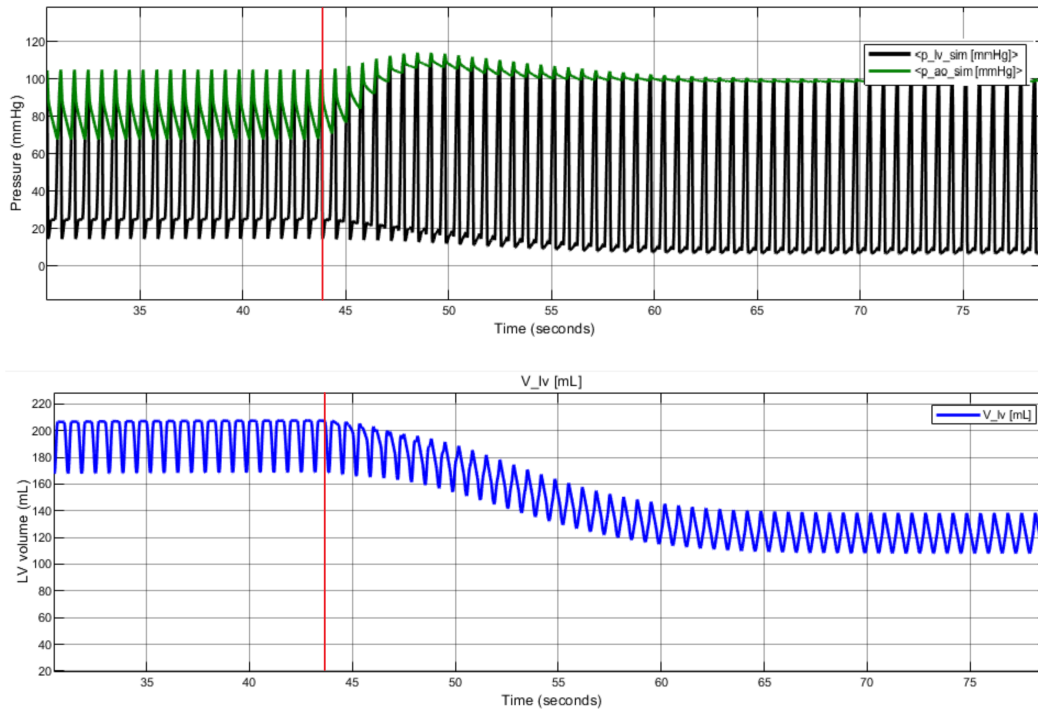


Figure 4.45: Simulated pressure waveforms (LV and Ao) and simulated LV volume waveform. At  $t=44$  s (red line) the VAD assistance is switched on at 4.8 l/min.

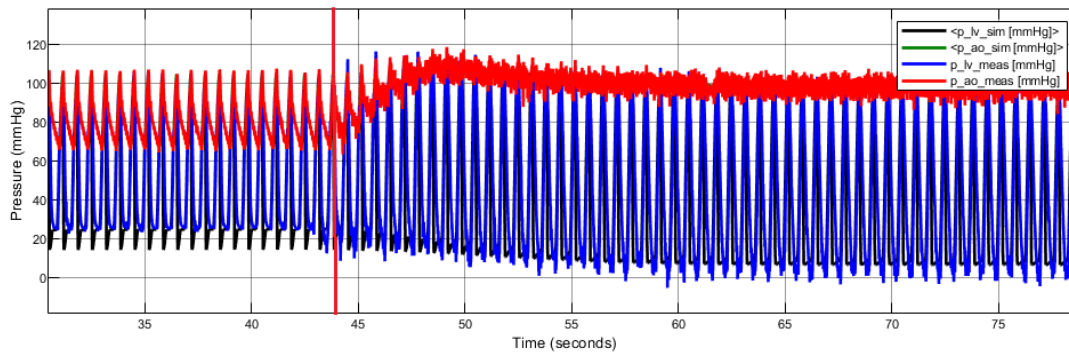


Figure 4.46: Simulated pressure waveforms (LV and Ao) that follow the numerical tracings when at  $t=44$  s (red line) VAD flow rate is delivered.

We have already mentioned in Figure 4.42 and Figure 4.43 that the numerical PV loops readjust according to the assistance level. In Figure 4.47 and 4.48 we analysed in a more detailed way how they change according to the different levels of assistance. Pathological conditions for the LV and RV are set in the HR and CF parameters. The four PV loops all correspond to different pump flow rates.



The PV loop shifts towards lower volumes and lower pressures in both cases. The SW reduces significantly in the LV from  $SW=2878 \text{ mL} \cdot \text{mmHg}$  to  $SW=1800 \text{ mL} \cdot \text{mmHg}$ . Likewise, that trend is displayed in the RV analysis in Figure 4.48.

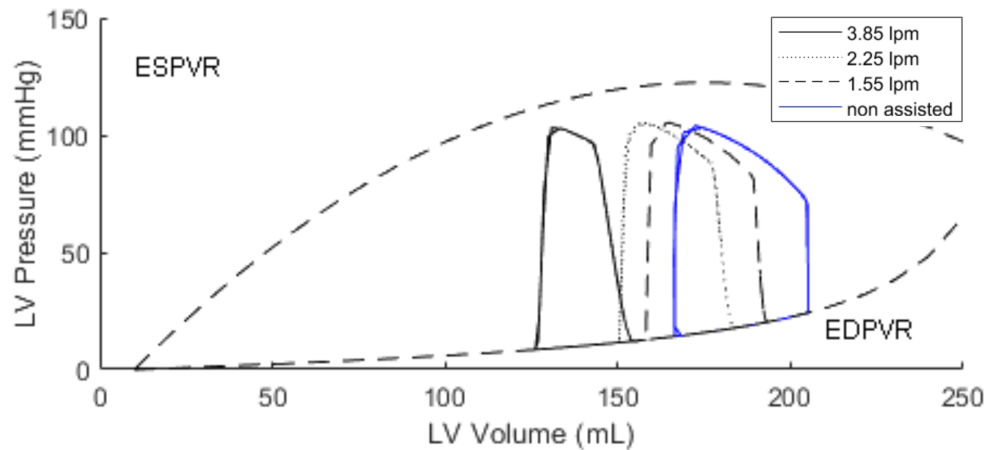


Figure 4.47: Theoretical LV PV loops changes with different levels of assistance. Solid blue line:  $q_{bp} = 0 \text{ l/min}$ ,  $SW=2878 \text{ mL} \cdot \text{mmHg}$ , dashed black line:  $q_{bp} = 1.55 \text{ l/min}$ ,  $SW=2589 \text{ mL} \cdot \text{mmHg}$ , dotted black line:  $q_{bp} = 2.25 \text{ l/min}$ ,  $SW=2418 \text{ mL} \cdot \text{mmHg}$ , solid black line:  $q_{bp} = 3.85 \text{ l/min}$ ,  $SW=1800 \text{ mL} \cdot \text{mmHg}$

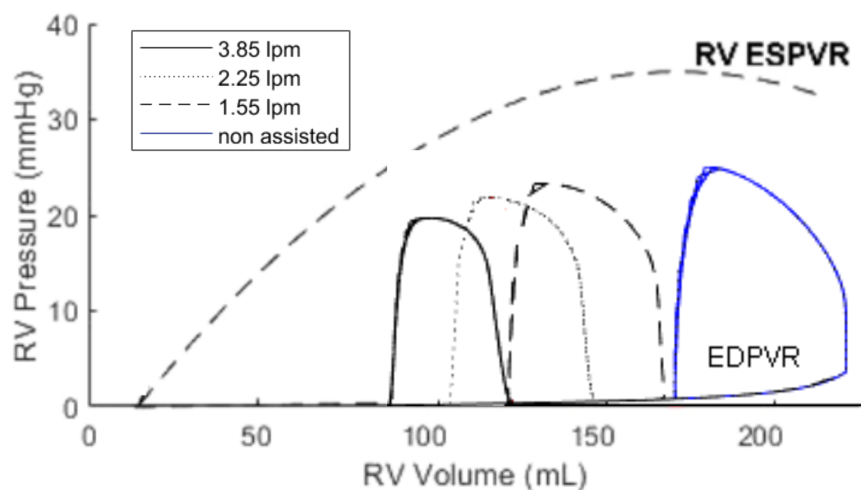


Figure 4.48: Theoretical RV PV loops changes with different levels of assistance. Solid blue line:  $q_{bp} = 0 \text{ l/min}$ , dashed black line:  $q_{bp} = 1.55 \text{ l/min}$ , dotted black line:  $q_{bp} = 2.25 \text{ l/min}$ , solid black line:  $q_{bp} = 3.85 \text{ l/min}$ .

In Figure 4.49 and Figure 4.50 we can see how the systemic arterial resistance ( $R_{sa}$ ),

the pulmonary arterial resistance ( $R_{pa}$ ), the unstressed venous volume (UVV) the mean aortic pressure (MAoP) and the cardiac output (CO) change with variations in the pump flow rate, according to the baroreflex control. The heart is considered to be in pathological conditions (HR= 90 bpm, CF= 0.34). The flow rate of the centrifugal pump was stabilised at 1.7 l/min at  $t=15$  s. Then, at  $t=55$  s (see solid blue line) we switched to a flow rate of 3.05 l/min and at  $t=135$  s (see the other solid blue line) to 4.55 l/min. The trends that can be highlighted are:

- The  $R_{sa}$  reduces with the increment of the VAD assistance.
- The  $R_{pa}$  increases with the increment of the VAD assistance.
- The UVV increases with the increment of the VAD assistance.
- The MAoP increases with the increment of the VAD assistance.
- The CO increases with the increment of the VAD assistance.

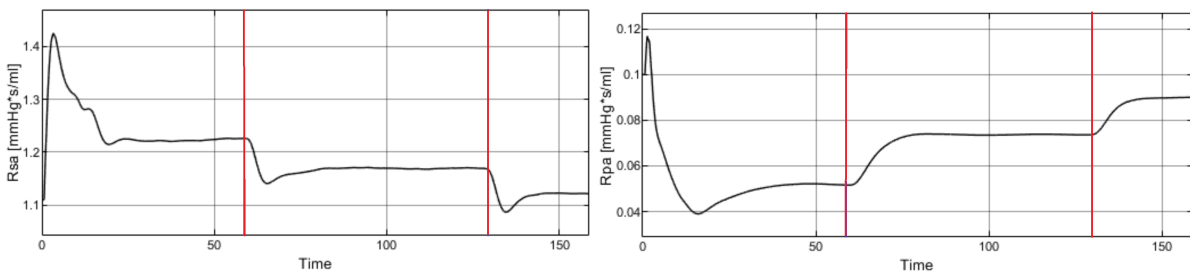


Figure 4.49: Resistance variation at different flow rates.

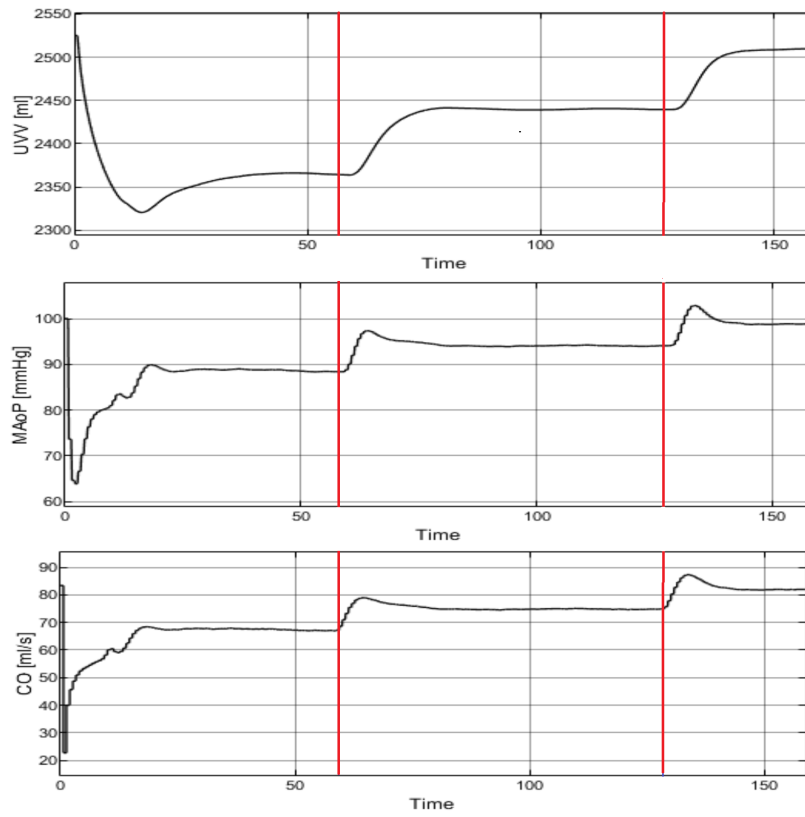


Figure 4.50: UVV, MAoP, CO variations at different flow rates.

We have mentioned before that the LV volume decreases with different VAD flow rates. Here we can see the behaviour of the left atrium volume with different levels of assistance and have a close up on the left ventricle volume. In Figure 4.52 the same levels of assistance as before were taken into consideration so the pump flow rate goes from 1.7 l/min (left) to 3.05 l/min (centre) to 4.55 l/min (right). Both volumes decrease with an increase in the flow rate, the left atrium gets discharged as well. Considering once more those assistance levels, we can have a close up on how the theoretical flow rate through the numerical aortic valve decreases. With a VAD, our numerical heart model will need to elaborate lower flow rates ( $q_{av}$ ). We can see in Figure 4.52 that peaks go from  $q_{av}=230$  ml/s, that is 13.8 l/min (a), to  $q_{av}=155$  ml/s, that is 9.3 l/min (b), to  $q_{av}=40$  ml/s, that is 2.4 l/min (c).

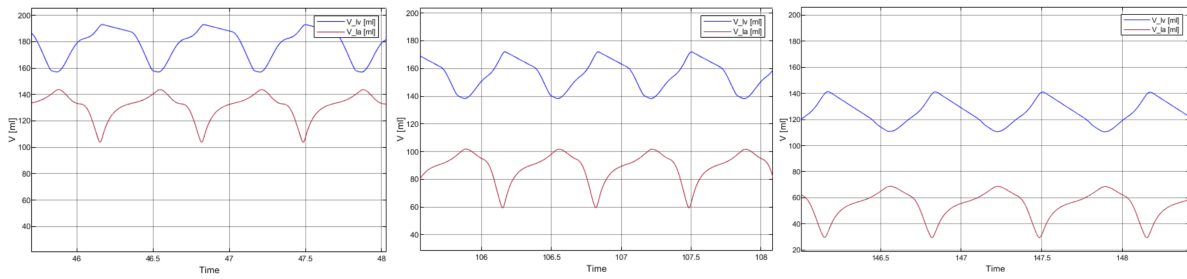


Figure 4.51: LV and LA volumes at three pump flow rates: 1.7 l/min (left), 3.05 l/min (centre), 4.55 l/min (right).

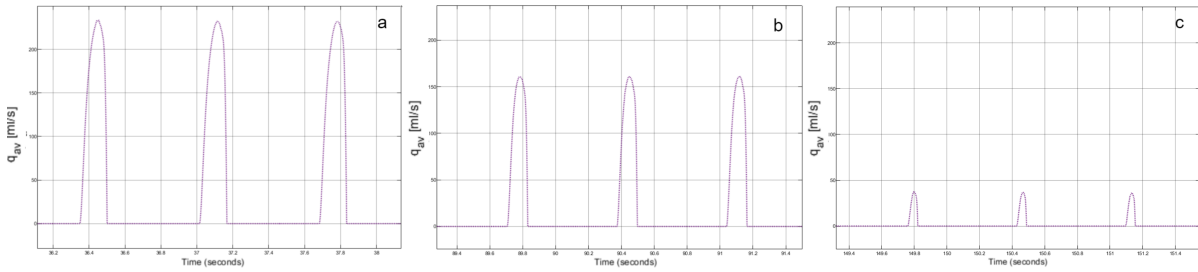


Figure 4.52: Numerical  $q_{av}$  tracings at three pump flow rates: 1.7 l/min (left), 3.05 l/min (centre), 4.55 l/min (right).

# 5 | Discussions and Conclusions

*In this chapter we propose the numerical model validation resof our mock loop has been validated. In Section 5.1 we saw that pressure tracings are capable of quickly adapting when HR and CF are changed in real-time through the GUI and in Section 5.2 the resultant pressure tracings are consistent to what we expected. In Section 5.3 we assess the suitability of our mock loop when a VAD is integrated.*

## 5.1. Numerical Model

The numerical model of our mock loop has been validated and the results are hopeful. The pressure tracings are capable of quickly adapting when HR and CF are changed in real-time through the GUI and the resulting pressure tracings are consistent with what we expected. In particular, when the baroreflex control is acting on peripheral resistances and volumes, the ventricular pressure tends to move to physiological values in a few cycles. This is what we expected accordingly to the literature: when the aortic pressure experiences disturbances in its waveform, and because of that the mean aortic pressure value changes, the baroreflex control tends to restore the physiological conditions. We can easily see that this is not happening in Figure 4.2. When the baroreflex is deactivated in fact, there is a small transient behavior after the HR is changed and then the pressure stabilizes to lower peak values, without any tendency to re-establish the physiological trends. When the baroreflex control is completely activated instead, we can also see the influence on HR. At low frequencies (40 bpm) the baroreflex acts increasing the heart rate in order to guarantee a more physiological value. On the other hand, increasing the frequency to 80 bpm or 120 bpm the baroreflex action works by decreasing the heart rate. In all cases, the changes on HR performed by the baroreceptors control are starting after 20 s because that is the time the model requires to achieve a more stable condition (Figure 4.14).

The pressures response to contraction fraction changes is the one expected too: when the baroreflex controls only Rpa, Rsa and UVV (Figure 4.6) the pressure waveforms tend towards the physiological condition. When the baroreflex control is activated also for the HR control, we can see that in physiological conditions, CF=1 and HR=60 bpm, the baroreflex control activates, but little changes are shown in Figure 4.8. The pressure tracings are in fact already in a physiological state, and the feedback control of our baroreflex model changes HR from values between 59 and 61 bpm.

When considering extremely pathological conditions, with a residual ventricle contractility of 20%, the baroreflex acts in order to increase the HR trying to rise pressure, but since the patient's conditions are too critical, and the heart is therefore too impaired in its contractility, the physiological pressure range (0 mmHg-130 mmHg) can't be achieved.

In conclusion, the sliders GUI control allows the user to easily change HR and CF and we can see the influence of these two parameters when the control of the baroreceptor is completely deactivated. When the baroreflex control is activated instead, the model we implement is capable of restoring a quasi-complete physiological pressure tracing (if the myocardium is not severely impaired) a few seconds after the real-time modifications of

HR and CF, consistently to what we expect by reading the literature.

Pressure-volume loop analysis gives additional worth to the numerical model. Analysing both CF and HR variability, we find results consistent with both the literature and the physiology. Increasing the HR, the end-diastolic volume reduces (Figure 4.10). Matter of fact, since diastole duration is highly dependent on heart frequency, the increase in HR leads to a smaller diastolic time. As a consequence, the left ventricle filling is not complete and so the left ventricular volume decreases, leading to a reduction of the SW too. We can also see in Figure 4.10 that the potential energy of the heart is fixed, while the ventricular stroke work decreases: the total mechanical energy of the ventricular contraction, and so the work required to generate the illustrated cardiac power decreases. Varying the contraction fraction from 1 (healthy) to 0.4 (pathological) and maintaining HR constant at one instead, the Frank-Starling curve slope diminishes and it shifts to the right (Figure 4.12): the response to inotropy decrease is an increase in end-diastolic volume even if the pathological ventricle does not succeed in generating adequate stroke volume. In this case, SW decreases with the reduction of contractility while PE, on the contrary, increases. Lower contractility means less steep ESPVR, smaller PV loops, indicating reduced ejection and lower blood pressure. Reduced ejection results in smaller stroke volume, Higher end-systolic volume results instead in reduced filling. As a consequence, pressure-volume curve shrink and move to the right.

In Section 4.1.4, we end the baroreflex model assessment by looking at HR and Rsa variations directly acting on the aortic pressure and at UVV variations acting on the cardiac output. The arterial baroreflex is an important reflex that acts as a buffer when high fluctuations in aortic blood pressure occur. As explained in Section 3.1.2 the baroreceptors are positioned in the walls of the carotid arteries and of the aortic arch and they are activated by beat-to-beat fluctuations in systemic blood pressure.

We assess the functionalities of our model starting from these physiology-based notions. Accordingly to the literature, the two main actions of the baroreflex feedback are: pressure buffering and cardio-protection [42]. In fact, when carotid sinus pressure increases (we actually consider aortic pressure variations being the two contiguous anatomic district) afferent baroreflex nerve and efferent parasympathetic traffic rises, while efferent sympathetic tone decreases. As a consequence, when blood pressure rises, systemic vascular resistances decrease. Concerning the effects of the baroreflex on the heart-beat instead, we can say that when the blood pressure increases, the baroreceptors act in order to protect the heart rising the parasympathetic tone and decreasing the sympathetic one: consequently, HR decreases. Our results, reported in Figure 4.14, 4.15 are consistent with these considerations. Dealing with the unstressed venous volume we see that increasing

the cardiac output, UVV slightly increases too (Figure 4.16). Consistently to the literature, in particular to the results reported by Lau et al.[43] an increase in pressure results in a rise of the unstressed volume. Our model actually takes as input parameter for the UVV control the cardiac output instead of  $P_{Ao}$ .

In conclusion, the flexibility of our mock loop and the possibility to reproduce different patient conditions has been checked changing the aortic valve resistance in the numerical model, as seen in Section 4.1.5. Several parameters can be changed and monitored, and in our experiment we take the aortic resistance variation into consideration as a paradigmatic example. As we expected, an increase in the valve inflow resistance to a value that can be the one in case of stenosis, leads to higher ventricular pressure and lower flow rate through the aortic valve in the numerical model.

## 5.2. Experimental Tracings

When dealing with the comparison between experimental and theoretical pressure and pressure-volume tracings the left ventricle and right ventricle results are really promising. Even though the pressure gap involved is higher than the right ventricle one, the controller is capable of making the experimental pressure waveforms follow the numerical tracings, especially at low frequencies.

Concerning the left ventricle: tracings do not have issues in following the real time variations of HR (Figure 4.19, 4.20) and CF (Figure 4.21, 4.22). The isovolumic relaxation is highly rapid, the pressure has to drop from 130 mmHg to zero. We can see that, at every HR we considered, the peak of the LV pressure waveform coincides with the peak of the Ao waveform and to the numerical tracings as well. This means that the controller is precise in tracing the numerical model when it comes to activating the electrovalve. Since the experimental model pressure finds it hard to decrease that rapidly, especially at higher HR (Figure 4.25, 4.26), we assumed that it could be due to three main reasons:

- Further optimisation of the controller parameters might be required. That will most likely lead to a bigger amount of oscillations, but it could adjust the tracings in the isovolumic relaxation.
- Inertia of the mechanical components. Once the electrovalve is activated, the pressure drop needs to be of 130 mmHg in 0.04 s (in case HR=120 bpm and CF=1). Even if the vacuum chamber is communicating via the electrovalve to the LV chamber, it requires time for the air to be exhausted, leading to a delay.
- Instability of the compressed air supply line. During the tests, we noticed a vari-



ability in the air flow that was processed by the compressor. Since the venturi vacuum pump elaborates negative pressures depending on the compressed air line pressure, those fluctuations prevented us from keeping the vacuum chamber at -80 kPa continuously. Changes in the vacuum pressure have led to issues in the pressure tracings and in the PV loops width.

In the PV loops it's even more evident that the experimental model can't follow the isovolumic relaxation tract as HR increases (Figure 4.27) . As stated, the experimental pressure tracings have issues in that part. For our tests, experimental PV loops have been computed using those LV pressure waveforms, but we exploited the numerical ventricular volume curve, which is merely theoretical. That was required because of our set-up, because a two chamber model doesn't allow us to compute the flow rate between the atrium and the ventricle. The backflow pump brings back fluid to balance the emptying of the chamber. That fluid would have had to be stored in an atrium chamber and then be delivered following other numerical laws and pressure tracings. Therefore, the theoretical ventricle volume doesn't suffer from the same delays that the experimental pressure undergoes to, but it's in phase with the numerical pressure waveform. This leads to a mismatch that causes the PV loops to be unable to replicate that isovolumic relaxation and the initial part of the ventricular filling.

Right heart failure is usually a result of left ventricular failure via volume and pressure overload [44]. That is the reason why when choosing the right ventricle configuration in the GUI, three slicers appear, giving the user the possibility to change HR, left ventricular contraction fraction and right ventricular contraction fraction. Figure 5.1 displays the GUI layout, where at first both the CFs are 1 and the HR is 60 bpm, so to compute pressure and pressure-volume curves in physiological conditions.

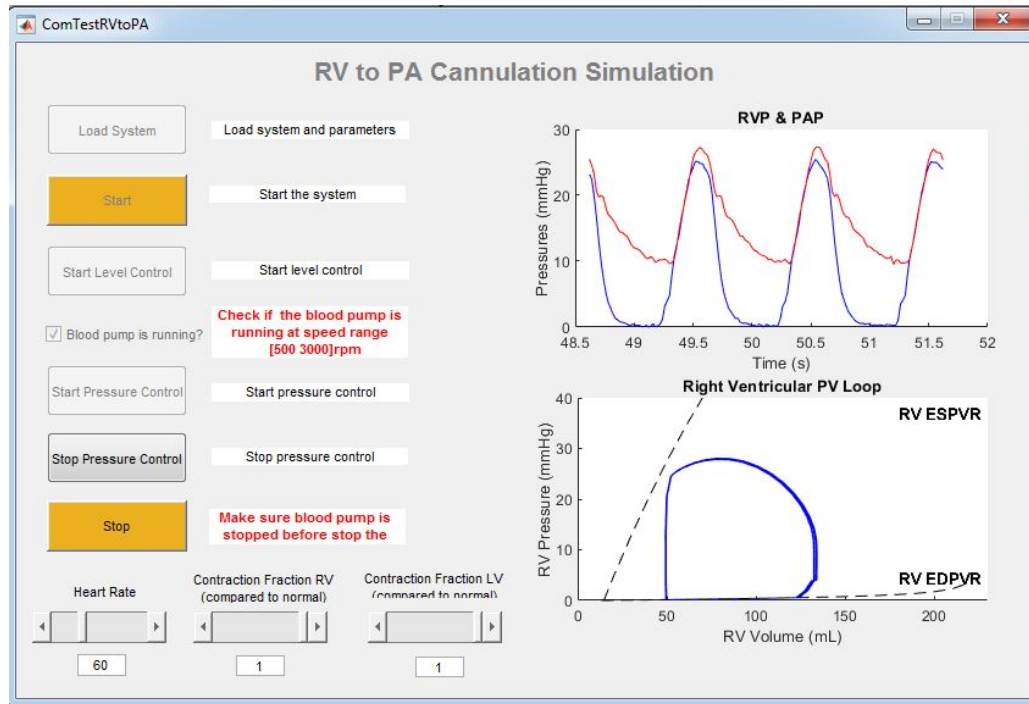


Figure 5.1: Graphic User Interface when choosing right cannulation.

Overall, the measured pressures follow the trend of the simulated ones with little average errors, which diminish with smaller HR and bigger  $CF_{RV}$ . Here as well we have the same issues we faced in the systolic descending tract, for the same reasons mentioned before. When it comes to the isovolumic contraction, we witness a delay that was present only at HR=120 bpm in the left ventricle (Figure 4.26). This is definitely due to the pressure control parameters which, in order to follow the tracing without many instabilities, have to give in a bit of accuracy.

Average errors are less relevant in modulus with respect to the left ventricle case (5.1 and that is consistent with the fact that lower pressures are involved in the RV analysis. The ventricle pressure delay in the descending phase is short. A smaller error is also present in the systolic peak. The results concerning the pulmonary artery waveforms are satisfactory: the measured pressures follow the dotted green line in an accurate way, adequately reproducing the dicrotic notch, mimicking the little backflow of blood back into the ventricle. When it comes to oscillations, we noticed that some of them, like the ones in Figure 4.32 and Figure 4.34 occur when the backflow pump gets activated and delivers water to the RV chamber. They are localised and stabilize within a cycle or two. As for the fluctuations in Figure 4.28, they are due to the controller. We chose values for  $K_p$  and  $T_i$  (Table 3.4) to ensure a better stability at higher frequencies, being a value of HR around 30 bpm unrealistic in medical scenarios.

As far as the RV-PV loops are concerned, the main reasons why they don't overlap (Figure 4.35) are always the same as the LV-PV loops. The same delays we found in the  $P(t)$  tracings are carried also in these graphs. We saw that the ventricular ejection was well followed in the LV, so it can't be a matter of inertia or vacuum pressure instabilities, but it can be due to the controller parameters. One of the most important results concerning the right ventricular pressure-volume loop is the one proposed in Table 4.3 when analysing the tracings varying the right ventricle CF (Figure 4.36). In particular, we saw that the experimental curves are not perfectly matching the theoretical ones but, changing the contraction fraction value, the stroke work changes by the same amount for both tracings. This means that our hybrid mock loop displays accurately the betterment or the worsening of the heart conditions in both numerical and experimental tracings. This conclusion bears significant relevance because it shows the suitability of our mock loop when a VAD is integrated in the system.

Table 5.1: Pressure errors with HR variability.

	$err_{LV}[mmHg]$	$err_{Ao}[mmHg]$	$err_{RV}[mmHg]$	$err_{Pa}[mmHg]$
<b>HR=30</b>	5.82	1.2	1.68	0.91
<b>HR=60</b>	10.82	1.46	2.78	0.98
<b>HR=90</b>	17.04	1.47	3.42	1.18
<b>HR=120</b>	19.7	2.54	5.02	1.39

The purpose of the VAD is to unleash the heart from its work overload by emptying the ventricle on his behalf. This action will therefore affect the PV loop, whose stroke work reduces significantly according to the levels of assistance. As in the CF analysis, where that parameter acts on the numerical model of our heart, with a VAD insertion the experimental PV loop will also be computed using the measured LV pressure, which is generated by a control scheme to follow the numerical. In other words, a VAD will influence the numerical model of the PV loop, and the experimental one will follow that. The principle that lies underneath is therefore the same as the CF analysis, hence the conclusions. Knowing that, with a change in CF, the SW of the experimental PV loop varies by the same amount as the theoretical PV loop, even though they don't overlap, ensures us of the fact that equal changes in the theoretical SW due to the ventricular assistance will be shown in the experimental SW. This conclusion is valid by keeping in mind that the PV loop has been computed over the theoretical volume tracing, so the

experimental volume of fluid that gets carried from the ventricle towards the aorta is not entering the equation.

Because of the fact that we numerically see the effects of the inflow valve resistance variation, we also deal with the measure of the physical flow rate. When actually measuring the flow through the valve with a flowmeter, despite the numerical result, it increases (Figure 5.2). This what we expected due to the rise in the trans-valvular pressure. In fact, the real valve we are testing can't change its resistance, so it will only experience an increase in the flow rate due to the increase in  $\Delta P$  according to the equation:

$$\Delta P = R \cdot Q \quad (5.1)$$

What we notice though is that in Figure 5.2 the peak flow rates are very low compared to the physiological ones, which means that our mock loop is not suitable for tests on valves. A wider overview on the reasons for that is provided in Chapter 6.

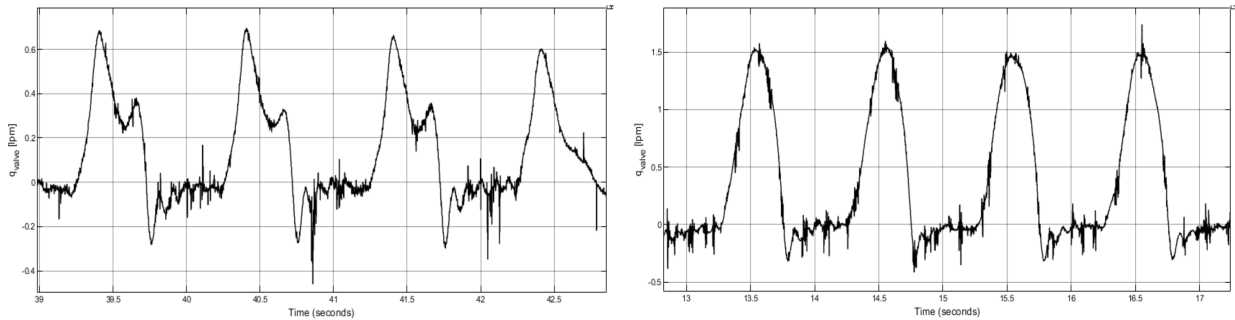


Figure 5.2: Experimental flow rate through the valve: on the left  $R_{valve} = 0.00375 \text{ mmHg} \cdot \text{s/ml}$ , on the right  $R_{valve} = 0.08 \text{ mmHg} \cdot \text{s/ml}$ .

### 5.3. VAD Integration in Mock Loop

In general, our mock loop interacts well with the VAD. Its action is fed into the numerical model by means of the DAQ board, using the signal from the flowmeter as an input.

With the pulsatile VAD, what is revealed is a limit due to asynchrony between the VAD pulsation frequency and the heart rate of the patient. For that reason, non-physiological peaks have appeared in the  $P_{A_0}$  tracings and in the LV volume curve. Even if the HR and the VAD pulsations were set at the same value, they have to be in phase as well, which requires ECG synchronization. The flow rates experience the same out-of-phase issue as visible from Figure 4.39

In the numerical method (Figure 4.38, 4.40) we can appreciate, by looking at the theoretical PV loops, that the assistance is working and that the VAD is unloading the ventricle. Since its dimensions are small, not a huge decrease in SW can be appreciated, but both for the LV and the RV analysis, the ventricles empty a little bit and shift towards lower volumes. The reason why pressure peaks don't change is due to the fact that the flow rate that goes to the aorta is the sum of the one that exits the aortic valve and the one that comes from the VAD, therefore the overall flow rate is practically the same. We can clearly see how the assistance that the VAD provides changes between the LV and the RV case. That explains why research is now leaning towards the development of specific VADs to assist the right ventricle (RVAD) different from the ones used to assist the left ventricle (LVAD).

When using a continuous centrifugal pump, we can appreciate better what happens with different levels of assistance. We see in Figure 4.41 how PV loops shift towards lower LV volumes and that the  $P_{Ao}$  curve flattens. That is due to the fact that, the more the VAD works, the more the flow rate will not rely on the heart, and the less it will display the pulsatility that the pump doesn't produce. Being a constant flow in time, the pressure getting in the aorta will be constant in time as well. This can also be appreciated by having a look at the numerical tracing of the  $P(t)$  in Figure 4.45 and at the experimental tracing of the  $P(t)$  in Figure 4.46. This flattening of the  $P_{Ao}$  causes issues when it comes to the peripheral vasculature. Some districts may remain closed because they don't perceive a variation in  $P(t)$  ( $\frac{\partial P}{\partial t}=0$ ). In fact, without a pulsatile pressure waveform, no change of shear stress is experienced by the endothelium, which becomes incapable of producing nitric oxide, an important vasodilator. Experimental tracings are well able to follow the numerical tracings in the PV loop, except for the last part of the iso-volumetric relaxation and the beginning of the ventricular filling. It's interesting to see in Figure 4.42 that the numerical model of the assisted PV loop goes towards a triangular shaped PV loop, which is typical of the heart condition with high impairments. In fact, at that level of assistance, the heart is practically not working, and the ventricular ejection is almost absent.

Bigger variations, with respect to the pulsatile VAD, in the theoretical PV loops (Figure 4.47), LV volume (Figure 4.51) and in the numerical flow rate (Figure 4.44) may be appreciated. Though we have lost the pulsatile flow rate we had before, we clearly see that the numerical model doesn't need to elaborate high flow rates when the workload is distributed to the VAD as well.

As for the UVV, MAoP and resistances, the results of our model are in accordance to the results by Jansen [36]. For the CO, we can see an increase in that that matches the results from Colacino [34], considering the CO as the output that exits the myocardium

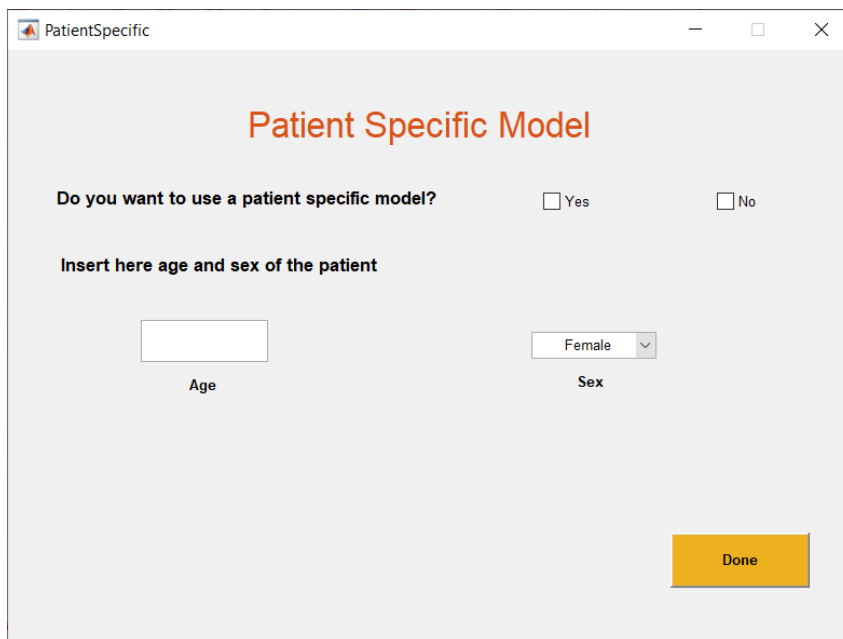
added to the one elaborated by the blood pump. Without any assistance, the CO ejected by the heart in pathological conditions of HR= 90 bpm and CF=0.34 is around 58 ml/s (3.5 l/min).

## 6 | Future Developments

*In this chapter the conclusive considerations are reported. Possible solutions to issues that we experience during the validation and testing phase are presented. In the last part of the section, we deal with future developments.*

As for now, we validated our mock loop as a standalone when it comes to recreate pressure tracings, we validated the numerical model that lies underneath it and we proved its capability of showing the effects of VAD assistance on a patient's pressure tracings and PV loops. Based on what we have acknowledged from tests and corresponding results, our mock loop proves to be efficient in replicating the physiological pressure waveforms and PV loops, even when a ventricular assist device is implanted. Pressure tracings definitely show room for improvement, as we deeply explain in Section 5.2, it can be done for example by making controller optimizations or by solving instability issues of the compressed air supply line.

This mock loop could even become more versatile in the future if it could adjust the value of the model parameters according to a patient's age, sex and clinical conditions. To proceed towards a customization of the model, we took a first step preparing a graphic user interface for that purpose. It will pop up when the user clicks on the "Load Parameter" button. Here the user is allowed to choose whether he wishes to apply a patient specific model or not (Figure 6.1). It is just a small step of course, the achievement of a real patient-specific model is really complicated, especially because the actual value for resistances, compliances and for all the vasculature parameters is not easy to be measured directly from the patient itself. It's easier to set the variation of some parameters based on the general population data. For example, average parameter values based on sex and age, can be extrapolated from papers as the ones of Miyachi et al.[45] Tanaka et al.[46] and Mohiaddin et al.[47]



The image shows a software window titled "PatientSpecific" with a standard Windows-style title bar (minimize, maximize, close buttons). The main content area has a light gray background. At the top, the text "Patient Specific Model" is displayed in a bold, orange font. Below this, there is a question: "Do you want to use a patient specific model?". To the right of this question are two checkboxes: "Yes" and "No", both of which are currently unchecked. Underneath the question, there is a prompt: "Insert here age and sex of the patient". This prompt is followed by two input fields. The first is a text input field labeled "Age" below it. The second is a dropdown menu labeled "Sex" below it, which currently shows "Female" and has a small downward arrow on its right side. At the bottom right of the window, there is a prominent yellow button with the text "Done" in black.

Figure 6.1: Patient Specific GUI.



As mentioned, parameters could be controlled even more by considering specific diseases that affect that patient. Resistances and compliances of an individual may change if he has arteriosclerosis, high cholesterol levels, tachycardia, stent implantation, if he's a smoker and so on and so forth. There's a huge room for improvement by tuning several parameters in the numerical model as to adjust accordingly. It will definitely require a lot of clinical studies and results to be implemented. So far, in literature we were able to find a few parameters to readjust the stroke volume and HR according to the age of the patient, but not much for the other parameters. We can see that as a further improvement to enhance the versatility of the hybrid mock loop.

Since the mock loop demonstrates to be a good generator of physiological waveforms, tests on valves could be performed. Of course, this assessment is not in conformity with the ISO 5840-1:2021 Standard. For that reason the simulator can't be used for authorising the roll-out of the device in the market, but only to do further evaluations on important parameters such as the Effective Orifice Area, Discharge Coefficient and Performance Index.

When we tried validating an aortic valve, instead, we noticed that, even though our mock loop can recreate pressure tracings, the flow rate that will in reality stream through the valve won't be realistic. The results show that the physical polymeric valve opens more widely when changing the inflow resistance ( $R_{dir}$ ) parameter in the Colacino model of the valve. We have to take into account that the pressure tracings we reproduce with our simulator show that the aortic pressure is, most of the time, at higher pressures than the LV pressure. The average  $\Delta P$  that we measured from our recreated pressure waveforms in the ejection phase, which is when the  $P(t)_{LV}$  overcomes the  $P(t)_{Ao}$ , was at 0.195 mmHg. Such a small difference was hardly detected and the valve opened very little, as shown by the  $Q(t)$  tracing and the EOA. As a future improvement, what could be done to characterise valves is create a volumetric test bench, whose goal is to replicate the  $Q(t)$  tracing and adjust pressures consistently. The  $\Delta P$  will increase enough to reach the desired flow rate. Another route could be to regulate the value of the numerical  $R_{dir}$  according to the actual value of the valve resistance. We saw that the  $P(t)_{LV}$  changes and increases when the resistance increases (i.e. in stenotic valves). Using a hybrid mock loop and adjusting the resistance in real time could make for a realistic flow rate waveform.



## Bibliography

- [1] Marco Viceconti, Francesco Pappalardo, Blanca Rodriguez, Marc Horner, Jeff Bischoff, and Flora Musuamba Tshinanu. In silico trials: Verification, validation and uncertainty quantification of predictive models used in the regulatory evaluation of biomedical products. *Methods*, 185:120–127, 2021.
- [2] The Editors of Encyclopaedia Britannica. Pulmonary Circulation, 2020.
- [3] Daniel Liden. What is Systemic Circulation?
- [4] Karthik Suresh and Larissa A Shimoda. Lung circulation. *Comprehensive Physiology*, 6(2):897, 2016.
- [5] Department of Anatomy, Neurobiology, Virginia Commonwealth University School of Medicine the Office of Faculty Affairs, and the ALT Lab at Virginia Commonwealth University. Semilunar valve.
- [6] The anatomy and function of the atrioventricular valves.
- [7] Jan Hendrik van Weerd and Vincent M Christoffels. The formation and function of the cardiac conduction system. *Development*, 143(2):197–210, 2016.
- [8] Alan Kennedy, Dewar D Finlay, Daniel Guldenring, Raymond Bond, Kieran Moran, and James McLaughlin. The cardiac conduction system: generation and conduction of the cardiac impulse. *Critical Care Nursing Clinics*, 28(3):269–279, 2016.
- [9] SS Mehta and NS Lingayat. Detection of p and t-waves in electrocardiogram. In *Proceedings of the world congress on Engineering and computer science*, pages 22–24. Citeseer, 2008.
- [10] PhD Richard E. Klabunde. Frank-Starling Mechanism, 2015.
- [11] John Hall and Michael E Hall. Guyton & hall. fisiologia medica. con test di autovalutazione: 2 volumi+ test di autovalutazione. Edra, 2022.
- [12] Anthony V Delicce and Amgad N Makaryus. Physiology, frank starling law. 2017.

- [13] PJ Blanco, PR Trenhago, LG Fernandes, and RA2911312 Feijóo. On the integration of the baroreflex control mechanism in a heterogeneous model of the cardiovascular system. *International journal for numerical methods in biomedical engineering*, 28(4):412–433, 2012.
- [14] Elena Cuenca-Navalon, Thomas Finocchiaro, Marco Laumen, Andreas Fritschi, Thomas Schmitz-Rode, and Ulrich Steinseifer. Design and evaluation of a hybrid mock circulatory loop for total artificial heart testing. *The International journal of artificial organs*, 37(1):71–80, 2014.
- [15] S Magder. Volume and its relationship to cardiac output and venous return. *Critical care*, 20(1):1–11, 2016.
- [16] Femke Cappon, Tingting Wu, Theodore Papaioannou, Xinli Du, Po-Lin Hsu, and Ashraf W Khir. Mock circulatory loops used for testing cardiac assist devices: A review of computational and experimental models. *The International Journal of Artificial Organs*, 44(11):793–806, 2021.
- [17] M Darowski, M Kozarski, G Ferrari, K Zieliński, K Górczyńska, A Szczepanowski, KJ Pałko, LIBERA Fresiello, and A Di Molfetta. A new hybrid (hydro-numerical) model of the circulatory system. *Bulletin of the Polish Academy of Sciences. Technical Sciences*, 61(4), 2013.
- [18] Gianfranco Ferrari, Claudio De Lazzari, Maciej Kozarski, Fabrizio Clemente, KRYSZYNA Górczyńska, Rita Mimmo, Eliana Monnanni, Giancarlo Tosti, and Marco Guaragno. A hybrid mock circulatory system: testing a prototype under physiologic and pathological conditions. *ASAIO journal*, 48(5):487–494, 2002.
- [19] G Ferrari, M Kozarski, C De Lazzari, K Górczyńska, G Tosti, and M Darowski. Development of a hybrid (numerical-hydraulic) circulatory model: prototype testing and its response to iabp assistance. *The International journal of artificial organs*, 28(7):750–759, 2005.
- [20] Anastasios Petrou, Marcus Granegger, Mirko Meboldt, and Marianne Schmid Daners. A versatile hybrid mock circulation for hydraulic investigations of active and passive cardiovascular implants. *Asaio Journal*, 65(5):495, 2019.
- [21] M Kozarski, G Ferrari, F Clemente, K Górczyńska, C De Lazzari, M Darowski, R Mimmo, G Tosti, and M Guaragno. A hybrid mock circulatory system: development and testing of an electro-hydraulic impedance simulator. *The International Journal of artificial organs*, 26(1):53–63, 2003.

- [22] Maciej Kozarski, Gianfranco Ferrari, Krzysztof Zieliński, Krystyna Górczyńska, Krzysztof J Pałko, Arkadiusz Tokarz, and Marek Darowski. A new hybrid electro-numerical model of the left ventricle. *Computers in biology and medicine*, 38(9):979–989, 2008.
- [23] Gregor Ochsner, Raffael Amacher, Alois Amstutz, André Plass, Marianne Schmid Daners, Hendrik Tevaearai, Stijn Vandenberghe, Markus J Wilhelm, and Lino Guzzella. A novel interface for hybrid mock circulations to evaluate ventricular assist devices. *IEEE transactions on biomedical engineering*, 60(2):507–516, 2012.
- [24] Frank Nestler, Andrew P Bradley, Stephen J Wilson, Daniel L Timms, O Howard Frazier, and William E Cohn. A hybrid mock circulation loop for a total artificial heart. *Artificial organs*, 38(9):775–782, 2014.
- [25] Daniel Timms, Mark Hayne, Keith McNeil, and Andrew Galbraith. A complete mock circulation loop for the evaluation of left, right, and biventricular assist devices. *Artificial organs*, 29(7):564–572, 2005.
- [26] Alfio Quarteroni, Alessandro Veneziani, and Christian Vergara. Geometric multi-scale modeling of the cardiovascular system, between theory and practice. *Computer Methods in Applied Mechanics and Engineering*, 302:193–252, 2016.
- [27] BM Hanson, MC Levesley, K Watterson, and PG Walker. Hardware-in-the-loop-simulation of the cardiovascular system, with assist device testing application. *Medical engineering & physics*, 29(3):367–374, 2007.
- [28] L De Pater and JW Van den Berg. An electrical analogue of the entire human circulatory system. *Medical electronics and biological engineering*, 2(2):161–166, 1964.
- [29] G Ferrari, M Kozarski, C De Lazzari, K Górczyńska, R Mimmo, M Guaragno, G Tosti, and M Darowski. Modelling of cardiovascular system: development of a hybrid (numerical-physical) model. *The International Journal of Artificial Organs*, 26(12):1104–1114, 2003.
- [30] Marcus Granegger, Martin Schweiger, Marianne Schmid Daners, Mirko Meboldt, and Michael Hübler. Cavopulmonary mechanical circulatory support in fontan patients and the need for physiologic control: A computational study with a closed-loop exercise model. *The International journal of artificial organs*, 41(5):261–268, 2018.
- [31] Kaiyun Gu, Yu Chang, Bin Gao, Youjun Liu, Zhe Zhang, and Feng Wan. Lumped parameter model for heart failure with novel regulating mechanisms of peripheral resistance and vascular compliance. *Asaio Journal*, 58(3):223–231, 2012.

- [32] Mohsen Abdi, Alireza Karimi, Mahdi Navidbakhsh, Gila Pirzad Jahromi, and Kamran Hassani. A lumped parameter mathematical model to analyze the effects of tachycardia and bradycardia on the cardiovascular system. *International Journal of Numerical Modelling: Electronic Networks, Devices and Fields*, 28(3):346–357, 2015.
- [33] IN Kiselev, FA Kolpakov, EA Biberdorf, VI Baranov, TG Komlyagina, IY Suvorova, VN Melnikov, and SG Krivoschekov. Patient-specific 1d model of the human cardiovascular system. In *2015 International Conference on Biomedical Engineering and Computational Technologies (SIBIRCON)*, pages 76–81. IEEE, 2015.
- [34] Francesco M Colacino, Francesco Moscato, Fabio Piedimonte, Maurizio Arabia, and Guido A Danieli. Left ventricle load impedance control by apical vad can help heart recovery and patient perfusion: a numerical study. *Asaio Journal*, 53(3):263–277, 2007.
- [35] Coleman TG Guyton AC, Jones CE. *Circulatory Physiology: Cardiac Output and its Regulation*. W.B. Saunders, 1973.
- [36] So-Hyun Jansen-Park, Mohammad Nauzef Mahmood, Indra Müller, Lisa Kathrin Turnhoff, Thomas Schmitz-Rode, Ulrich Steinseifer, and Simon Johannes Sonntag. Effects of interaction between ventricular assist device assistance and autoregulated mock circulation including frank–starling mechanism and baroreflex. *Artificial organs*, 40(10):981–991, 2016.
- [37] Johnny T Ottesen. Modelling of the baroreflex-feedback mechanism with time-delay. *Journal of mathematical biology*, 36(1):41–63, 1997.
- [38] Mauro Ursino. Interaction between carotid baroregulation and the pulsating heart: a mathematical model. *American Journal of Physiology-Heart and Circulatory Physiology*, 275(5):H1733–H1747, 1998.
- [39] Libera Fresiello, Ashraf William Khir, Arianna Di Molfetta, Maciej Kozarski, and Gianfranco Ferrari. Effects of intra-aortic balloon pump timing on baroreflex activities in a closed-loop cardiovascular hybrid model. *Artificial organs*, 37(3):237–247, 2013.
- [40] Simon Mushi and Yih-Choung Yu. Control of a mock circulatory system to simulate the short-term baroreflex. In *2008 American Control Conference*, pages 844–849. IEEE, 2008.
- [41] S Cavalcanti. Arterial baroreflex influence on heart rate variability: a mathematical

- model-based analysis. *Medical and Biological Engineering and Computing*, 38(2):189–197, 2000.
- [42] CA Swenne. Baroreflex sensitivity: mechanisms and measurement. *Netherlands Heart Journal*, 21(2):58–60, 2013.
- [43] Kevin D Lau and C Alberto Figueroa. Simulation of short-term pressure regulation during the tilt test in a coupled 3d–0d closed-loop model of the circulation. *Biomechanics and modeling in mechanobiology*, 14(4):915–929, 2015.
- [44] Stacy A Mandras and Sapna Desai. Right heart failure. 2017.
- [45] Motohiko Miyachi, Anthony J Donato, Kenta Yamamoto, Kouki Takahashi, Phillip E Gates, Kerrie L Moreau, and Hirofumi Tanaka. Greater age-related reductions in central arterial compliance in resistance-trained men. *Hypertension*, 41(1):130–135, 2003.
- [46] Hirofumi Tanaka, Frank A Dinunno, Kevin D Monahan, Christopher M Clevenger, Christopher A DeSouza, and Douglas R Seals. Aging, habitual exercise, and dynamic arterial compliance. *Circulation*, 102(11):1270–1275, 2000.
- [47] RH Mohiaddin, SR Underwood, HG Bogren, DN Firmin, RH Klipstein, RS Rees, and DB Longmore. Regional aortic compliance studied by magnetic resonance imaging: the effects of age, training, and coronary artery disease. *Heart*, 62(2):90–96, 1989.





## List of Figures

1.1	Cardiovascular system. . . . .	4
1.2	Heart anatomic section. . . . .	5
1.3	Cardiac valve plane. . . . .	6
1.4	Cardiac conduction system. . . . .	6
1.5	Frank-Starling mechanism. . . . .	8
1.6	Parameters influenced by the baroreflex mechanism. . . . .	8
1.7	Baroreflex mechanism outline considering a pressure decrease. . . . .	10
2.1	Hybrid impedance transformer (a) and circuit including VAD connection (b) as proposed by Darowsky [17]. . . . .	13
2.2	Schematic of mock circulation loop used by Timms [25]. . . . .	14
2.3	Comparison between distributed and lumped parameter models.[16] . . . .	15
2.4	Analog of the heart innervation as proposed by de Pater [28]. . . . .	16
2.5	Vessel electric analog. . . . .	16
2.6	Schematic model used to study baroreflex influence on heart rate variability [41]. . . . .	20
3.1	Mock loop set-up. . . . .	25
3.2	Simulink model overview. . . . .	27
3.3	Electric analog of the cardiovascular model[23]. . . . .	28
3.4	Simulink model of the circulatory system. . . . .	30
3.5	(a) LV elastance curves at different time of the cardiac cycle. (b) normalized ventricular and atrial contraction functions [34]. . . . .	31
3.6	GUI in cannulation choice. . . . .	37
3.7	GUI in <i>Device testing</i> mode for the left ventricle cannulation . . . . .	38
3.8	GUI in <i>Baroreflex</i> mode for the left ventricle cannulation . . . . .	39
3.9	Pump overall dimensions. . . . .	40
3.10	Relationship between voltage and pump rotation frequency. . . . .	41
3.11	Backflow pump datasheet. . . . .	42
3.12	Exhaust characteristics. . . . .	43

3.13	Time to obtain vacuum. . . . .	43
3.14	Pneumatic main components overview. . . . .	44
3.15	Electric schema. . . . .	44
3.16	Electrical Wiring Schematic. . . . .	46
3.17	Humusoft X1 Extension Board. . . . .	47
3.18	Humusoft X2 Extension Board . . . . .	48
3.19	24VDC to 5VDC voltage regulation circuit. . . . .	49
3.20	Linear Voltage Pressure Relationship. . . . .	50
3.21	Left ventricle pressure sensor curve relating voltage and operating pressure. . . . .	51
3.22	Aortic pressure sensor curve relating voltage and operating pressure. . . . .	51
3.23	Simulink model of the pressure controller. . . . .	52
3.24	Left ventricle level sensor curve relating voltage and water level . . . . .	54
3.25	Aortic level sensor curve relating voltage and water level . . . . .	54
3.26	Overview of the VAD and the backflow pump connecting the two chambers. . . . .	55
3.27	Simulink model of the level controller. . . . .	55
3.28	External structure of the relay. . . . .	56
3.29	Internal circuit of the relay. . . . .	57
3.30	Left ventricular chamber. . . . .	58
3.31	Level sensors voltage-height correlation. . . . .	58
3.32	Overview on PV loop parameters. . . . .	61
3.33	Graphic user interface if <i>Device testing</i> mode is chosen for the left cannulation. . . . .	62
3.34	Connection of the centrifugal pump to the circuit. . . . .	63
4.1	Numerical pressure tracings for LV (black line) and Ao (green line) varying the HR with UVV and SVR baroreflex control. . . . .	67
4.2	Numerical pressure tracings in time for LV (black line) and Ao (green line) varying the HR without baroreflex control. . . . .	67
4.3	Numerical pressure tracings in time for LV (black line) and Ao (green line) with HR=40 bpm as initial condition and HR,UVV,SVR baroreflex control. . . . .	68
4.4	Numerical pressure tracings in time for LV (black line) and Ao (green line) with HR=80 bpm as initial condition and HR, UVV, SVR baroreflex control. . . . .	68
4.5	Numerical pressure tracings in time for LV (black line) and Ao (green line) with HR=120 bpm as initial condition and HR, UVV, SVR baroreflex control. . . . .	69
4.6	Numerical pressure tracings for LV (black line) and Ao (green line) varying the CF with UVV and SVR baroreflex control. . . . .	69
4.7	Numerical pressure tracings for LV (black line) and Ao (green line) varying the CF without UVV and SVR baroreflex control. . . . .	70

4.8	Numerical pressure tracings in time for LV (black line) and Ao (green line) with $CF=1$ and HR, UVV, SVR baroreflex control. . . . .	70
4.9	Numerical pressure tracings in time for LV (black line) and Ao (green line) with $CF=0.2$ and HR, UVV, SVR baroreflex control. . . . .	71
4.10	Simulated left ventricular P-V loops considering HR variability. . . . .	72
4.11	Simulated left ventricular P-V loops comparison varying HR. . . . .	72
4.12	Simulated left ventricular P-V loops considering CF variability. . . . .	73
4.13	Simulated left ventricular P-V loops comparison varying CF. . . . .	73
4.14	HR variability changing the input aortic pressure. . . . .	74
4.15	Systemic arterial resistance variability changing the input aortic pressure. . . . .	75
4.16	Unstressed venous volume variability changing the input cardiac output. . . . .	75
4.17	Left heart pressures at different aortic valve resistance. . . . .	76
4.18	Numerical flow rate through the valve . . . . .	76
4.19	Numerical and experimental pressure tracings comparison for LV and Ao varying the HR with UVV and SVR baroreflex control. . . . .	78
4.20	Numerical and experimental pressure tracings comparison for LV and Ao varying the HR without baroreflex control. . . . .	78
4.21	Numerical and experimental pressure tracings comparison for LV and Ao varying the CF with UVV and SVR baroreflex control. . . . .	79
4.22	Numerical and experimental pressure tracings comparison for LV and Ao varying the CF without baroreflex control. . . . .	79
4.23	Left ventricle pressure waveforms and errors at HR=30 bpm and $CF=1$ . . . . .	80
4.24	Left ventricle pressure waveforms and errors at HR=60 bpm and $CF=1$ . . . . .	81
4.25	Left ventricle pressure waveforms and errors at HR=90 bpm and $CF=1$ . . . . .	82
4.26	Left ventricle pressure waveforms and errors at HR=120 bpm and $CF=1$ . . . . .	83
4.27	Theoretical and experimental left ventricular PV loops considering HR variability. . . . .	84
4.28	Right cannulation pressure waveforms and errors at HR=30 bpm and $CF_{RV} = CF_{LV} = 1$ . . . . .	85
4.29	Right ventricle pressure waveforms and errors at HR=60 bpm and $CF_{RV} = CF_{LV} = 1$ . . . . .	86
4.30	Right ventricle pressure waveforms and errors at HR=90 bpm and $CF_{RV} = CF_{LV} = 1$ . . . . .	86
4.31	Right ventricle pressure waveforms and errors at HR=120 bpm and $CF_{RV} = CF_{LV} = 1$ . . . . .	87
4.32	Right ventricle pressure waveforms and errors at HR=60 bpm and $CF_{RV} = 0.8, CF_{LV} = 1$ . . . . .	88

4.33	Right ventricle pressure waveforms and errors at HR=60 bpm and $CF_{RV}$ =0.6, $CF_{LV}$ =1. . . . .	89
4.34	Right ventricle pressure waveforms and errors at HR=60 bpm and $CF_{RV}$ =0.5, $CF_{LV}$ =1. . . . .	89
4.35	Theoretical and experimental right ventricular PV loops considering HR variability. . . . .	90
4.36	Theoretical and experimental right ventricular PV loops considering CF variability. . . . .	91
4.37	Pressure waveforms when VAD assisted (upper). Left ventricle volume waveform when VAD assisted (lower). . . . .	94
4.38	PV loop when the left ventricle is working in assisted (red) and unassisted (blue) conditions. . . . .	94
4.39	Plots of the blood pump flow rate vs time without assistance (upper figure) and with assistance (lower figure). . . . .	95
4.40	RV PV loop in assisted and unassisted conditions. . . . .	96
4.41	Numerical and experimental pressure tracings and PV loops with different levels of assistance. . . . .	97
4.42	Theoretical LV PV loops with and without VAD assistance . . . . .	98
4.43	Theoretical RV PV loops with and without VAD assistance . . . . .	98
4.44	Simulated flow rate and actual flow rate elaborated by the centrifugal pump	99
4.45	Simulated pressure waveforms (LV and Ao) and simulated LV volume wave- form. . . . .	100
4.46	Simulated pressure waveforms (LV and Ao) that follow the numerical trac- ings when VAD flow rate is delivered. . . . .	100
4.47	Theoretical LV PV loops changes with different levels of assistance. . . . .	101
4.48	Theoretical RV PV loops changes with different levels of assistance. . . . .	101
4.49	Resistance variation at different flow rates. . . . .	102
4.50	UVV, MAoP, CO variations at different flow rates. . . . .	103
4.51	LV and LA volumes at three pump flow rates. . . . .	104
4.52	Numerical $q_{av}$ tracings at three pump flow rates. . . . .	104
5.1	Graphic User Interface when choosing right cannulation. . . . .	110
5.2	Experimental flow rate through the valve. . . . .	112
6.1	Patient Specific GUI. . . . .	116

## List of Tables

2.1	Baroreflex control mechanism implementations . . . . .	21
3.1	Baroreflex control mechanism parameters. . . . .	35
3.2	Frequency-rpm relation. . . . .	41
3.3	Pressure and voltage measurements to obtain pressure sensors operating curve. . . . .	50
3.4	Pressure controllers parameters. . . . .	52
3.5	Level and voltage measurements to obtain level sensors operating curve. . .	53
3.6	Level controller parameters. . . . .	56
4.1	Physiological Parameters. . . . .	66
4.2	Experimental and numerical stroke work values. . . . .	92
4.3	$\Delta SW$ calculations varying contraction fraction. . . . .	92
5.1	Pressure errors with HR variability. . . . .	111



## Acknowledgments

First of all, we wish to thank the professor Maria Laura Costantino for the huge opportunity she gave us to work on such an interesting project. This thesis work was the first chance that we had to put our hands and brains into a laboratory, and the LaBS was the perfect structure for us to learn and gain experience. So many challenges have been brought to light, but we can definitely say that we have grown a lot as people and as engineers. We also want to thank the professor Francesco De Gaetano for being our tutor, our guide and our advisor throughout the thesis work. We would have been lost if he wasn't there to mentor us in times of mental crisis. In the end, we wish to thank the "Istituto Cardiocentro Ticino" for allowing this thesis work to happen.

